

SIMULATION OF COSMIC RAY INTERACTIONS WITH MATERIALS

BY

ALADDIN S. GELEIL

A THESIS

SUBMITTED TO THE FACULTY OF

ALFRED UNIVERSITY

IN PARTIAL FULFILLMENT OF THE REQUIREMENTS  
FOR THE DEGREE OF

DOCTOR OF PHILOSOPHY

IN

GLASS SCIENCE

ALFRED, NEW YORK

MARCH, 2011

Alfred University theses are copyright protected and may be used for education or personal research only. Reproduction or distribution in any format is prohibited without written permission from the author.

SIMULATION OF COSMIC RAY INTERACTIONS WITH MATERIALS

BY

ALADDIN S. GELEIL

B.S. ALFRED UNIVERSITY (2003)

M.S. ALFRED UNIVERSITY (2005)

SIGNATURE OF AUTHOR \_\_\_\_\_ (SIGNATURE ON FILE)

APPROVED BY \_\_\_\_\_ (SIGNATURE ON FILE)  
MATTHEW M. HALL, ADVISOR

\_\_\_\_\_  
(SIGNATURE ON FILE)  
ALEXIS G. CLARE, ADVISORY COMMITTEE

\_\_\_\_\_  
(SIGNATURE ON FILE)  
DOREEN E. EDWARDS, ADVISORY COMMITTEE

\_\_\_\_\_  
(SIGNATURE ON FILE)  
WILLIAM B. CARLSON, ADVISORY COMMITTEE

\_\_\_\_\_  
(SIGNATURE ON FILE)  
CHAIR, ORAL THESIS DEFENSE

ACCEPTED BY \_\_\_\_\_ (SIGNATURE ON FILE)  
DOREEN D. EDWARDS, DEAN  
KAZUO INAMORI SCHOOL OF ENGINEERING

ACCEPTED BY \_\_\_\_\_ (SIGNATURE ON FILE)  
NANCY J. EVANGELISTA, ASSOCIATE PROVOST  
FOR GRADUATE AND PROFESSIONAL PROGRAMS  
ALFRED UNIVERSITY

## ACKNOWLEDGMENTS

The author wishes to thank all the faculty and staff at Alfred University, the Kazuo Inamori School of Engineering, and what was formerly the New York State College of Ceramics for the opportunity to accomplish a great deal of learning and growing. A special thank you goes to Dr. James Shelby and Dr. Matthew Hall for thinking of me to do this NASA radiation project, and giving me invaluable access to them and everything I ever needed to do good research and be successful. Dr. Alexis Clare was also instrumental in my graduate school experience, and instilling a love for glassmaking and glass science. The help I got from James Thiebaud and Gerry Wynick is more appreciated than even they can realize, as were the many laughs shared with Gerry. My other friends and co-workers belong on this page as well, but there are many names. I would also like to thank parents, Dr. Nadia Geleil and Dr. Samir Geleil for being amazing people and for the unconditional love. I also remain thankful for having two great brothers in Sherif and Nader, who are my closest friends and confidants.

Acknowledgments .....	iii
Table of Contents .....	iv
List of Tables .....	vii
List of Figures .....	viii
<b>I. INTRODUCTION.....</b>	<b>1</b>
A. The Concern with Cosmic Radiation.....	6
1. Cosmic Radiation Background.....	6
2. The Interactions of Energetic Radiation Incident on Atoms .....	12
B. Basic Nuclear Structure and Properties .....	20
1. Static Properties.....	21
i. Electric Charge .....	21
ii. Mass and Energy .....	22
iii. Strong Nuclear Force .....	24
iv. Binding Energy .....	26
v. Shell Model .....	28
C. Dynamic Property - Radioactive Decay .....	32
1. Systematics .....	32
2. Decay Processes .....	33
i. Alpha Decay .....	34
ii. Beta Decay .....	35
iii. Beta Decay and Leptons.....	37
iv. Gamma and Other Decays.....	38
D. Nuclear Interactions.....	39
1. Tools for Investigating Nuclear Reactions .....	40
i. Q Values .....	40
ii. Cross sections .....	43
E. Mesons.....	47
i. Properties of Pi-mesons.....	48
ii. Stars .....	49
F. The Interaction of Radiation with Matter .....	50
1. Electromagnetic Radiation – Gamma Rays.....	51
i. Photoelectric Effect .....	51

ii.	Compton Scattering.....	52
iii.	Pair Production.....	53
2.	Charged Particles.....	55
i.	Coulomb Scattering.....	55
ii.	Inelastic Collisions.....	56
iii.	HCP.....	58
iv.	LCP.....	58
v.	Bremsstrahlung.....	61
vi.	Linear Energy Transfer and Stopping Power.....	62
3.	Neutrons.....	65
4.	Radiation Quantities and Dosimetry.....	70
<b>II.</b>	<b>EXPERIMENTAL PROCEDURE.....</b>	<b>75</b>
A.	Solar Protons in MCNPX.....	75
B.	GeV Proton and Heavy Ion Bombardment in FLUKA.....	81
1.	Proton Irradiation and <sup>12</sup> C Bombardment.....	82
C.	Estimates of Mean Range Using LISE.....	83
<b>III.</b>	<b>RESULTS.....</b>	<b>84</b>
A.	Effects of Primary Protons.....	84
1.	Secondary Gamma and Neutron Radiation.....	84
2.	Secondary Radiation.....	89
3.	Charged Pi-Meson fluence and Deposited Energy in Elemental and LDPE targets.....	92
B.	Deposited Energy.....	98
1.	Range Estimates.....	104
2.	Heavy Nuclei.....	110
i.	<sup>12</sup> C Irradiation of LDPE Target - Fragmentation.....	110
<b>IV.</b>	<b>DISCUSSION.....</b>	<b>115</b>
A.	Protons.....	115
1.	Secondary Gamma and Neutron Radiation.....	115
2.	Mesons.....	116
B.	Heavy Ion Bombardment.....	119
1.	Fragments.....	119

V. CONCLUSIONS..... 121

## LIST OF TABLES

		<b>Page</b>
Table I.	Hydrogen Content for some Proposed Shielding Materials .....	6
Table II.	Nucleons (Spin 1/2 baryons).....	25
Table III.	Quarks (Spin = 1/2).....	25
Table IV.	Mediators (Spin = 1).....	27
Table V.	Leptons (Spin = 1/2) .....	40
Table VI.	Quarks (Spin 1/2).....	50
Table VII.	Some Pseudoscalar Mesons (Spin = 0).....	51
Table VIII.	List of Heavy Charged Particles for Use at RHIC .....	63
Table IX.	Neutron Moderation Properties for Several Nuclei .....	71
Table X.	Radiation Quantities of Interest .....	76
Table XI.	Quality Factors (Weighting Factors) for Photon and Particle Radiation.....	77
Table XII.	Property Data for Fabricated SGM and Commercial HGM Glass .....	81
Table XIII.	Composition of Simulated Composite Target Materials .....	82
Table XIV.	Carbon, Hydrogen, and Ion Content of Composite Samples.....	83
Table XV.	Percentage of C, H, and Inorganic Ions Based on the Total Number of Ions or Atoms in the Simulated Composites .....	84
Table XIV.	Unstable Residual Nuclei from <sup>12</sup> C Irradiation of LDPE Target.....	120

# LIST OF FIGURES

		<b>Page</b>
Figure 1.	Abundance of Stable GCR Nuclei Up to Z=30 Measured at a Distance of One Astronomical Unit (A.U.) from Earth.....	8
Figure 2.	All-Particle Cosmic Ray Spectrum.....	10
Figure 3.	Schematic of Radiation Cascades Produced in Matter After Bombardment by an Energetic Nucleus. ....	13
Figure 4.	Schematic of Electron (e) and Proton (p) Ionization Tracks Through Photographic Emulsion.....	18
Figure 5.	Representation of Ionization Tracks for Projectile Nuclei. ....	19
Figure 6.	Representation of Cosmic Ray Tracks in Plastic.....	20
Figure 7.	Binding Energy per Nucleon. ....	28
Figure 8.	Nuclear Energy Levels and Shell Structure Obtained with the Spin-Orbit Interaction. ....	30
Figure 9.	Filled Proton and Neutron Levels in <sup>27</sup> Al. ....	31
Figure 10.	Laboratory and Center of Mass Frames.....	42
Figure 11.	Spherical Coordinate System.....	43
Figure 12.	Geometry of Scattering Cross Sections. ....	44
Figure 13.	Impact Parameters for Different Particles Impinging on a Target Nucleus. ....	44
Figure 14.	Schematic of K-Shell Photoelectron Produced via a keV $\gamma$ -Ray.....	52
Figure 15.	Schematic of Compton Scattering. ....	53
Figure 16.	Schematic of $\gamma$ -Ray Induced Electron-Positron Pair Production.....	54

Figure 17.	Effect of Z on $\gamma$ -Ray Interactions.....	55
Figure 18.	Rutherford (also Coulomb) Scattering.....	56
Figure 19.	Range in $\text{g}/\text{cm}^2$ Vs. Energy in MeV/u for $^1\text{H}$ (protons), $^4\text{He}$ , $^{12}\text{C}$ , and $^{56}\text{Fe}$ in Aluminum Metal. ....	57
Figure 20.	Representation of Energy Imparted over the Path Length for MeV Charged Particles and Subsequent Bragg Peak of Energy Deposition. ....	60
Figure 21.	Energy Deposition and Bragg Peak for 500 MeV Protons in Simulated Biological Tissue. ....	60
Figure 22.	Determination of Track Average and Dose Average LET. ....	64
Figure 23.	Simulated MCNPX Solar Proton Spectrum.....	81
Figure 24.	Irradiation Geometry used in Both MCNPX and FLUKA. ....	83
Figure 25.	Secondary Gammas and Neutrons Produced for $20\text{Li}_2\text{O}-10\text{Al}_2\text{O}_3-$ $70\text{B}_2\text{O}_3$ Composite Materials Relative to Pure LDPE. ....	85
Figure 26.	Secondary Gammas and Neutrons Transmitted through 2 cm of $20\text{Li}_2\text{O}-10\text{Al}_2\text{O}_3-70\text{B}_2\text{O}_3$ Composite Shielding.....	86
Figure 27.	Relative Gamma Ray Transmission Per Primary for Simulated Composite Materials Containing Lithium Borate or Lithium Aluminoborate Glasses. ....	88
Figure 28.	Relative Neutron Transmission Per Primary for Simulated Composite Materials Containing Lithium Borate or Lithium Aluminoborate Glasses. ....	88
Figure 29.	Gamma Ray Spectrum Behind Composites Containing Lithium Aluminoborate Glass. ....	90
Figure 30.	$^{27}\text{Al}$ Excited States and Prominent Gamma Ray Emission.....	91
Figure 31.	Neutron Spectrum Behind Composites Containing Lithium Aluminoborate Glass Particles.....	92
Figure 32.	Charged Pion Fluence in and Around Be Target.....	94

Figure 33.	Three-dimensional Representation of Charged Meson Track Density in and Be Target. ....	95
Figure 34.	Charged Pion Fluence in and Around Al Target. ....	95
Figure 35.	Three-dimensional Representation of Charged Meson Track Density in Al Target.....	96
Figure 36.	Charged Pion Fluence in and Around W Target.....	96
Figure 37.	Three-dimensional Representation of Charged Meson Track Density in W Target.....	97
Figure 38.	Charged Pion Fluence in and Around LDPE Target. ....	97
Figure 39.	Three-dimensional Representation of Charged Meson Track Density in LDPE Target.....	98
Figure 40.	Two-dimensional Projection of Energy Deposition in Be Target. ....	99
Figure 41.	Representation of Deposited Energy Density in Be Target. ....	100
Figure 42.	Two-dimensional Projection of Energy Deposition in Al Target.....	101
Figure 43.	Representation of Deposited Energy in Al Target.....	101
Figure 44.	Two-dimensional Projection of Energy Deposition in W Target. ....	102
Figure 45.	Three-dimensional Representation of Energy Deposition in W Target. ....	102
Figure 46.	Two-dimensional Projection of Energy Deposition in LDPE Target.....	103
Figure 47.	Three-dimensional Representation of Energy Deposition in LDPE Target. ....	104
Figure 48.	Range Estimates up to 3.0 GeV/u for Heavy Particles on Beryllium.....	105
Figure 49.	Range Estimates up to 3.0 GeV/u for Heavy Particles on Aluminum....	105
Figure 50.	Range Estimates up to 3.0 GeV/u for Heavy Particles on Tungsten .....	106

Figure 51.	Range Estimates up to 3.0 GeV/u for Heavy Particles on LDPE. ....	106
Figure 52.	Average Penetration Depth for $^1\text{H}$ , $^{12}\text{C}$ , and $^{56}\text{Fe}$ in Beryllium. ....	107
Figure 53.	Average Penetration Depth for $^1\text{H}$ , $^{12}\text{C}$ , and $^{56}\text{Fe}$ in Aluminum. ....	108
Figure 54.	Average Penetration Depth for $^1\text{H}$ , $^{12}\text{C}$ , and $^{56}\text{Fe}$ in Tungsten. ....	109
Figure 55.	Average Penetration Depth for $^1\text{H}$ , $^{12}\text{C}$ , and $^{56}\text{Fe}$ in LDPE. ....	109
Figure 56.	Unstable Fragments Generated in LDPE per Primary. ....	112
Figure 57.	Stable Fragments Generated in LDPE per Primary. ....	112

## ABSTRACT

A representative group of target materials were simulated and irradiated within the physics framework of two Monte Carlo particle transport codes to determine the general effects of energetic space radiation on common solid materials. The target materials consisted of low-density polyethylene, polyethylene-based composite filled with glass particles, and solid slabs of beryllium, aluminum, and tungsten metals. The simulated composites were irradiated by solar protons within the MCNPX software to determine the secondary gamma and neutron radiation generated in and transmitted through potential lightweight shielding materials. The pure polyethylene and elemental targets were bombarded by protons and  $^{12}\text{C}$  nuclei within FLUKA to determine the extent of charged meson production, energy deposition, and generation of stable or unstable nuclear fragments within the target. The polyethylene-based composites of this work enable a maximum of 8% weight reductions, so have potential value as lightweight shielding materials, but any incorporated elements with  $Z$  significantly larger than one cause detrimental neutron and gamma radiation to be produced by the incident proton events. Charged meson production peaks at a density of about  $10^{-4}$  per incident primary at the center of the particle beam, and a maximum of roughly  $10^{-4}$  GeV/cm<sup>3</sup> of energy is deposited in all targets per primary proton. The polyethylene targets appear to backscatter significant particle radiation, and also yield only 6 unstable fragments within, compared to 11 stable fragments. Unstable fragments decay by electron capture, which does not result in a significant dose from the emitted neutrinos. The effects of other radiation-matter interactions such as scattering events and Bremsstrahlung are also discussed.

## I. INTRODUCTION

This work deals with what is known as “the radiation problem” with regard to deep-space exploration. NASA and other international space agencies are pursuing manned missions to the Moon and eventually Mars, but the continuous background of cosmic rays propagating through space presents a formidable problem. The galactic cosmic radiation (GCR) background is made up of various high energy particles and electromagnetic radiation. Astronomers have observed an extensive spectrum with regard to types and energies of cosmic rays, from x- and gamma-ray photons, to solar protons and the nuclei of many elements of the periodic table.<sup>1-3</sup> The primary GCR particles are electrons, protons, and helium, and nuclei such as carbon, oxygen, and iron that are produced by stars. The secondary GCR particles are lighter nuclei such as lithium, beryllium, and boron, which are not abundant end-products of stellar nucleosynthesis, but are the result of fragmentation of projectile or target nuclei in space.<sup>4-6</sup> The particle radiation flux in the relevant regions of space consists of about 90% solar protons, 9% helium nuclei, and about 1% heavier nuclei such as <sup>56</sup>Fe, <sup>16</sup>O, <sup>28</sup>Si, and <sup>12</sup>C, with an elemental distribution a bit like what is seen on Earth.<sup>1-3</sup> The energies of these particles can range from a few million electron-volts (eV) to more than 10<sup>20</sup> eV,<sup>3</sup> which would result in a prolonged radiation exposure to the inhabitants of any spacecraft.

The interaction of high-energy radiation with materials is an area of research that combines the fields of nuclear and particle physics. There are potentially many nuclear reactions that may occur when energetic particles experience bulk matter. The reactions and their properties are divided into three categories based on the incident energy of the particle projectiles: “low energy” is taken to be of the order of 10 MeV per nucleon or less, “medium energy” is 100 MeV to 1 GeV, and “high energy” reactions occur at 1 GeV per nucleon and higher.<sup>7</sup> Nuclear and particle interactions become increasingly more complex when going from low to high energy. For medium energy reactions, one may observe the production of mesons or other particles, and protons and neutrons may transform into each other.<sup>7</sup> At high energy, numerous exotic phenomena occur, such as quark rearrangement,<sup>7</sup> and many other exotic particles also begin to appear, such as W

and Z bosons, and K or  $\psi$  mesons.<sup>7,8</sup> The study of these unusual reactions is known as particle physics.

High energy charged particles ionize atoms in their path within materials, and the ionization effects increase rapidly for larger and/or faster particles. Energetic nuclei present significant hazards because they will densely ionize targets. Energetic charged particles will slow down as they traverse until they are captured, because of inelastic collisions with atomic electrons. Electrons also serve to attenuate the energy of gamma rays by what is known as Compton scattering, but in the processes of most interest, the role of atomic electrons is reduced in comparison to the extent of nuclear phenomena that may occur when materials are bombarded by energetic particles or radiation. For example, protons begin to produce mesons when they have 300 MeV of energy or greater,<sup>1,7,9</sup> and there are 4 different types of mesons that are seen when an incoming proton's energy is increased.<sup>7</sup> Any potential deep space travelers should know the extent of the various deep-space radiation phenomena, so they might have an idea of the dose they were experiencing. On earth, people do receive a continual dose of cosmic radiation, but there is no concern because it is negligible due to the thickness of the atmosphere and the vast number of molecules it contains.<sup>1,7,10</sup>

The emphasis in developing GCR shielding materials must be placed in avoiding or minimizing the effects of multiple radiation interactions with exterior and interior components of spacecraft.<sup>10-12</sup> The earth is always being bombarded with high-energy cosmic rays, but the kilometers of thickness and large numbers of molecules in the atmosphere strongly attenuate the incident radiation and thus the harmful effects on earth's inhabitants. For objects in orbit and without the aid of an atmosphere, the distance from earth is also a concern, as the earth's magnetic field deflects many of the charged particles away or into more shallow (and less harmful) trajectories. This benefit is eliminated for geosynchronous orbit distances or further (> 30,000 km). Magnetic shielding in spacecraft is also being considered as a potential solution to the radiation problem,<sup>13,14</sup> but deep-space travel does not afford the luxury of a protective magnetic field, and proximity to such an intense magnetic field may have negative consequences on biological systems.

In present designs, crews on any manned-mission to Mars would face a one-way travel time of roughly seven months, during which they would continually experience secondary particles and radiation as products of the interaction of GCR with spacecraft components. Experiment and observation have shown that materials of lowest possible atomic number and containing the fewest nucleons are much more effective at moderating the effects of the incident GCR.<sup>7,11-15</sup> The materials investigated here and which of most interest are meant specifically to shield the effects of incident  $^{56}\text{Fe}$ , since it is the heaviest component of GCR, is heavily-ionizing radiation, and its interaction with target materials causes fragments, energetic neutrons and electromagnetic radiation which must also be defended against. Neutrons, being uncharged, do not interact with coulomb fields or charged particles, but pass through matter and collide with nuclei. The collisions reduce the energy of the neutrons until they are absorbed by some nucleus after multiple events. The smallest nuclei are much more effective at reducing the energy of neutrons, with hydrogen being 6 times better than carbon and more than 100 times better than uranium.<sup>7,16</sup>

The optimum shield against GCR would then be some variant of pure  $^1\text{H}$  or a material containing a significant concentration of hydrogen.<sup>7,11-15</sup> Typical aerospace structural metals such as Al or Ti perform poorly as shields, because they produce nuclear fragments and decay products such as gamma rays or neutrons behind them.<sup>7,10-12</sup> The emitted gamma rays are due to the de-excitation of nuclear excited states, which may also result in nucleon or  $\alpha$  emission. The various products of the nuclear interactions can all be of at least a MeV, but are typically much more energetic. The exiting gamma ray and neutron fluence will generally be of the same order of magnitude in energy as the incident radiation,<sup>10,12,17,18</sup> which has been verified by the author in simulations of 20 GeV proton irradiation. Some of the lower energy products are most commonly of the order of 1-10 MeV, which results in significant radiation exposure in the space environment.

The energetic radiation in space would be harmful for any amount of time, but seven months provides a situation in which it is impossible for a human to survive without lasting detrimental effects.<sup>19,20</sup> MeV particles or radiation will ionize atoms or molecules in the body, and produce showers of secondary radiation that could effect

organisms.<sup>19,20</sup> The large mass of the neutron will cause collisions that literally knock other nuclei out of position, breaking hydrogen bonds, for example, as the neutron is attenuated.<sup>7</sup> When the neutrons are slow enough to be absorbed, the resulting nucleus is excited and radioactive to the surrounding biological tissue. Any extended deep-space travel must provide radiation protection, even from the effects of the spacecraft's hull itself.<sup>10,12-14,21</sup>

Radiation protection for successful deep-space manned missions therefore requires some atypical considerations, such as the use of large volumes of low atomic number compounds like water or low-density polyethylene (PE) to surround portions of a spacecraft, and thereby inhibit the interaction of GCR with the higher Z nuclei that would be present in most mechanical and electrical spacecraft components.<sup>10,12-14</sup> It is serendipitous that the low-Z, hydrogen-containing materials such as H<sub>2</sub>O or LDPE are of low mass-density, since space payloads have been estimated to cost roughly \$20,000/kg at the time of this writing. LDPE contains the highest hydrogen-density of any common material, so this work focused on glass particle as LDPE additives in the aim of providing some nuclear functionality, specifically the attenuation and capture of secondary neutrons from the fragmentation of energetic primaries with target materials.

The materials investigated here are glasses and composite materials. Glasses are versatile solids in that they can be formed with many elements of the periodic table, and over a vast range of compositions, which allows very specific functionality or properties to be incorporated into a material. The original goal of this work was the design and fabrication of a lightweight composite material featuring hollow glass microspheres (HGM) embedded in an LDPE matrix. The original HGM composition was proposed to be in the lithium borate (Li<sub>2</sub>O-B<sub>2</sub>O<sub>3</sub>) series of glasses, with other elements incorporated within to enhance chemical durability. The hollow glass spheres were meant to act as small containers for high-pressure hydrogen gas, and to reduce the mass density of the composite relative to pure LDPE. The presence of hydrogen gas in HGM increases the cosmic ray shielding potential of the composite materials relative to the use of HGM for lightweighting alone.

The formation of hollow glass spheres appears highly dependent on glass composition, with silicate glasses being far superior to the borate glasses investigated

here. Current studies elsewhere are focused on filling HGM with significant pressures of hydrogen gas, perhaps up to 10,000 psi (69 MPa), which has generally involved silicate-based glasses of commercial compositions such as Pyrex and soda-lime silicate. The borate glasses studied were not as suitable in the formation of HGM, as these glasses generally display more fragile liquid behavior and very low viscosity at the temperature of the torches used to form hollow glass spheres, which was about 1900° C. A series of  $\text{Li}_2\text{O}-\text{Al}_2\text{O}_3-\text{B}_2\text{O}_3$  glasses with different  $\text{Li}_2\text{O}/\text{Al}_2\text{O}_3$  ratios was investigated for their ability to form HGM. The variation in the  $\text{Li}_2\text{O}/\text{Al}_2\text{O}_3$  ratio allows a range of different viscosity behaviors to be achieved, and inclusion of 8-15 mol%  $\text{Al}_2\text{O}_3$  greatly enhances the durability of these glasses relative to binary  $\text{Li}_2\text{O}-\text{B}_2\text{O}_3$  glasses.<sup>22</sup>

The choice of lithium and boron as the major glass constituents serves multiple purposes. Both lithium and boron are of low atomic number, with  $Z = 3$  and  $Z = 5$ , respectively, which is advantageous in minimizing nuclear interactions with heavy primary particles. Lithium and boron are also used because they feature a natural abundance of two stable isotopes,  ${}^6\text{Li}$  and  ${}^{10}\text{B}$  which have the potential to capture thermal neutrons, which are about 0.02 eV.<sup>7,10</sup> Roughly 7.5% of natural lithium is  ${}^6\text{Li}$ , and 19.9% of natural boron is  ${}^{10}\text{B}$ . Both isotopes and have large values for the thermal energy neutron-capture cross sections, which are 940 and 3840 b respectively.<sup>7</sup> Other studies of radiation shielding materials have shown a reduction in transmitted neutron flux when this type of efficient neutron absorber is added to materials like LDPE.<sup>10,12,21</sup> It was hoped that the presence of these isotopes in the composite material might capture and attenuate some of the transmitted neutron flux behind the composite. Ideally, the HGM would then be filled with hydrogen gas (perhaps 1,000-10,000 psi or 6.9-69 MPa), and the natural abundance of  ${}^6\text{Li}$  and  ${}^{10}\text{B}$  in the glass sphere's shell would aid in capturing neutrons generated in the fragmentation of  ${}^{56}\text{Fe}$  ions incident on the material. The hollow, gas-filled shells reduce the mass density of LDPE, while still maintaining relatively high hydrogen density. The hydrogen density of some proposed shielding materials shown in Table I.<sup>23,24</sup>

**Table I.** Hydrogen Content for some Proposed Shielding Materials.<sup>23-25</sup>

<b>Material</b>	<b>No. Hydrogen Atoms per cm<sup>3</sup> (x10<sup>22</sup>)</b>	<b>No. Hydrogen Atoms per g (x10<sup>22</sup>)</b>
Hydrogen (solid; liquid)	5.7; 4.5	59.7; 59.7
H <sub>2</sub> gas at 20 MPa	0.95	0.92
Water	6.7	6.7
Lithium hydride	5.9	7.6
Pure polyethylene (LDPE)	8.9	8.6
5 % borated LDPE	6.6	8.2

## **A. The Concern with Cosmic Radiation**

### **1. Cosmic Radiation Background**

The components of the cosmic radiation (CR) background local to our solar system may be generally subdivided into three different groups: solar, non-solar, and extra-galactic, based on the original source of the particles. The sun is the local source of charged particles such as protons and helium nuclei, with the upper limit of energy for these particles being around 1000 MeV (1 GeV). There are also two types of more energetic CR which originate from much further away. The large majority of non-solar CR come from our own Milky Way galaxy, possibly from sources such as supernovae. Though many of the exact sources of non-solar CR are not known, unusual stars such as supernovae are known to eject high-energy electrons and other particles into their environment. The third classification are the very high-energy particles (VHE) which are termed extra-galactic, since there is now increasing evidence that they come from any of the vast number of distant galaxies.<sup>1-3</sup> The VHE particles are accelerated to such high energy, perhaps tens of thousands of GeV and higher, which means they can not be contained within their galaxy or origin, and hence propagate through the universe almost unaffected by the magnetic fields of galaxies, stars, or planets.<sup>1-3</sup> The space environment between earth and mars is devoid of magnetic fields or other defenses, so any spacecraft

will have to act as a self-contained shield for all three possible types of radiation, even the exceedingly-rare VHE particle events.

The cosmic ray spectrum shows a wide distribution of elements, with each nucleus being very energetic at the moment they are incident on any targets. For a distance of one astronomical unit (1 A.U. =  $1.4960 \times 10^{11}$  m) from earth, the relative abundances of nuclei up to  $Z=30$  in three different energy distributions are depicted in Figure 1. The lighter nuclei such as Li, Be, and B show relatively low abundance in the solar system, but are present in significant amounts as cosmic rays. This is due to the spallation of larger nuclei as they propagate through space and interact with the atoms of the interstellar medium.<sup>5,6,26</sup> A comprehensive review of the elemental and isotopic composition of the cosmic rays was given by J.A. Simpson.<sup>2,3</sup> The energies of the particles in space are significant, ranging from 70-2000 MeV. Depicted in the inset of Fig. 1 is the spherical shell centered on the earth, with the radius of one A.U. The flux is given as a number of particles passing through a unit of area and time ( $\#/m^2\text{-sr-s-MeV}$ ) normalized to the amount of Si ions at a distance of 1 A.U. from earth, where sr denotes steradians of solid angle. The abundance of H is off the scale, while He is about  $10^5$  times more abundant than Si. All elements are present up to Ni, although for nuclei larger than  $Z=30$ , the abundance is reduced by a factor anywhere from  $10^2$  to  $10^6$ . There is more significant contribution to the GCR from such heavy nuclei as C, O, Ne, Mg, Si, and a large spike is seen for  $Z=26$ , which represents Fe. The heaviest nuclei, such as  $^{56}\text{Fe}$ , represent the largest hazard to the presence of humans in deep space, due to the multitude of particles in these nuclei and their high incident energy.

In addition to heavy charged particles throughout space, there is a fairly continuous background of high energy electromagnetic radiation. Any photon that exceeds the typical energy of X-rays is termed a gamma ray ( $\gamma$ ). The X-ray portion of the electromagnetic spectrum is generally taken to vary from 100 eV to 100 keV, for which the corresponding wavelength ( $\lambda$ ) range is from 12.4 nm to 12.4 pm. Thus gamma rays are photons with energies greater than 100 keV, and the upper limit of gamma photon energies can be in the tera-eV ( $\text{TeV} = 10^{12}$  eV) range or greater. Current studies in  $\gamma$ -astronomy employ the giga-eV ( $\text{GeV} = 10^9$  eV) to peta-eV ( $\text{PeV} = 10^{15}$  eV) range of photon energy, typically from extragalactic sources.<sup>1-3,27</sup> Gamma rays are produced by

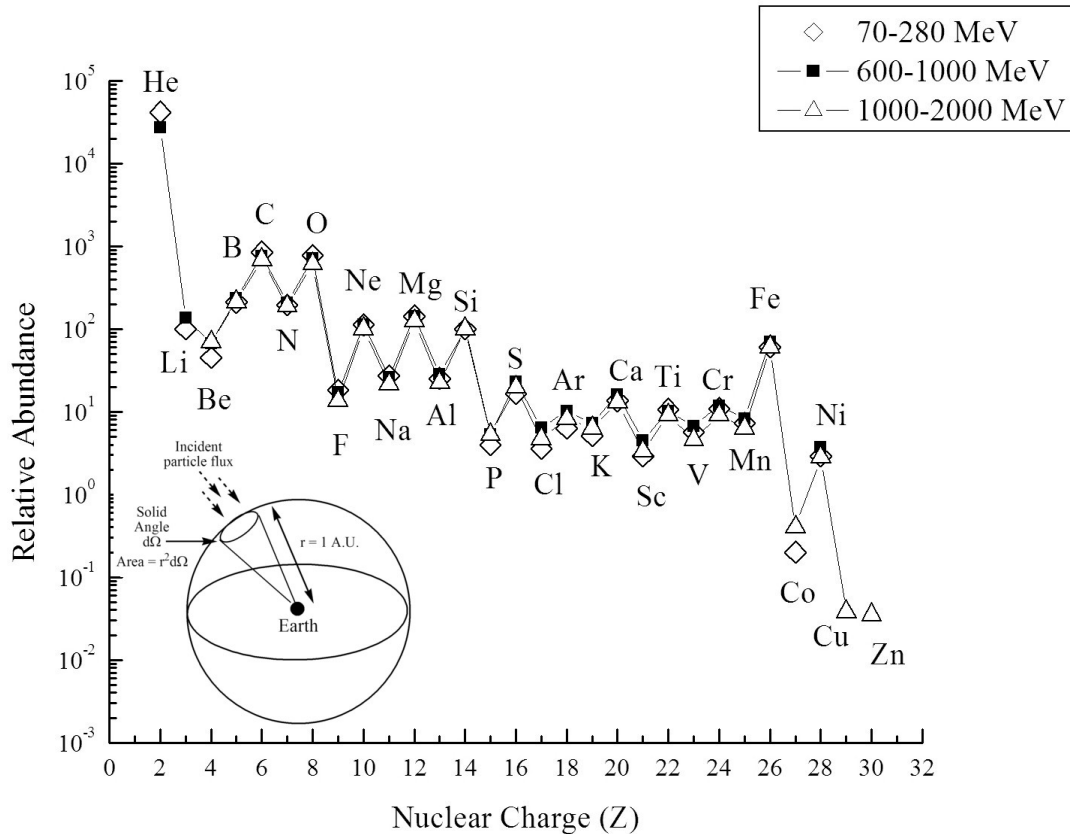


**Figure 1.** Abundance of stable CR nuclei up to  $Z=30$  measured at a distance of one astronomical unit (A.U.) from earth.<sup>2,3</sup>

some of the hottest regions of the universe, and also in violent astrophysical events and phenomena, such as supernovae explosion and the destruction of atoms.<sup>27,28</sup> Gamma ray sources also include objects such as neutron stars, pulsars, and black holes, as well as the decay of radioactive atoms in space.

The cosmic radiation flux in deep space is similar to both the flux at one A.U. and at the top of the earth's atmosphere, and this consists of all stable charged particles and nuclei with lifetimes  $10^6$  years or longer. Within this group are the primary particles, which are nuclei produced by stars, and are directly accelerated to high energy by some astrophysical source. There are also secondary particles which are the smaller nuclei, and are from the interaction of primaries with the carbonaceous molecules and other constituents of the interstellar medium (ISM).<sup>29</sup> The unstable particles, which are those subject to some form of radioactive decay, are not as common in shielding studies.

A very active current area of astrophysical research involves the origin and propagation of the very high energy (VHE) particles. The VHE particles that are sometimes detected feature energies of almost incomprehensible magnitude. Nuclei heavier than protons are commonly called high-z, high-energy (HZE) particles, and objects as small as protons are considered charged heavy particles. Performed at accelerating facilities, particle interactions are most commonly studied at energies of MeV ( $10^6$ ) to GeV ( $10^9$ ), but the VHE spectrum is known to have components of in the range of TeV, PeV, and exa-eV (EeV,  $10^{18}$  eV).<sup>2,3</sup> TeV studies are exceedingly difficult, and nothing more energetic than 3 TeV has ever been achieved at an accelerator, which was demonstrated in early 2010 at the Large Hadron Collider at CERN. Any particles containing greater than  $10^{17}$  eV of energy are considered ultra high energy (UHE). There is also the question of whether the spectrum extends well beyond  $10^{20}$  eV, which is currently the foremost problem in high-energy particle astrophysics.<sup>3</sup> The single highest energy ever reported for a particle incident on earth was  $3 \times 10^{20}$  eV, which was recorded at the “Fly’s Eye” detector of the University of Utah.<sup>1</sup> It is estimated that only one of these extremely-energetic particles strikes each  $\text{km}^2$  of the earth’s atmosphere each century.<sup>1-3</sup> The VHE and UHE particles travel at speeds that are very close to  $c$ , so total energy of a moving particle is the sum of its kinetic energy ( $T$ ) and its rest mass energy ( $mc^2$ ). The velocity by itself is not a good indicator of how energetic the particle truly is, so a better consideration is the ratio of the total energy ( $T + mc^2$ ) to the rest mass energy ( $mc^2$ ). The ratio of  $(T+mc^2)/mc^2$  can reach values of up to  $10^{11}$  for the VHE or UHE particles.<sup>1-3,7</sup>

The collected observations about cosmic ray abundance and propagation have yielded an all-particle spectrum with a unique shape, as shown in Figure 2. Displayed is the particle *flux* (normalized to 1 GeV energy and in units of  $\# / [\text{m}^2 * \text{steradian solid angle} * \text{second}]$ ) against the particle energy in GeV. Flux can be thought of as a *rate*, so it is reported as some number per area per second. This is in contrast to the term *fluence*, which can be thought of as the total *number* to pass through an area during the course of some time interval. The flux of the VHE particles drops off rapidly and continuously from a maximum flux of about  $10^4 \text{ m}^{-2}\text{sr}^{-1}\text{s}^{-1}$  at 1 GeV to  $1 \text{ m}^{-2}\text{sr}^{-1}\text{s}^{-1}$  at 100 GeV, after which there are two features at high energy. The “knee” is a small upturn in flux which

peaks at about  $10^{-6} \text{ m}^{-2} \text{ sr}^{-1} \text{ s}^{-1}$  at  $10^{15}$ - $10^{16}$  GeV, after which the particle flux drops at the same rate of energy dependence over about 3 orders of magnitude. For VHE flux between  $10^{19}$  and  $10^{20}$  eV, there is another slight bump that peaks at about  $10^{-14} \text{ m}^{-2} \text{ sr}^{-1} \text{ s}^{-1}$ , which is termed the “ankle”. The approximate flux at three areas in the curve is denoted. It is fortunate for any would-be space traveler that the detected flux of VHE particles above 100 GeV is reduced to just a few particles per  $\text{m}^2$  per year.

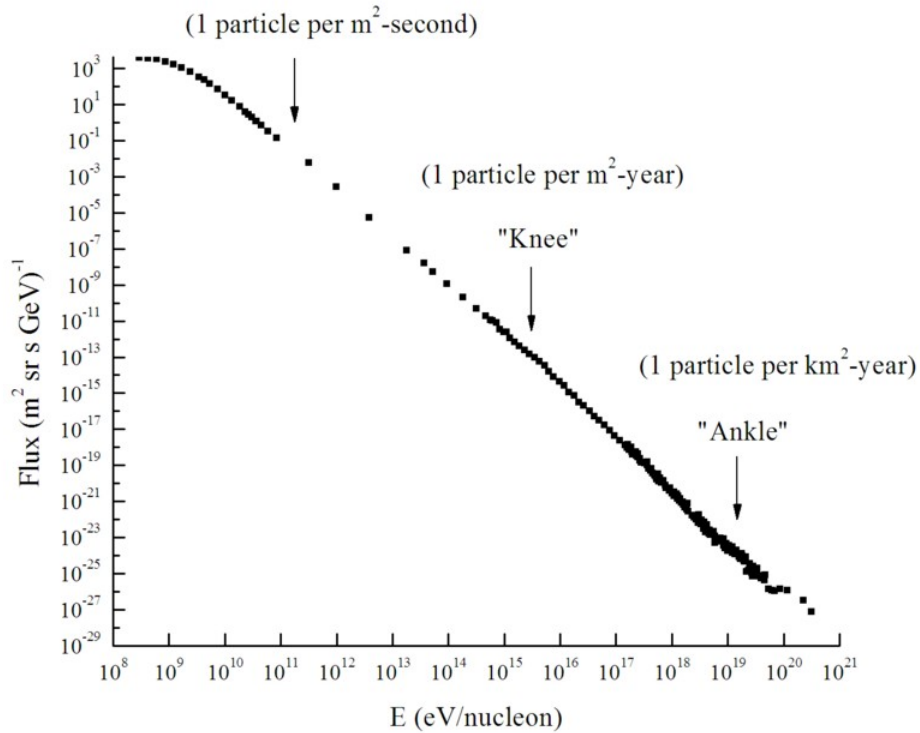


**Figure 2.** All-particle cosmic ray spectrum. The very high and ultra high energy events ( $> 10^{17}$  eV) are exceedingly rare.

The primary particles include protons, electrons, helium, and heavier nuclei which are products of stellar nucleosynthesis, and may exist in a quasi-free state in the space surrounding some active astrophysical body. The secondary particles are the result of primaries impinging on nuclei such as  $^{12}\text{C}$  in the interstellar medium (ISM),<sup>5,6,26</sup> and causing the formation of a nucleus of different charge, which will propagate energetically away from the collision. The majority of the fragmentation nuclei are Li, B, and Be, and

it is now believed that the secondary production process is responsible for much of the abundance of these nuclides in the universe.<sup>4-6,11,26,30,31</sup> The ISM contains a great deal of ordinary matter and the constituent nuclei such as  $^{12}\text{C}$  and  $^{16}\text{O}$ , and essentially any charged particle that strikes such a nucleus can cause a fragmentation reaction, so the creation of secondary Li, B, and Be is common.<sup>29</sup> The identity of the secondary particle will depend on the incident particle and energy, but the majority of these reactions involve incident protons or helium nuclei as the projectiles.

The sun produces protons and helium up to about 1 GeV/nucleon, but there are also sources of high-energy particles that are much further away. The evidence of more distant sources is that there is a negligible difference in the cosmic ray flux between night and day,<sup>1</sup> which points to agents external to the sun, but most likely from within the milky way galaxy. The sun also provides some beneficial effects, such as modulating and reducing the energy of the majority of extra-galactic GCR radiation by a factor of 2/3 or more. The acceleration mechanisms for the very-high energy particles are theorized to be events such as shockwaves that accompany a “nearby” supernova explosion.<sup>1-3,28,32</sup> Particles are caught by the propagating shockwave front, and the extreme violence of the event propels them to relativistic speeds. The resulting particles often cannot be contained by their galaxy of origin, so are basically free to propagate extreme distances, until either they interact with some component of the ISM, or have their energy modulated by an astrophysical object upon entering some different galaxy.

The possibility of nuclear interaction with target materials is increased for incident particles of both high-Z and high-energy (termed HZE particles). The negative effects are greatly magnified with an increase in either the incident energy or Z of the particle, because of the increased probability for nuclear interactions. The modulation effects of the sun limit most of the GCR present in our solar system to a maximum of about 1 GeV per nucleon. The heaviest HZE particles at about 1 GeV per nucleon would therefore have the most adverse effects on objects in the space environments of interest. The heaviest and most abundant stable nuclei in the GCR pose the most significant risk to people in deep-space, which is greatly amplified for  $Z \geq 2$ . The  $^{56}\text{Fe}$  nucleus is most stable because it has the highest binding energy per nucleon, and it is therefore a common product in the late stage, high-temperature reactions within stars. The  $^{56}\text{Fe}$  in the GCR of

our solar system has a maximum energy of about 1.05 GeV/nucleon in the modulated GCR spectrum, so much of the study in shielding is being done specifically to combat this constituent of the GCR at this energy, because of the number of high-energy nucleons that are incident for every  $^{56}\text{Fe}$ . Though moderately rare, such an energetic and heavy nucleus has multiple deleterious effects on objects in its path.

## 2. The Interactions of Energetic Radiation Incident on Atoms

When penetrating radiation such as high-energy CR enters the earth's atmosphere, the collisions with atoms change their identity and produce showers of effects due to the energy loss of the incident projectiles. The heavy CR particles such as helium, carbon, and other nuclei, are generally fragmented when they collide, but may also fragment the nucleus of the target atoms. The projectile nuclei lose a large fraction of their initial energy by collision and fragmentation into lighter nuclei, and the energy difference from the collision or lost mass manifests itself in the products that emerge from these collision reactions; these products can be particulate or electromagnetic in nature. There are streams of radiation that are produced by collisions, including fragments of the projectile or target, neutrons, energetic electrons, high-energy electromagnetic radiation (such as  $\gamma$ - or hard x-rays), and *mesons*. These energetic species become projectiles themselves, and propagate further to take part in additional collisions with atoms. Figure 3 displays a simplified picture of the process. Mesons are rather exotic, as explained later in I.5, but they begin to appear when the incident projectile energy is approximately equal to or greater than several hundred MeV (perhaps 300 MeV).<sup>1,7,9</sup> Mesons consist of different quark-antiquark pairs that exist briefly in bound state. The lighter mesons (primarily K and  $\pi$ ) are a necessary part of the discussion when bombarding materials with GeV radiation, such as that in space, because mesons will ionize and deposit energy within target materials, and may cause undesirable effects in target nuclei. Mesons decay into *muons*, which eventually decay into electrons. Even after the disintegration or decay of the original particle, the incident projectile leaves a lasting impression on the atoms within materials or atmospheres due to the showers of effects that are produced after the initial collision.

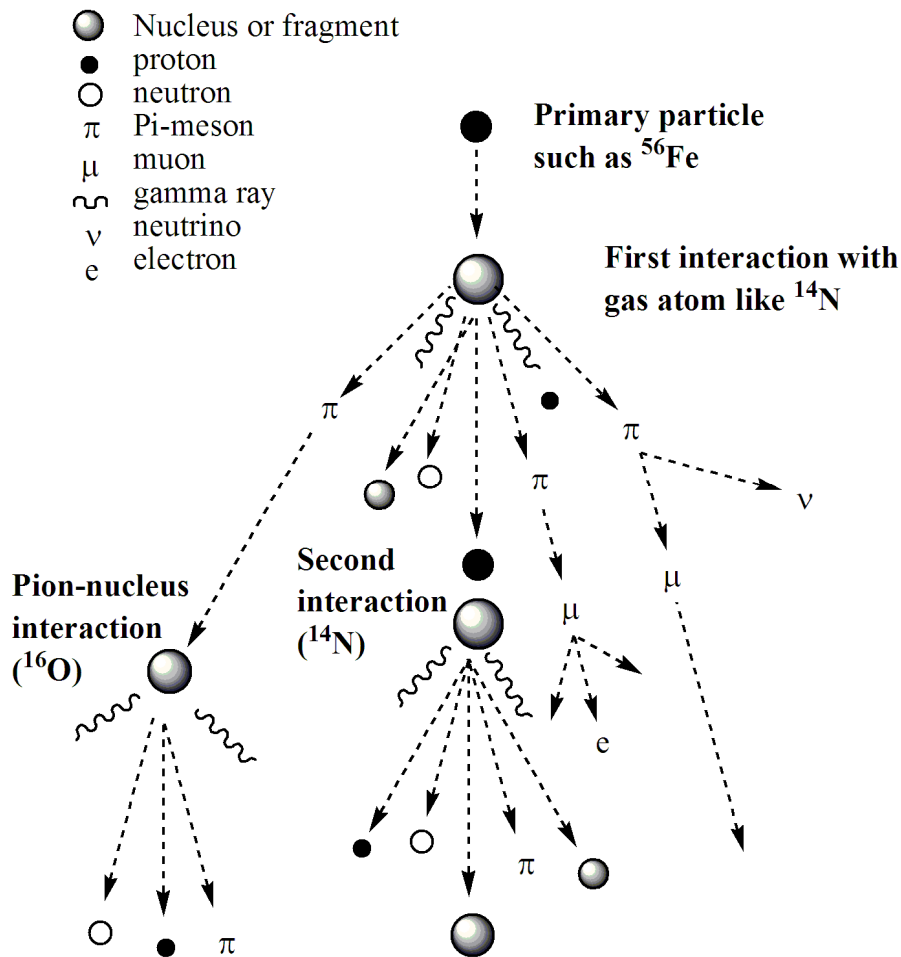


**Figure 3.** Schematic of radiation cascades produced in matter after bombardment by an energetic nucleus.

The observed radiation showers are called *cascades*, which develop as the collision and energy loss process is repeated over many generations through matter, as would occur for atmospheres of gaseous composition. When mesons decay or collide with other atoms in the air, more particles such as electrons are produced. These electrons may be energetic enough to take part in further collisions with atoms, but may also radiate energy as they encounter the electric fields set up by atomic and molecular arrangements. Moving charges radiate electromagnetic energy when they are accelerated, so cascade electrons can radiate photons as they are being decelerated, with

the radiated photons possibly ionizing atoms lower in the cascade, and producing further streams of electrons. There are an immense number of possibilities in the cascade sequence, which makes the original identity or ultimate effect of one incident particle almost impossible to trace. An initially-massive particle such as a  $^{56}\text{Fe}$  nucleus will have basically evaporated after a number of interactions, but will leave generations of energetic fragments that greatly affect their surroundings. Muons and electrons constitute the majority of the radiation that survives and is observed at the earth's surface, with muons being the product of a pi-meson decay, and electrons being the product of muon decays. There are billions of individual particles and photons that are produced in a cascade, with the resulting shower possibly covering hundreds of square kilometers.

Any matter will be subject to internal radiation cascades upon bombardment, so the effect is not confined to just planetary atmospheres. The vast extent of an air shower is due to the height and number of molecules in the atmosphere, but similar processes are seen for any thickness of solid materials in the path of energetic radiation, with the effects greatly dependent on density. This includes any materials used in the construction of spacecraft: electronic and structural components, the hull of the ship, and even the shielding materials themselves. Elements of low mass-density, such as aluminum, have traditionally been advantageous in the aerospace industries, because of their low cost and light weight, so aluminum metal has been used in spacecraft hulls. Thin materials like aluminum shells may be advantageous compared to thick materials because they don't produce the same number of cascading generations, but the detriment is that energetic particles pass right through light metals, see little to no attenuation, and collide with human occupants with most of their initial energy.<sup>11,12,15</sup> The radiation will then directly ionize human tissues, as well as producing cascades within the body. The cascade process is inevitable, so protective measures can only be realized by minimizing the amount of 'stuff' that is liberated during the initial interaction of the primary with material nuclei. To estimate the extent of a cascade within some region of matter, the energy contained within the incident primary due to its mass and velocity must be characterized.

The initial total energy of moving particles is the sum of the rest mass energy and the kinetic energy, with the kinetic energy being the primary source for material changes

such as ionization. The rest mass energy (E) is given by the relation for mass-energy equivalence made famous by Einstein,  $E = mc^2$ , where m is the mass of the object, and c is the speed of light. The expression holds true for all non-moving particles, and shows that any amount of mass contains substantial inherent energy, with the change in mass being proportional to the change in energy. This idea is central to the principles of nuclear science and technology.

$$\Delta E = \Delta mc^2 \tag{1}$$

The equation relating relativistic energy and momentum is shown in Eq. 1. Incident CR particles exhibit a large total energy, since the mass and velocity of the particles combine in the expression of kinetic energy (T). From basic kinematics, it is known that T increases rapidly with velocity (v) because of the  $v^2$  dependence.

$$T = \frac{1}{2}mv^2 \tag{2}$$

This expression holds for non-relativistic situations ( $v \ll c$ ). T may also be expressed in terms of the momentum (p) of the moving body, where  $p=mv$ , and an equivalent expression for the kinetic energy can be constructed using momentum.

For situations in which the particle velocity begins to approach the magnitude of c ( $v$  roughly  $\geq 0.1c$ ), relativistic considerations are required, in which the quantity  $\gamma$  is introduced, relating the object's velocity to the upper limit of velocity.

$$\gamma = \frac{1}{\sqrt{1 - \left(\frac{v^2}{c^2}\right)}} \tag{3}$$

and the quantity  $pc$  may then be used to find the equation for the relativistic energy, which is given by the invariant equation relating energy and momentum:<sup>8</sup>

$$E^2 - p^2c^2 = m^2c^4 \tag{4}$$

The energies of small-scale phenomena are then expressed in terms of electron-volts (eV), where one 1 Joule =  $6.24 \times 10^{18}$  eV. This equation allows the determination of  $p$  if  $E$  is known, or the determination of  $E$  if  $p$  is known.<sup>8</sup>

The kinetic energy of projectiles is the primary source for the ionization of atoms within materials. An increased level of ionization caused in a material corresponds to a reduction in the kinetic energy of the propagating particle, which ultimately slows down, loses all its energy, and comes to rest within a material. The distance required for the particle to stop is the *range*, which also may provide an estimate of the original kinetic energy of the projectile. The total initial energy may then be determined by using calibrated range-energy tables, which show the relationship between the type and energy of a particle, and the subsequent traveling distance in various materials.<sup>7</sup> Fast particles may pass all the way through a material if they are sufficiently energetic, or if the material is thin. Early research in cosmic rays focused on the determination of what energetic particles do when they pass through common materials.

Cascades and ionization have historically been studied by using photographic evidence, highly-controlled gas chambers, or the ejecta of the collisions, mainly in the form of a minute electronic current.<sup>1,7,9</sup> Vessels known as cloud chambers contain gas at controlled pressure and temperature, and after the interaction of X-rays and radioactive particles with the chamber contents, the ions produced serve as centers for condensation.<sup>1,7,9</sup> The condensed water vapor droplets are easily seen, and provide direct visual evidence of a particle's trajectory. Particle tracks have also been 'photographed' using emulsions of gelatin containing crystals of silver bromide or silver chloride, which react when exposed to light. Upon development, tiny silver grains are produced where light was absorbed, which indicate the nature of the multiple quanta of radiation that have been absorbed by the emulsion. The particle tracks then show up as a trail of tiny silver grains, which show the path of the particle through the object; the extent of ionization is revealed by the number and density of silver grains that constitute the track.<sup>1</sup> The darker and thicker the track, the higher the level of ionization imparted to the material. A very thick and grainy track also shows that ionization of atoms adjacent to the trajectory is higher than would be for the thin or faint situation.

The evidence of particle trajectories shows that the total relativistic energy, including mass and velocity, controls the level of ionization that the target material will experience. Charged particles may ionize target atoms, and the electrons produced may be energetic enough to ionize other atoms and yield secondary electrons as per the cascade mechanism discussed above. This is in addition to the possibility of nuclear collisions, which produce energetic fragments and radiation that may also ionize. In contrast, the uncharged particles such as neutrons, neutral mesons, gamma rays, and neutrinos were originally detected by the effects they produce upon decay into a charged particle, or by the ejection of charged particles from a collision. The rate at which a charged particle projectile loses energy through ionization depends on the initial charge ( $Z$ ) and velocity ( $v$ ). The produced ionization depends mainly on the ratio of  $Z^2/v^2$ . A proton is roughly 2,000 times more massive than an electron, so for the same incident velocity, the proton will be much more-densely ionizing. The situation is pictured in Figure 4, which is a comparison of the general appearance of electron and proton tracks in an emulsion. It is apparent that the electronic trajectories are much more skewed, and they have been deflected many times as they travel, because the low-mass of electrons and their charge ( $e$ ) makes them more susceptible to electric fields (thus electric forces) set up by the atoms within matter. The inverse speed dependence indicates that slow particles will ionize more heavily than fast particles, which is evident in the electronic trajectories. The electrons in Figure 4 initially produce low levels of ionization, but the tracks thicken as they are slowed and deflected by electrodynamic interactions, until they are eventually captured by an atom. In contrast, the protons display a more direct passage through, because even though protons have the same magnitude of charge as an electron, their mass makes them less susceptible to the deflection and violent accelerations of electrons as they go through the same electric fields (the charge to mass ratio  $e/m$ ). The degree of ionization is central to the behavior of the more massive charged particles as they encounter bulk matter.

The more massive particles produce very heavy tracks in photographic emulsions. The  $Z^2/v^2$  relation demonstrates that the extent of ionization for particles is more strongly dependent on mass than velocity.<sup>1,7,9,33</sup> Since  $Z$  is at a minimum for protons ( $Z=1$ ), one may readily deduce that the ionization increases rapidly because of  $Z^2$ . For an alpha

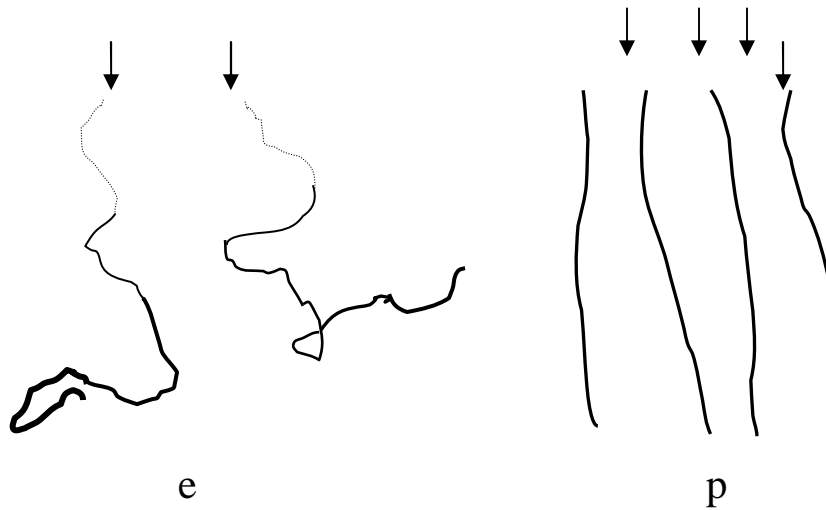


**Figure 4.** Schematic of electron (e) and proton (p) ionization tracks through photographic emulsion.

particle with  $Z=2$  (helium nucleus), the ionization is roughly 4 times as extensive, and ionization is 9 times more for  $Z=3$ . The negative effect of *very* heavy particles in the cosmic radiation could be hundreds or thousands of times that of protons. A pictorial representation of particle tracks through emulsions is shown in Figure 5 for some of the more common CR nuclei. Hydrogen nuclei are analogous to the protons of Figure 4, and though significant, we see that it creates much less ionization in its wake than even some other light nuclei, He and Li. Be, B, and C are still of relatively low mass, but begin to show very strong levels of ionization, which increases the degree of energy lost by the particles to the surrounding material. Shown here is a visual representation of the negative effects of the common heavy CR particles such as  $^{16}\text{O}$ ,  $^{27}\text{Si}$ , and  $^{56}\text{Fe}$  on materials. The heavier particles show a much larger magnitude of effects on the surrounding atoms of materials, and something as heavy as  $^{56}\text{Fe}$  exhibits immense levels of ionized atoms in its path, as well as adjacent to its track. Biological matter or solid materials would be affected similarly by these heavy projectiles; they would suffer from widespread ionization throughout their volume, with the altered atoms leading to cell damage in living organisms, or undesired effects in materials used for spacecraft.

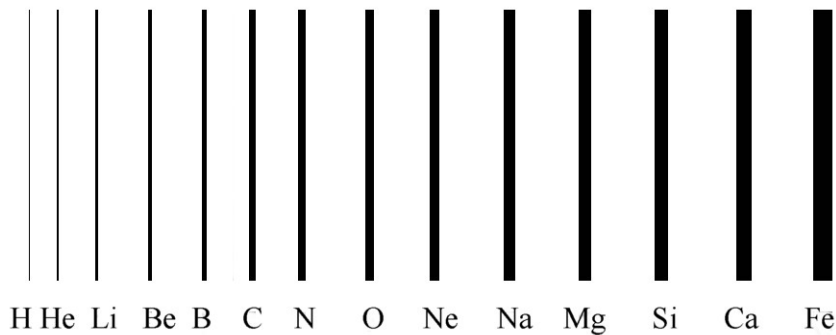


**Figure 5.** Representation of ionization tracks for projectile nuclei.

Macroscopic evidence of particle tracks in materials was provided by some of the Apollo program astronauts, many of whom passed through the Van Allen radiation belts in their travels through space.<sup>1</sup> Examination of plastic space-suit components revealed physical deformation of the materials as energetic particles passed through them. Cone-shaped deformations were seen, which were on the order of tenths of mm in length. The basic phenomenon is illustrated in Figure 6, which shows a maximum deformation cone of roughly 1 mm in length.<sup>1</sup> This visual evidence should be troubling for would-be space travelers and space mission researchers: not only does CR ionize materials and cause radiation cascades within them, the energetic radiation also has the power to physically deform targets on a scale that is in fact perceptible to human eyes.<sup>1</sup> The possibility of multiple CR effects must be fully explored by those hoping to achieve extended space travel, so that some effective strategies for radiation shielding may be developed. The characterization of consequences due to energetic radiation exposure and effective protection strategies are the goals of this work.

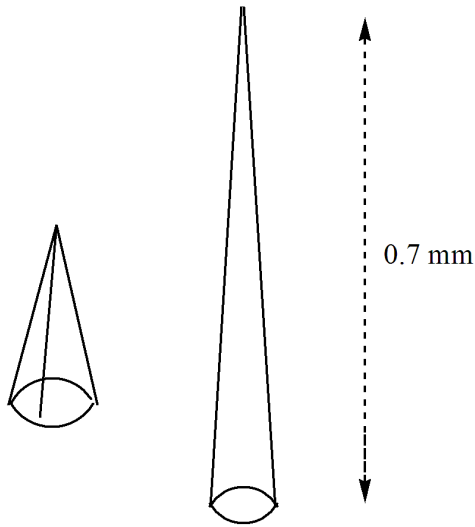


**Figure 6.** Representation of cosmic ray tracks in plastic.

The discussion of energetic particles and radiation requires some knowledge of nuclear structure, much of which has been revealed by quantum mechanics. The success of quantum mechanics in explaining atomic structure and energy levels allowed physicists to make a natural extension of these concepts to the structure of nuclei. Research in the latter part of the twentieth century showed the presence of various particles produced in nuclear experiments, such as the now-familiar electrons, protons, and neutrons, but more recent (and more advanced) experiments using higher energy have revealed a wealth of substructure within nuclei.

## **B. Basic Nuclear Structure and Properties**

One encounters much detail in the study of atomic and nuclear constituents with regard to their structure. As objects, there are divisions with regard to scale of size, mass, and the range of the force with which particles act upon their neighbors. The nuclear constituents are called protons (p) and neutrons (n), and are collectively termed nucleons, which fill and occupy increasing energy levels within the nucleus in the same way as electrons do within atoms. Taken further, nucleons are in fact objects that are each

composed of three quarks, which (strangely enough) makes the charge on a quark equal to  $+2/3$  or  $-1/3$ . Symmetry is an important concept in particle physics, so it is of note that for each particle, there is a corresponding anti-particle which has the opposite charge. There exist anti-electrons ( $e^+$ ) termed positrons, anti-protons ( $p^-$ ), and anti-neutrons, in addition to others. Generally, anti-particles are denoted by a dash above the notation for the normal particle, which for protons-antiprotons and electrons-positrons are written as  $p, \bar{p}$  and  $e, \bar{e}$ . Numerous complexities arise when dealing with elementary particles and anti-particles, the majority of which is outside the scope of this work. The focus here is to provide insight into some of the most basic nuclear properties that might be relevant or interesting to the materials scientist or engineer reading this document.

There are two types of properties that are used in the discussion of nuclear structure, these are the static and dynamic properties. The most basic static properties include electric charge, radius, mass, and binding energy. The second tier of static properties includes angular momentum, parity, the magnetic dipole and electric quadrupole moments, and the energies of excited states. The dynamic properties introduce more complexity, and examples include the decay and reaction probabilities for some nuclide. For simplicity, only the most basic of static or dynamic properties are discussed here. What is most important within this study are the energetics of particles and radiation, such as the masses of particles and basic shell structure of nuclei; these are pertinent because of mass-energy equivalence and nuclear excited states, which govern the behavior of irradiated materials. Detailed explanations of a topic such as angular momentum are left to the reader for outside study.

## **1. Static Properties**

### *i. Electric Charge*

The charge in the nucleus of an element is determined by the number of positive protons it contains. Nuclei are specified by the number of protons ( $Z$ ) within them, and an isotope of an element is specified by the number of neutrons ( $N$ ) in the nucleus; protons are positively charged and neutrons are electrically neutral. Being nuclear constituents, protons and neutrons are termed nucleons, with both particles falling within

the classification of *baryons* with spin ( $S$ ) =  $\frac{1}{2}$  in the standard model. The number of nucleons ( $A$ ) given by:  $A = Z + N$ . An isotope of element  $X$  is then  ${}^A_Z X$ . Atomic electrons each contain one unit of negative charge ( $e$ ), which has a magnitude of  $1.6 \times 10^{-19}$  coulombs (C), or  $4.80 \times 10^{-10}$  electrostatic units (esu). Electrons are often denoted as  $e^-$ , and are generally referred to as such in this text. Protons also contain one unit of positive charge ( $e^+$ ), and are denoted as  $p$  in this text. Neutrons are uncharged, and are indicated as  $n$ . Protons and neutrons are intimately connected by their interaction, and also have a similar mass. Nucleons interact at close distance through the strong nuclear force, which actually takes place between constituent quarks, and overcomes the expected coulomb repulsion between neighboring protons, and allows the nucleus to be bound.<sup>7</sup> Discussion of atoms or molecules involves internal dimensions of  $10^{-9}$  or  $10^{-10}$  m (the nanometer and Angstrom units, respectively), but nuclei are about 5 orders of magnitude smaller, which means they take up almost zero “volume” within atoms, but they are most of the mass.

In comparison to electrons, the properties of protons and neutrons are much more difficult to observe macroscopically. Typical nuclear dimensions are on the order of  $10^{-15}$  m, which is the SI unit known as the femtometer (fm) or Fermi, and any probe radiation would need to be of wavelengths of the same size or smaller than this to be useful. Energies of MeV or greater are effective but require the use of accelerators, which are not commonly accessible. To actually measure the size of the nuclei, one has to use more energetic alpha particles or electrons so that they can get closer to the potential well of a target nucleus. Of more interest to the materials scientist or engineer is the direct relationship between mass and energy, a concept that was made famous by the theories of Einstein, and is connected to the ability of humans to use nuclear technology.

## *ii. Mass and Energy*

The proton and neutron mass are comparable, and far exceed the mass of the electron. Nuclear masses are specified in terms of the unified atomic mass unit (u), which is defined so that the mass of a whole atom of  ${}^{12}\text{C}$  is exactly 12.0000 u. The result is that each nucleon has a mass of roughly 1 u. Physicists work with mass energies, rather than the actual mass quantities themselves, which is done with the conversion

factor of  $1 \text{ u} = 931.502 \text{ MeV}/c^2$ . Thus, nucleons have mass energies of roughly 1000 MeV, while electrons are fractions of MeV. Particle masses are then equivalent to an energy value in eV, with most particles of interest being in the MeV range.

Similar to the use of Planck's constant above, as an example, we consider the conversions in the use of rest mass energies for particles. The conversion from mass to energy is done using the famous result from special relativity,  $E = mc^2$ . An electron has a mass of  $9.11 \times 10^{-31} \text{ kg}$ , or  $5.485 \times 10^{-4} \text{ u}$ , neither of which are very useful numbers. Instead, what is done in problems containing the particle mass  $m$  is the insertion of the quantity  $c^2$  next to the mass, yielding the product  $mc^2$ , which is the rest mass, and thus the rest mass energy. The quantity  $1 \text{ u} = 931.502 \text{ MeV}/c^2$ , and the electron has a rest mass of 0.511 MeV. Protons have rest mass of 1.00727647 u (938.280 MeV), while neutrons are slightly larger, at 1.00866501 u (939.573 MeV). The properties of the nucleons ( $S = 1/2$  baryons) are summarized in Table II. There are also more massive baryons with  $S = 3/2$ , such as  $\Delta$ , but these particles are not typically encountered in the 1-10 GeV range of energies that are the focus of this study. Baryons are made up of different combinations of quarks, whose identities are shown in Table III. The quarks are divided into three "generations" which are classified according to the general order in which they were found (or predicted).<sup>8</sup> The first generation consists of the up (u) and down (d) quarks, the second generation are termed strange (s) and charm (c), and the most massive, elusive quarks are the bottom (b) and top (t). The electronic mass/energy contribution is usually negligible in the energetics of nucleonic collisions, though the  $\beta$ -decay and electron capture processes require knowledge of the rest mass and kinetic energies of the electrons involved. The electrons of  $\beta$ -decays typically occur with outgoing energy in the MeV range, so must be treated relativistically. These energetic electrons are commonly called delta rays.

**Table II.** Nucleons (Spin  $1/2$  Baryons).

Particle	Quark content	Charge	Mass (MeV/c <sup>2</sup> )	Lifetime (s)	Principal decays
p	uud	+1	938.280	$\infty$	--
n	udd	0	939.573	900	$p e \bar{\nu}_e$

**Table III.** Quarks (Spin = 1/2).

			<b>Mass (speculative) (MeV/c<sup>2</sup>)</b>
<b>Generation</b>	<b>Flavor</b>	<b>Charge</b>	<b>Bare</b>
1 <sup>st</sup>	d	$-\frac{1}{3}$	7.5
1 <sup>st</sup>	u	$+\frac{2}{3}$	4.2
2 <sup>nd</sup>	s	$-\frac{1}{3}$	150
2 <sup>nd</sup>	c	$+\frac{2}{3}$	1100
3 <sup>rd</sup>	b	$-\frac{1}{3}$	4200
3 <sup>rd</sup>	t	$+\frac{2}{3}$	--

For very fast speeds near  $c$ , relativistic effects regarding the frame of reference must also be taken into account. In nuclear physics experiments, there are two frames of reference, the center of mass (CM) and laboratory (L) frames. The CM frame is attached to the target nucleus, while the laboratory frame is for the projectile, moving at some speed  $v$ , for example. For speeds at a significant fraction of  $c$ , perhaps  $v \geq 0.5c$ , the time or distance coordinates at which an event is perceived must be adjusted for the moving frame, relative to the stationary frame. Many of the interactions described in this document are qualitative, so the relativistic effects on spatial coordinates have not been considered, as this is not vital to a basic grasp of irradiation effects on shielding materials.

### *iii. Strong Nuclear Force*

The strong nuclear force is exchanged between the quarks within nucleons, and has an extremely short range. The characteristics of the strong force have been deduced by nucleon-nucleon scattering experiments such as protons incident on protons (p-p), and neutrons incident on protons (n-p). Three early observations were: 1) the nuclear force

was attractive, and much stronger than the Coulomb force at short distances (the force between nucleons overcomes Coulomb repulsion of protons), 2) At long distances, on the order of  $\text{\AA}$  or atomic diameters, the nuclear force is negligible, and 3) some particles are “immune” to the nuclear force (atomic electrons display no evidence that they interact with the nuclear force at all). The strong nuclear force also shows charge independence, wherein the nucleon-nucleon interaction seems independent of whether the nucleons are neutrons or protons, so the p-p, n-p, and n-n binding interactions all take place in roughly the same manner. More advanced aspects of the strong force involve the charge, spin, and angular momentum of the interacting particles, as well as the presence of a repulsive term. The repulsive component to the strong nuclear interaction is observed at extremely short distances, and this behavior tends to keep nucleons at an average separation distance, similar to what occurs for like charges in electrostatics.

The strong nuclear interaction results in protons and neutrons being bound states of quarks, rather than single particles or objects. The dynamics of quark interactions are more complex than the scope of this discussion, but theories and evidence of so-called “virtual particles” in high-energy physics have explained much of the interaction responsible for the strong nuclear force. Quarks interact via mediators known as *gluons*. The action of each of the fundamental forces (electromagnetic, weak nuclear, and strong nuclear) occurs through these mediating virtual particles, which are displayed in Table IV. The mediator of the gravitational force is theorized to be the graviton, though this particle has yet to be observed experimentally.<sup>8</sup> The mediators for the weak nuclear force are further classified into exchanges for uncharged and charged weak interactions. Nuclei contain a great deal of energy when the quarks within nucleons and the full extent of their strong interaction is summed. The total energy contained within a nucleus (and thus, an atom) therefore includes the binding energy of the various nucleons, as well as the mass energy of the particles themselves.

**Table IV.** Mediators (Spin = 1)

Mediator	Charge	Mass (MeV/c <sup>2</sup> )	Lifetime (s)	Force	
Gluon	0	0	$\infty$	Strong	
Photon ( $\gamma$ )	0	0	$\infty$	Electromagnetic	} electroweak
W <sup>±</sup>	$\pm 1$	81,800	Unknown	(charged) weak	
Z <sup>0</sup>	0	92,600	Unknown	(neutral) weak	

*iv. Binding Energy*

The strong interaction of nucleons is responsible for most of the nuclear binding energy. The strong interaction takes place between all nucleons in proximity to each other (p-p, p-n, and n-n), so the energy of binding the atom's nuclear constituents (protons and neutrons) is considered separately from the electrons. The approximate extent of the strong interaction is a distance of fm or less. The binding energy (B) of a nucleus is the difference in mass energy between a bound nucleus and its constituent Z protons and N neutrons. The empirical formulation of the binding energy takes into account that the mass energy of a certain nuclide ( $m_N$ ) is equal to the atomic mass energy ( $m_A$ ) minus the mass of the electrons and the binding energy due to the electrons, with  $B_i$  being the binding energy of the  $i$ th electron. Atomic mass energies are typically of the order of  $A \cdot 1000$  MeV, while the binding energy for the electrons may be of the order of 10-100 keV. The electronic binding energy may be neglected in determining the mass energy of the nuclide, as its contribution is on the order of one out of  $10^6$ . The extremely small distances are also a factor in the way nucleons interact strongly.

The strong nuclear interaction takes place at very short distances, so adding protons and neutrons to a nucleus to build heavier elements must take this into account. The extent of the strong force is generally taken to be  $\leq 1$  fm, so only the closest nucleons interact with each other, which discounts the nucleons that are anything other than nearest neighbors. Also, one may imagine a lesser magnitude of strong interaction for "surface" nucleons as opposed to those internal, which have are fully surrounded full by neighbors. In addition, the empirical formulation of the terms in the binding energy also requires the

use of several constants that have been obtained from experimental evidence. The rest mass energy of a nuclide ( $m_N$ ) is given by

$$m_N c^2 = m_A c^2 - Z m_e c^2 + \sum_{i=1}^Z B_i \quad (5)$$

The binding energy ( $B$ ) for a nucleus is the difference in mass energy between some nucleus  ${}^A_Z X$  and its constituent  $Z$  protons and  $N$  neutrons.

$$B = \{Z m_p + N m_n - [m({}^A X) - Z m_e]\} c^2 \quad (6)$$

The  $Z$  protons and electrons may be grouped into  $Z$  neutral hydrogen atoms, and  $m({}^A X)$  stands for the atomic mass of isotope  $X$ .

$$B = \{Z m({}^1 H) + N m_n - m({}^A X)\} c^2 \quad (7)$$

To compare how different nuclides are bound, the binding energy is normalized so that it is expressed in terms of the number of nucleons participating in the strong interaction. One often sees the binding energy per nucleon ( $B/A$ ), for which the binding energy from Eq. 7 is divided by the mass number  $A$ . The value of  $B/A$  indicates the stability of the bound system. As shown in Figure 7, the binding energy per nucleon varies between 7 and 9 MeV/nucleon for most nuclei, and reaches a maximum around  $A = 56$  for Fe. Many nuclei feature  $B/A$  of around 8 MeV/nucleon, but it is evident from Figure 7 that  $B/A$  increases rapidly when going from  $A = 2$  to  $A = 20$ , and gradually decreases when going beyond  $A = 56$ . There are thus two ways in which energy may be extracted from nuclei. From  $A = 2$  to  $A = 56$ , energy is liberated from *fusion* reactions, while for  $A \geq 56$ , energy is given off during the *fission* of these nuclei. More on the specific energetics of these processes is given in the description of  $Q$ -values for nuclear reactions, but the distribution of possible states for nucleons may be understood in terms of the shell model, which came from similar conclusions about electrons in atoms.

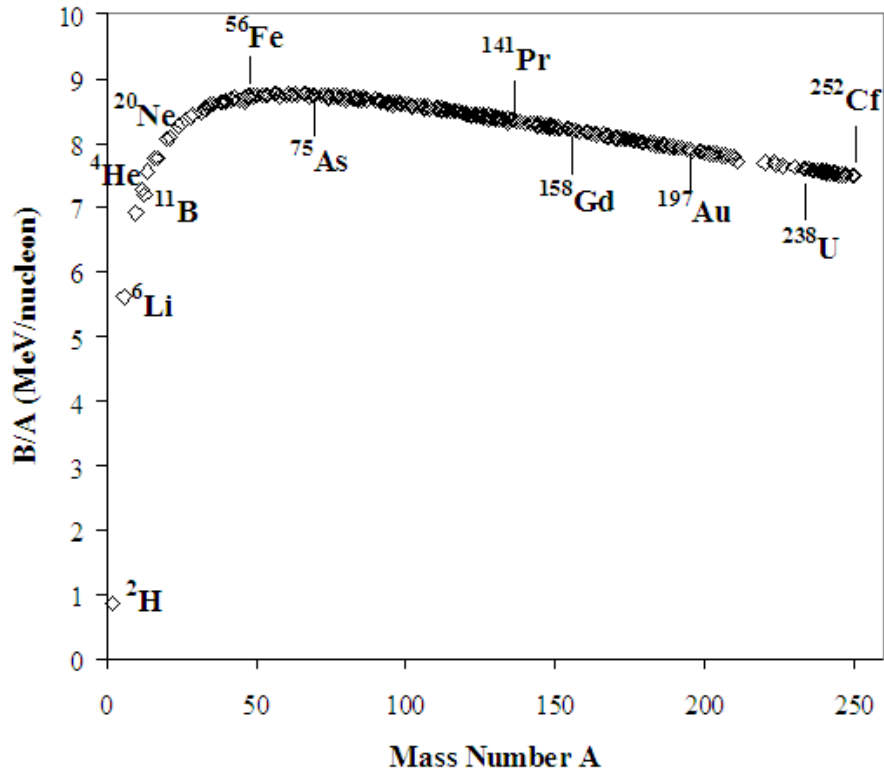


**Figure 7.** Binding energy per Nucleon

v. *Shell Model*

Atomic theories using the shell model have provided many details of atomic structure, so nuclear physicists applied quantum mechanics to nuclei in an attempt to elucidate their structure. The construction involves filling shells with electrons or nucleons of increasing energy in levels. The result is a filled core with some number of valence particles. In atoms, one sees an inert filled core and some number of valence electrons, and the model assumes that atomic and chemical properties are governed by the valence electrons. In nuclei and atoms, there is fairly smooth variation of atomic properties within each subshell and dramatic changes when going from one shell to the next. The potential in atoms is supplied by the coulomb field of the nucleus, which is an agent external to the electrons, and this is in contrast to nuclei, which move in a potential they themselves create. The nucleon-nucleon potential is set up by the nearest neighbors, so the maximum force is experienced when a nucleon's surroundings are saturated.

Experimental evidence showed sudden and discontinuous behavior at the same proton or neutron numbers, which provided evidence of a series of filled energy levels. The subsequent ordering demonstrates what are known as the “magic numbers”, with  $Z$  or  $N = 2, 8, 20, 28, 50, 82, 126$ . The nuclear subshells are filled in the order of increasing energy. The energy level schemes that were originally deduced for simpler potentials such as the Harmonic oscillator or square well showed agreement with the early magic numbers for the filled shells, but discrepancies appeared after  $N$  or  $Z = 28$ , so it was known that the simpler potentials were somehow incomplete. The results were improved in the early 1950s by recognizing a contribution to the potential that comes from the coupling of spin and angular momenta for nucleons in their orbitals.

In the late 1940s, M.G. Mayer and co-workers were the first to elucidate much of the underlying shell structure, by including a term in the nuclear potential due to interacting angular momentum between the orbital and the single, odd nucleon.<sup>7,34</sup> This is known as the spin-orbit potential, which serves to split some of the closer-lying levels into multiple states. The resulting energy levels agree with experimental evidence in that they give the magic numbers exactly, and so are applicable to all nuclei. The level structure is depicted in Figure 8, with the spin assignment for the odd nucleon shown on the left, the magic numbers displayed in the middle, and the nucleon occupation numbers shown at the right of each level.

For materials scientists or engineers without much background in nuclear physics, familiarity with the concepts of electronic shell structure enables application and understanding of how nuclei behave when energy is transferred to them. Nucleons are promoted to excited states due to transferred energy, and the de-excitation by gamma ray emission is similar to photon emission by electrons in atoms. Some of these similarities might be the probability of a reaction producing a certain excited state, the half-life of that state, or the probability/lifetime of the gamma emission. It is relatively straightforward to determine some of the characteristics of a nucleus by organizing its nucleons into the available levels.

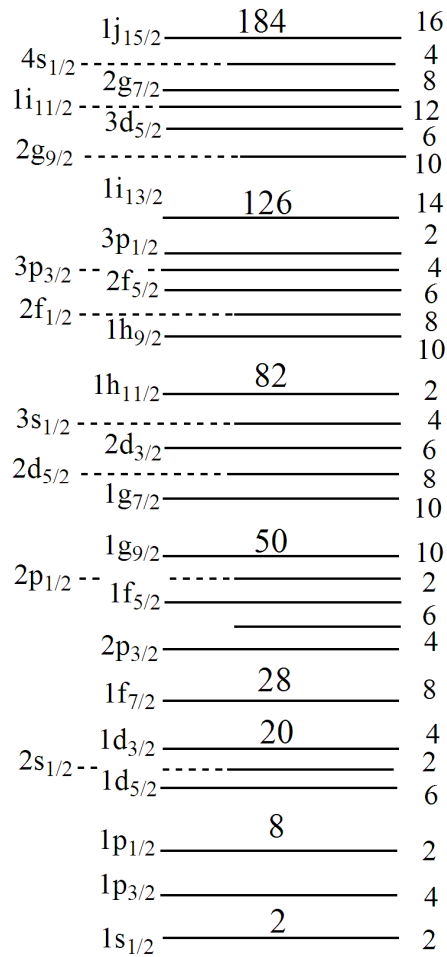


**Figure 8.** Nuclear energy levels and shell structure obtained with the spin-orbit interaction.<sup>7,34</sup>

To use the diagram, we may consider an example such as the <sup>27</sup>Al nucleus, which has odd Z, but even N. From Figure 9, one may immediately notice that A = 27, which is one less than the magic number of 28. There are 13 protons, since Z = 13, so N = 14, and there are in fact two types of available levels, with one set being for p and the other for n. To assemble a nucleus of <sup>27</sup>Al, one starts at the bottom level (1s<sub>1/2</sub>), and fills the levels with the number of nucleons that should occupy each. For Z = 13, and by knowing the occupation and magic numbers, one obtains the following scheme: 2 protons in 1s<sub>1/2</sub>, 4 protons in 1p<sub>3/2</sub>, and 2 protons in 1p<sub>1/2</sub> gives a total of 8, so there are 5 protons left. The 1d<sub>5/2</sub> level can accept 6 protons, so the remaining protons enter this level, but there is one ‘hole’ within, so that the properties of the ground state of <sup>27</sup>Al are determined by the odd

proton. For neutrons ( $N = 14$ ), the levels are filled the same way, so the  $1s_{1/2}$ ,  $1p_{3/2}$ ,  $1p_{1/2}$ , and  $1d_{5/2}$  levels are all fully occupied, and the properties of the ground state are not governed by level structure of the neutrons.

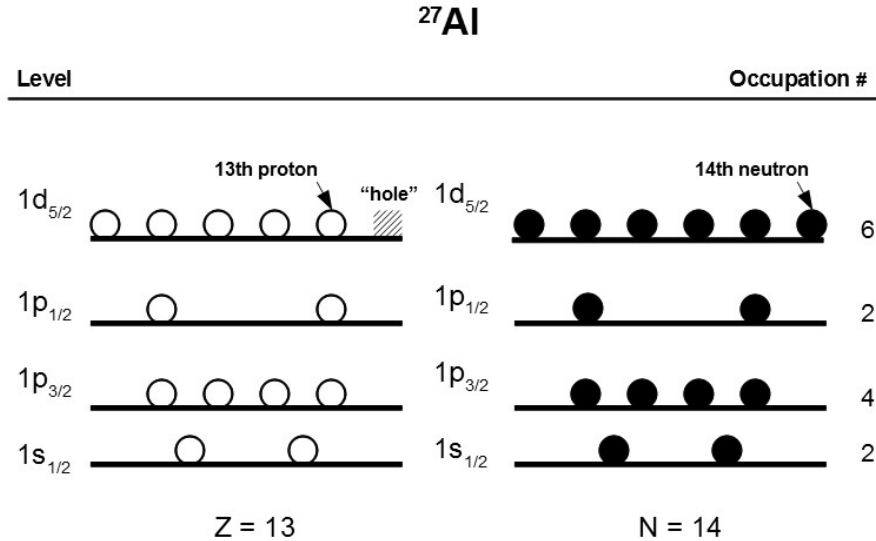


**Figure 9.** Filled proton and neutron levels in  $^{27}\text{Al}$ .

The nuclear energy shell structure is analogous to that observed for atomic electrons, so nuclear excited states and relaxation phenomena might be studied in a similar fashion. The energy levels depicted in Figure 8 and Figure 9 are on the order of and are separated by MeV, as opposed to the eV-keV seen for atomic electrons. The subsequent transitions between levels are on the order of MeV, and there is the possibility that nucleons can be excited due to the energy that might be transferred in, for example, an inelastic collision. In addition, many nuclei may feature rotational excited states that occur from the conservation of angular momentum between projectile particles and target nuclei. The promotion to higher energy states commonly results in the emission of  $\gamma$ ,  $p$ , or  $n$  upon subsequent de-excitation. The meaningful discussion of nuclear interactions requires basic understanding of the shell model, since incoming energy will promote nucleons to higher energy states. How a nucleus will behave when it reaches some

excited state is a more complex matter which depends on the lifetime of the excited state and the probability of the decay mechanism.

## C. Dynamic Property - Radioactive Decay

### 1. Systematics

For the nuclei within irradiated target materials, a dynamic property of interest is radioactive decay. If some sample of matter has  $N$  radioactive nuclei at some time  $t$ , and if no new nuclei are being introduced to the sample, then the number ( $dN$ ) decaying in a time  $dt$  is proportional to  $N$ , so

$$\lambda = \frac{(-dN/dt)}{N} \quad (8)$$

where  $\lambda$  is a constant called the disintegration or decay constant. The right-hand side of Eq. 8 is the probability per unit time for the decay of an atom. The basic assumption of the statistical theory of radioactive decay is that this probability is a constant, regardless of the age of the atoms. Integrating Eq. 8 leads to the exponential law of radioactive decay

$$N(t) = N_0 e^{-\lambda t} \quad (9)$$

where  $N_0$  is the constant of integration and gives the original number of nuclei at time  $t = 0$ . The half-life ( $t_{1/2}$ ) gives the time necessary for half of the nuclei in the sample to decay, so for  $N = N_0/2$ ,

$$t_{1/2} = \frac{0.693}{\lambda} \quad (10)$$

Also useful is to consider the mean lifetime ( $\tau$ ), which is defined as the average time that a nucleus is likely to survive before it decays. The number of nuclei that survive to time  $t$  is  $N(t)$ , and the number that decay between  $t$  and  $t + dt$  is  $\left| \frac{dN}{dt} \right| dt$ , so the mean lifetime is

then

$$\tau = \frac{\int_0^{\infty} t |dN/dt| dt}{\int_0^{\infty} |dN/dt| dt} \quad (11)$$

the denominator gives the total number of decays, and evaluation of the integrals yields

$$\tau = \frac{1}{\lambda}, \quad (12)$$

so the mean lifetime is the inverse of the decay constant. In addition to the lifetime of the decaying state, there is concern as to *how* radioactive some sample is relative to another. Discussion of this feature of radioactivity is done by defining the *activity* of a sample

The activity of a radioactive substance is defined to be the rate at which decays occur in the sample. The expression for activity also takes the exponential form:

$$A(t) = \lambda N(t) = A_0 e^{-\lambda t} \quad (13)$$

and the initial activity at  $t = 0$  is  $A_0 = \lambda N_0$ . The activity of a radioactive sample is thus the number of decays of the sample per unit time. To put activity into useful units, one considers the number of disintegrations (decays) per unit time. Radioactivity is expressed in terms of the curie unit (Ci), which is the activity of one gram of radium, and is equal to  $3.7 \times 10^{10}$  decays per second. The SI unit is the Becquerel (Bq), which is equal to one decay per second. Such measurements of activity are applicable to all of the known radioactive phenomena, though the ways in which nuclei disintegrate may vary. A nucleus with constituents in higher energy states may decay by emission of gamma rays, whereas a nucleus with a neutron or proton excess might reduce its mass instability by emitting a particle such as an alpha particle. The lifetime would then refer to either the length of time that the excited state exists prior to the gamma de-excitation or particle emission.

## 2. Decay Processes

Nuclei are unstable if there is an existing physical process that enables nucleons to settle into a more tightly bound state with a lower total rest energy. A nucleus will eventually decay into that lower-energy state, again analogous with atomic electrons.

Lower-energy states generally exist for a nucleus if: 1) it has roughly the right mix of protons and neutrons, but the nucleus is so large that excessive coulombic repulsion between protons makes it energetically favorable for the nucleus to fragment into smaller pieces ( $\alpha$ ), 2) it doesn't have the optimal mix of protons and neutrons ( $\beta$ ), or 3) there is a nucleon that is in an energy level higher than the lowest level available to that nucleon ( $\gamma$ ). These are the alpha, beta, and gamma ( $\alpha$ ,  $\beta$ , and  $\gamma$ ) decays.

### *i. Alpha Decay*

The  $\alpha$  decay mechanism is the emission of a fairly energetic helium nucleus,  ${}^4\text{He}$ . The  ${}^4\text{He}$  nucleus can be the agent of such a process because it is a tightly-bound system.<sup>7</sup> We may consider the  ${}^{226}\text{Ra}$  nucleus as an alpha-emitter, which displays  $3.7 \times 10^{10}$  disintegrations per second, and decays into radon gas,  ${}^{222}\text{Rn}$ . The Curie unit of radioactivity was previously defined as the amount of radioactive matter that has the same disintegration rate as 1 gram of  ${}^{226}\text{Ra}$  (37 GBq). For the process of  $\alpha$  emission by the  ${}^{226}\text{Ra}$  nucleus, we have



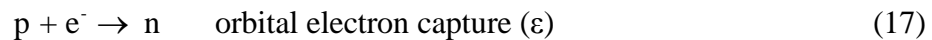
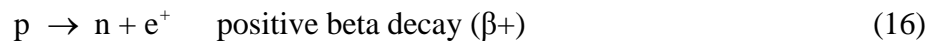
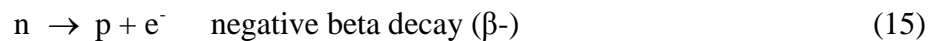
For the radium nucleus,  $t_{1/2} = 1600$  years, and the  $\alpha$  particle exits with a kinetic energy of 4.8 MeV. Alpha emission is a way for a heavy, unstable nucleus to remove excess energy by emitting a stable, energetic particle. The  $\alpha$  emission mechanism is increasingly important for the heavier nuclei, as the Coulomb interaction increases rapidly in comparison to the nuclear binding. Coulomb repulsion increases with size roughly as  $Z^2$ , while the nuclear binding force increases proportional to  $A$ . The spontaneous emission of an alpha particle may be favored in some instances to minimize the amount of mass lost, while maximizing the energy release;  ${}^4\text{He}$  is very tightly bound, has low mass, and is emitted with anywhere from 1 to 10 MeV kinetic energy.

Alpha decay was a process that was readily explained by the inherent statistics and probabilities of quantum mechanics. The idea is that a fully-formed  ${}^4\text{He}$  particle pre-exists in the nucleus, and there is a statistical probability for it to “leak out” of the nuclear

potential well via quantum mechanical tunneling. The wave function of the particle has some probability of being outside the confines of the nuclear coulomb barrier, though it is very low. In fact, it has been determined that the alpha particle must present itself to the barrier more than  $10^{30}$  times before it might leak out as an energetic alpha particle.<sup>7</sup> Many large nuclei, such as isotopes of uranium like  $^{232}\text{U}$ , release their maximum amount of energy via an alpha particle. In  $^{232}\text{U}$ , the emission of any other type of particle (n,  $^1\text{H}$ ,  $^2\text{H}$ ,  $^3\text{H}$ ,  $^3\text{He}$ ,  $^5\text{He}$ ,  $^6\text{Li}$ ,  $^7\text{Li}$ ) leads to an endothermic situation and negative energy release. Only the  $^4\text{He}$  emission is energetically favorable, and releases +5.41 MeV, which allows the decay. However, alpha decay is not favored in many of the lower-Z elements that are the focus of current radiation shielding studies; the dominant mechanisms for the lighter nuclei fall within the class of  $\beta$  decay.

## *ii. Beta Decay*

There are three types of Beta decay processes, which change both Z and N by one unit, and lead to a more stable isotope for that nucleus. The possibilities are the decay of a free neutron into a proton ( $\beta^-$ ), the decay of a proton into a neutron ( $\beta^+$ ), and the conversion of a proton into a neutron via orbital electron capture (denoted  $\epsilon$  or EC). The free neutron is unstable against  $\beta$  decay, and has a half-life of roughly 10.6 minutes. As shown in Equations 15-17, the basic processes within the  $\beta$  decay classification are

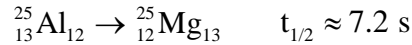


but each process also involves another particle, either a neutrino or antineutrino, which (along with electrons) are in what is known as the lepton family of particles. Each type of lepton has its own identifying number. In Eqs. 15 through 17 above, we see the presence of electrons and a positron within ( $\beta^+$ ). The presence of the electron on the right-hand side of the ( $\beta^-$ ) reaction and the left-hand side of  $\epsilon$  require the conservation of lepton number on the opposite side.

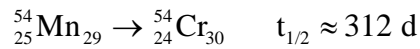
1. Neutron decay ( $\beta^-$ ) – Lowers N/Z



2. Proton decay ( $\beta^+$ ) – Raises N/Z



3. Electron capture – Raises N/Z



The changes which occur in the nucleus are balanced by the presence of an electron, neutrino, or anti-neutrino within the scheme of the reaction. A does not change, but Z and N may differ for the final nucleus. The decay of a neutron means N is decreased by one, which makes a proton appear and Z increases by one. Proton decay has the opposite effect, which means that a proton is changed into a neutron, with Z-1 and N+1 on the product side of the reaction. Neutron decay yields an electron and anti-neutrino as products, whereas proton decay causes a positron and a neutrino to appear. In electron capture, an electron gets close to and is absorbed by the nucleus, which causes a neutrino to be emitted, and one of the protons is then converted into a neutron; we then see Z-1 and N+1 in the product. Electrons and neutrinos are elementary particles, in that they themselves are not composed of anything else, whereas nucleons are composed of multiple quarks. Electrons and neutrinos are classified within the lepton family of elementary particles, so reactions must include conservation of lepton numbers to be balanced.

### iii. *Beta Decay and Leptons*

The Beta decay processes reveal some reaction components as belonging to what is termed the lepton group within the standard model of particle physics. Particle physics turns complex rather quickly, but the conservation of lepton number (L) is a relatively straightforward concept. The leptons are the electrons (e), muons ( $\mu$ ), and tau particles ( $\tau$ ), with the corresponding anti-particles being termed anti-leptons. L is +1 for leptons, -1 for anti-leptons, and L = 0 for non-leptons. Total lepton number is separately conserved for each type of lepton in particle interactions or decays, so for e and  $\mu$ , one would see electron, muon, and tau lepton numbers, which are  $L_e$ ,  $L_\mu$ , and  $L_\tau$  respectively. The total number of leptons minus antileptons on each side of a reaction or decay must be the same. To observe the conservation of lepton numbers, we consider the decay of a muon ( $\mu^-$ ) by



$L_e$  and  $L_\mu$  must have the same value on both sides of the decay equation. The negatively-charged muon has no electron lepton number associated with it, so  $L_e = 0$  and  $L_\mu = +1$  on the left-hand side.  $L_e$  must then equal zero, and  $L_\mu$  must equal +1 for the right-hand side. We see that the product electron gets assigned +1, but the electron anti-neutrino product has L = -1, so the right side sums to zero as expected:

$$\begin{array}{rcccc} & \mu^- \rightarrow & e^- & + & \bar{\nu}_e & + & \nu_\mu \\ L_e = & & 0 & & +1 & & -1 & & 0 \\ L_\mu = & & +1 & & 0 & & 0 & & +1 \end{array}$$

There are in fact three types of neutrinos, each associated with one of the above particles: there are the electron ( $\nu_e$ ), muon ( $\nu_\mu$ ), and tau ( $\nu_\tau$ ) neutrinos, which are indicated by the subscript as shown, and depend on the exchange part of the interaction. The lepton family is summarized in Table V. Some details of leptons as well as  $\alpha$  and  $\beta$  beta decay have been presented because they are tractable, but gamma emission is quite different, with details that are outside the scope of traditional materials chemistry or engineering.

**Table V.** Leptons (Spin 1/2)

Lepton	Charge	Mass (MeV/c <sup>2</sup> )	Lifetime	Principal decays
e	-1	0.511003	$\infty$	--
$\nu_e$	0	0	$\infty$	--
$\mu$	-1	105.659	$2.197 \times 10^{-6}$	$e \nu_\mu \bar{\nu}_e$
$\nu_\mu$	0	0	$\infty$	--
$\tau$	-1	1784	$3.3 \times 10^{-13}$	$\mu \nu_\tau \bar{\nu}_\mu, e \nu_\tau \bar{\nu}_e, \rho \nu_\tau$
$\nu_\tau$	0	0	$\infty$	--

#### *iv. Gamma and Other Decays*

High-energy bombardment of matter will produce some population of excited nuclear states in the target, from which gamma decay may occur. At some level, gamma decay may be understood by drawing analogy to the excitation of atomic electrons. An excited electron decays to a more stable state via the emission of a photon, with an example being the visible light given off from luminescent materials when exposed to UV radiation. The correct analysis of gamma ray emission requires the determination of the most prevalent electric (EL) or magnetic (ML) multipole transitions, which are derived from the electromagnetic fields inherent from the nuclear charge distribution.  $L$  is the order of the multipole operator that is used to calculate the decay probability from a time-varying electric or magnetic multipole moment, The decay probability is for the transition of a nuclear state ( $\psi$ ) from  $\psi_i$  to  $\psi_f$ . Angular momentum and parity changes also lead to selection rules for the transitions, as for electronic transitions in atoms. The lower-order multipole transitions are generally the most favored, and one generally sees them labeled as E1, E2, (electric multipole of first and second orders), or M1, M2, etc. The details are too complex for inclusion here, but some of how energy may be imparted to nucleons is discussed below. Gaining proximity to or exciting nucleons requires incident projectiles that are at least MeV in energy, which is achieved with particle accelerators.

Outside of alpha, beta, and gamma decay, there are two other decay processes that are worth mentioning here, though the details are omitted. The mass stability of the

nucleus is one of the determining factors that leads to either spontaneous fission, or the actual emission of nucleons. A very massive nucleus with a neutron excess may by spontaneous fission split roughly in half, resulting in two lighter nuclei. The product nuclei may not be known exactly; the products are in fact statistically distributed over the entire weight range of the medium-weight nuclei. Examples that may disintegrate in this fashion are the extremely heavy nuclei  $^{256}\text{Fm}$  ( $t_{1/2} = 2.6$  h), and  $^{254}\text{Cf}$  ( $t_{1/2} = 60.5$  d), both of which are uncommon in nature. For nuclei with a neutron excess, the heavy nuclei may release one or more free neutrons, which changes the mass numbers of the final fragments, and may produce stable, tightly bound products.

Often the heavier isotopes of some nucleus reside outside the stable ‘valley’ of masses for that nucleus. Further away from the valley, excess mass causes inherent energy differences for the heavy nuclei in comparison to the stable, lighter nuclei. If the energy difference exceeds the nucleonic binding energy, which is roughly 8 MeV, it may be possible to have radioactive decay by nucleon emission. This process occurs most often in fission products that feature a very large neutron excess.

There are several ways for energy to be released or emitted by excited nuclei, but the  $\alpha$ ,  $\beta$ , and  $\gamma$  decays are the most relevant to the results of this study. Radiation bombardment of target materials is likely to cause excited states in their nuclei and the emission of energetic particles and gamma rays. The target materials are generally of low  $Z$ , so spontaneous fission is not an issue, while nucleon emission is not as common as the three dominant modes of decay.

#### **D. Nuclear Interactions**

The study of energetic nuclear reactions is required for those that would delve into astrophysics, as well as for those in the fields of nuclear power generation or nuclear engineering. There is a possibility for nuclear reactions any time energetic particles hit matter. Energetic particles may be produced via reactors, accelerators or radioactive isotopes, and nuclear reactions produce widely-varying phenomena depending on the kinetic energy of the incident particle. There are three energy ranges to be considered in the study of nuclear reactions: low energy of less than 10 MeV is most common in nuclear physics, medium energy is from 100 MeV to 1000 MeV, wherein the situation is

complicated by meson production and the possibility of protons and neutrons transforming into each other. Incident energies greater than 1 GeV/nucleon are the domain of particle physicists, in which there may be many exotic particles produced.<sup>7-9</sup>

The probabilistic aspects of nuclear behavior require the use of interaction cross sections, which are a rough measure of the probability of occurrence for some reaction. The cross sections for products of interest may in fact vary significantly within *each* energy range, as well as when going from low- to high-energy, that is when increasing from 1 MeV to 1 GeV per nucleon. The bulk of early work in nuclear physics dealt with the interaction of light particles (nucleons,  $e^-$ ,  $A \leq 4$ ) with target materials, but there is currently much interest in bombardment with heavier nuclei, which is highly-relevant to any study of cosmic rays. Unfortunately, since solar modulation limits most cosmic ray particles to  $\leq 1$  GeV/nucleon, there is the need for familiarity with the processes that might occur for all three energy ranges, but much of the work in cosmic ray bombardment is limited to hundreds of MeV to 1 GeV/nucleon, which makes the problem a bit more tractable. However, the reader should be aware that the field of traditional nuclear physics, with a focus on low-energy interactions, has likely reached its apex in modern times. Most of the current attention has been shifted to particle physics, with simulations and experiments done well above the GeV range of incident energies.

## 1. Tools for Investigating Nuclear Reactions

### *i. Q Values*

Nuclear physics and reactions have been very well-studied since the latter part of the nineteenth century, and tools have been developed to extract information from materials or beams of interest. The important properties of nuclear reactions are primarily dependent on the energies and masses of the incident and target nuclei and exchanged particles, as well as the probability of a specific product or emitted particle to appear. Nuclear reactions are written as



which is more simply denoted as X(a,b)Y. X and Y are the target and product nuclei, respectively, while a is the incident particle, and b is the particle that is emitted. The (a,b) part of the notation may be thought of as the ‘exchange’ of particles that occurs during the reaction. From conservation of total relativistic energy, the Eq. 22 yields

$$m_X c^2 + T_X + m_a c^2 + T_a = m_Y c^2 + T_Y + m_b c^2 + T_b \quad (23)$$

where the T is the kinetic energy and m the mass of the interacting species. Changes in mass (m) and energy (E) are related by

$$\Delta E = \Delta m c^2$$

with c equal to the speed of light. Any change in the kinetic energy of the system of reacting particles must be balanced by an equal change in the system’s rest energy. The Q-value is an important quantity that is used in the study of nuclear reactions, with the value being given by Eqs. 24 or 25:

$$Q = (m_{\text{initial}} - m_{\text{final}})c^2 \quad (24)$$

$$Q = T_{\text{final}} - T_{\text{initial}} \quad (25)$$

with m equal to the rest mass energy of the nuclei under consideration. Stated in a different way,

$$Q = (m_X + m_a - m_Y - m_b)c^2 \quad (26)$$

$$Q = T_Y + T_b - T_X - T_a \quad (27)$$

If  $Q > 0$  ( $m_i > m_f$  or  $T_f > T_i$ ) the reaction is termed exoergic or exothermic, and nuclear mass or binding energy is released as the kinetic energy of the final products. If  $Q < 0$  ( $m_i < m_f$  or  $T_f < T_i$ ), the reaction is endoergic or endothermic, and some of the initial kinetic energy is converted into nuclear mass or binding energy. The third possibility is that  $Q = 0$ . There are also two reference frames of interest in such experiments: the laboratory frame and the center of mass frame.

For projectiles moving at very fast speeds near  $c$ , relativistic effects regarding the frame of reference must also be taken into account. In nuclear physics experiments, there are two frames of reference, the center of mass (CM) and laboratory (L) frames. The CM frame is attached to the target nucleus, while the laboratory frame is for the projectile, moving at some speed  $v$ , for example. The situation is shown in Figure 10 for the reaction of Eq. 22.

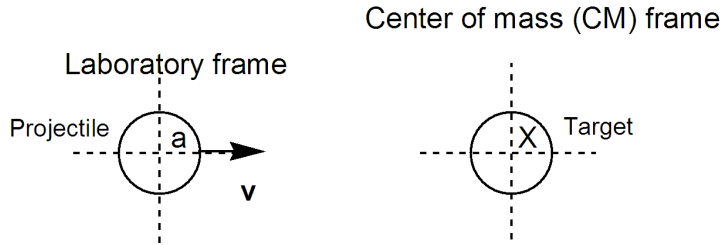


**Figure 10.** Laboratory and center of mass frames

For speeds at a significant fraction of  $c$ , perhaps  $v \geq 0.5c$ , the time or distance coordinates at which an event is perceived must be adjusted for the moving frame, relative to the stationary frame. Throughout this study, relativistic effects are not vital in understanding the qualitative effects of GeV irradiation on the simulated shielding materials. In the laboratory frame, the target nuclei are considered to be at rest. The inherent room-temperature thermal energy of the nucleons is negligible compared to the MeV scale of nuclear reactions, but additional energy may be imparted by the collision, which would then appear as an excited nuclear state.

In the study of reactions, a specific sequence or product may be more likely than another, so the use of interaction cross-sections is helpful to categorize the likelihood of certain phenomena. For example, irradiation of aluminum by MeV protons might produce neutrons, where the exchange part of the reaction is  $^{27}\text{Al}(p,n)$ , and the cross section deals with the statistical probability of observing neutrons at some angle. At higher energy, GeV protons would produce pi-mesons, also known as pions ( $\pi^\pm$  for charged,  $\pi^0$  for uncharged), where the experimenters would be concerned with  $^{27}\text{Al}(p,\pi^\pm)$  or  $^{27}\text{Al}(p,\pi^0)$ .

*ii. Cross sections*

The cross section ( $\sigma$ ) is used in prediction and experimentation that deal with nuclear reactions. A cross section takes into account the geometry of the scattering center, as well as the probability that some outgoing particle is scattered in a given direction. The cross section can be taken as a measure of the relative probability for a nuclear reaction to occur.

To calculate or measure cross sections, the geometry of the scattering center is assumed to be spherical, as is the description of the scattered particle current. The spherical coordinate system is used as specified by physicists, in which the angle  $\theta$  is taken from the z-axis to the vector  $\mathbf{r}$ , while the angle  $\phi$  opens from the x-axis to  $\mathbf{r}$  as shown in Figure 11. The unit of solid angle is the steradian, which is used extensively in physics and astronomy.

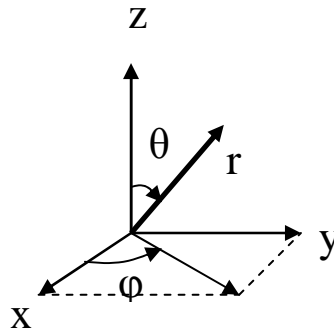


**Figure 11.** Spherical coordinate system.

For a scattering experiment, as shown in Figure 12, the goal is to determine the direction in which the scattered particle travels. The number of particles scattered into some solid angle  $d\Omega$  is the quantity of interest, in comparison to the number of particles from the incident flux impinging on a unit area.

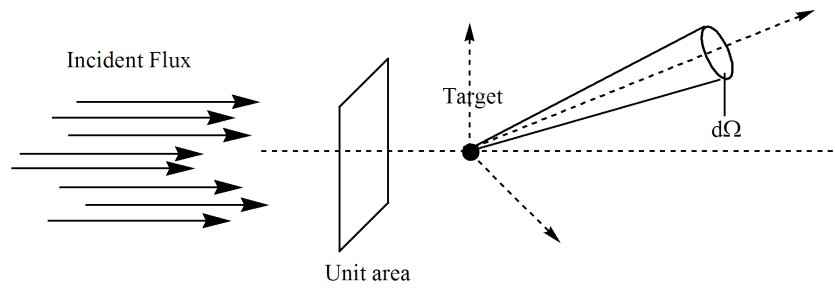


**Figure 12.** Geometry of scattering cross sections.

The impact parameter ( $b$ ) is defined as the minimum distance between the incident particle and the target particle if there were no deflection. For a group of three hypothetical particles (1, 2, 3), with impact parameters  $b_1$ ,  $b_2$ , and  $b_3$ , the situation for the impinging particles is shown in Figure 13.

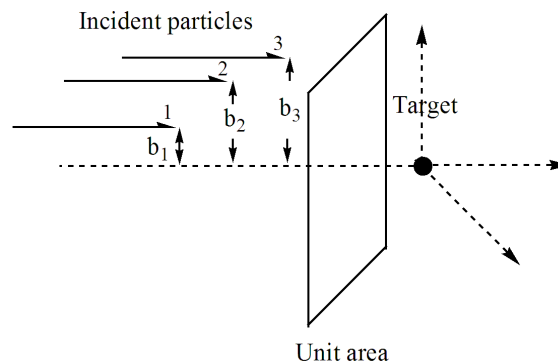


**Figure 13.** Impact parameters for different particles impinging on a target nucleus.

For an irradiated target, which can be either a single nucleus or slab of material, and for some flux ( $F$ ) of incident particles per unit area, scattering cross sections may be determined by considering the number of particles scattered into the solid angle  $d\Omega$  per unit time. Due to inherent randomness in impact parameters ( $b$ ) for a number of particles, as shown in Figs. 12 and 13, the number of particles scattered into  $d\Omega$  will vary for different time intervals of measurement. If the statistics of many finite measuring periods are averaged, the number tends toward a fixed value of  $dN_S/d\Omega$ , where  $dN_S$  is the

average number of particles scattered per unit time. The differential cross section is defined as the ratio

$$\frac{d\sigma}{d\Omega}(E, \Omega) = \frac{1}{F} \frac{dN_s}{d\Omega} \quad (44)$$

and is a function of the energy (E) of the incident particles that make up the flux. The quantity  $d\sigma/d\Omega$  represents the average fraction of incident particles that are scattered into  $d\Omega$  per unit time and per unit flux F. The total cross section for any scattering at an energy E is defined as the integral of  $d\sigma/d\Omega$  over all solid angles:

$$\sigma(E) = \int d\Omega \frac{d\sigma}{d\Omega}$$

This explanation of cross sections provides a basic visual picture, but is not practical for most cases of experimentation. In real situations, the target is a slab of material with many scattering centers. The quantity of interest then becomes the number of centers per unit perpendicular area, with

$$\frac{\text{\# centers}}{\text{unit perpendicular area}} = N\delta x \quad (x)$$

where N is the density of centers (areal density in  $g/cm^2$ ), and  $\delta x$  is the thickness of the material along the direction of the beam. If A is the total perpendicular area of the target, then the number of particles eligible for an interaction is F x A:

$$N_s(\Omega) = FAN\delta x \frac{d\sigma}{d\Omega} \quad (x)$$

and the total number scattered into all angles is similarly

$$N_{tot} = FAN\delta x\sigma \quad (x)$$

If the geometrical dimensions of the particle beam are smaller than the target, then A is the area of the target covered by the beam, and  $F \cdot A$  approaches  $n_{inc}$  which is the total

number of incident particles per unit time. Dividing by  $F \cdot A$  gives the probability for scattering a single particle in a thickness of  $\delta x$ :

$$\text{Probability of interaction in } \delta x = N\sigma\delta x \quad (\text{xx})$$

The total cross section (in  $\text{cm}^2$ ) for a number of events ( $N$ ) is

$$\sigma = \frac{N_{\text{events}}}{(\text{beam particles per unit area}) \times (\text{target particles})} \quad (\text{Xx})$$

Partial cross sections may also be defined, such as  $\sigma_{\text{elastic}}$ ,  $\sigma_{\text{inelastic}}$ ,  $\sigma_{\text{fission}}$ ,  $\sigma_{\pi \text{ production}}$ .  $N_{\text{events}}$  may also be restricted to the case in which an outgoing particle goes into a particular range of angles in space (e.g. into a specific detector of finite size). In this case, the differential cross section ( $d\sigma/d\Omega$ ) may be defined such that

$$N_{\text{events into solid angle } \Delta\Omega} = N_{\text{incident}} \times \frac{d\sigma}{d\Omega} \Delta\Omega$$

with  $d\Omega = \sin\theta \, d\theta \, d\phi$ , which is the infinitesimal element of solid angle measured in steradians (sr).

A cross section is therefore a measure of the effective surface area seen by the impinging particles, and is expressed in units of area. Cross section data are expressed in terms of barns (b), where  $1 \text{ b} = 10^{-24} \text{ cm}^2$ , but millibarns (mb,  $10^{-27} \text{ cm}^2$ ) and microbarns ( $\mu\text{b}$ ,  $10^{-30} \text{ cm}^2$ ) are also seen in the literature. The cross section of two particles (i.e. observed when the two particles are colliding with each other) is a measure of the interaction event between the two particles.

For those conversant with classical kinematics, it is known that energetic particles might convey some of their energy to a target during a collision, but for a situation other than a nuclear reaction, such as for particles in a bound nucleus, it is known that the particles must interact with their neighbors in order to stay together. There is much interest in knowing *how* the particles interact with each other, which leads to a brief discussion of the strong nuclear force, and the exchange that occurs between particles to cause the strong interaction.

## E. Mesons

A step beyond nuclear reactions, the threshold of particle physics begins when incident particles contain several hundred MeV or more of kinetic energy. More and more exotic species of elementary particles are observed when increasing the reaction energetics to the GeV range. The *meson* has the lowest mass of any strongly-interacting particle, and mesons are two quark objects, being composed of a quark and an antiquark which exist briefly in a bound state. Mesons and baryons both belong to the group called *hadrons*, which applies to any multi-quark object that interacts via the strong nuclear force. There are numerous particles that show up in when sampling with MeV energy or above, these are divided into three major categories, which are the meson, lepton, and baryon families. Electrons and neutrinos fall within the family of leptons, and nucleons are classified as baryons. Some of meson physics is useful to those studying space radiation at incident energies of 1 GeV and above because of the potential for changes in the nuclei of target or shield materials.

**Table VI.** Quarks (Spin ½)

Gen.	Flavor	Charge	Bare	Mass (MeV/c <sup>2</sup> ) (speculative)	
					Effective
				In baryons	In mesons
1 <sup>st</sup>	d	$-\frac{1}{3}$	7.5	} 363	} 310
1 <sup>st</sup>	u	$+\frac{2}{3}$	4.2		
2 <sup>nd</sup>	s	$-\frac{1}{3}$	150	438	483
2 <sup>nd</sup>	c	$+\frac{2}{3}$	1100	1500	
3 <sup>rd</sup>	b	$-\frac{1}{3}$	4200	4700	
3 <sup>rd</sup>	t	$+\frac{2}{3}$		> 23,000	

*i. Properties of Pi-mesons*

The mesons are known as ‘virtual’ particles, and what is observed is the force that results from the exchange of virtual particles, but not the particles themselves. The exchanged particle must have integral spin (0 or 1) and some electric charge. A suitable analogy for the exchange of virtual particles is the coulomb interaction between electric charges; this force can be regarded as the exchange of virtual photons. The exchanged particles that carry the nuclear force are the mesons. At the simplest level, mesons are composite structures consisting of a quark and an anti-quark. Experimental results have shown that there must be 3 pions with +1, 0, and -1 charge; all pions have 0 spin. The resulting pions are the  $\pi^+$ ,  $\pi^-$ , and  $\pi^0$ . The  $\pi^\pm$  have rest mass of 139.6 MeV, while  $\pi^0$  has a rest mass of 135.0 MeV. Pion exchange can transform a neutron into a proton with  $\pi^-$ , or a proton into a neutron with  $\pi^+$ , which can easily be shown qualitatively in reaction sequences that describe the exchange.

**Table VII.** Some Pseudoscalar Mesons (Spin 0)

Meson	Quark content	Charge	Mass (MeV/c <sup>2</sup> )		
			Mass (MeV/c <sup>2</sup> )	Lifetime	Principal decays
$\pi^\pm$	$u\bar{d}, d\bar{u}$	+1, -1	139.569	$2.60 \times 10^{-8}$	$\mu \nu_\mu$
$\pi^0$	$(u\bar{u} - d\bar{d})/\sqrt{2}$	0	134.964	$8.7 \times 10^{-17}$	$\gamma \gamma$
$K^\pm$	$u\bar{s}, s\bar{u}$	+1, -1	493.67	$1.24 \times 10^{-8}$	$\mu \nu_\mu, \pi^\pm \pi^0, \pi^\pm \pi^\pm \pi^\pm$
$K^0, \bar{K}^0$	$d\bar{s}, s\bar{d}$	0	497.72	$0.892 \times 10^{-10}$	$\pi^+ \pi^-, \pi^0 \pi^0$
				$5.18 \times 10^{-8}$	$\pi e \nu_e, \pi \mu \nu_\mu, \pi \pi \pi$

The characteristics of pions, such as their charge, spin, and rest mass allows the deduction of equations for pion exchange between nucleons. Also of note is that the  $\pi^+$  and  $\pi^-$  are antiparticles to each other, while  $\pi^0$  is its own antiparticle. Pions also have the longest range of the mesons, and are able to propagate through many types of matter before they are ‘captured’ to take place in a strong interaction within the matter.

$$n_1 \rightarrow n_1 + \pi^0 \quad \pi^0 + n_2 \rightarrow n_2 \quad (30)$$

$$p_1 \rightarrow p_1 + \pi^0 \quad \pi^0 + p_2 \rightarrow p_2 \quad (31)$$

$$n_1 \rightarrow p_1 + \pi^- \quad \pi^- + p_2 \rightarrow n_2 \quad (32)$$

The capture reactions are known as stars.

With the particles of the GCR being limited to roughly 1 GeV/nucleon, the prevalence of heavier mesons (besides  $\pi$  or K) in an energetic reaction is dependent on higher incident energies than what would be encountered most often in the space environment, perhaps TeV or more, which generally makes them inaccessible on earth, other than at the most energetic accelerators.

## *ii. Stars*

Pions will pass through and interact with matter, whereby they are eventually stopped and captured by nuclei of the target atoms. There are many reactions which might then occur, such as the capture of  $\pi^-$  by  $^{16}\text{O}$  to yield  $^{16}\text{N}^*$ , and the location of  $\text{N}^*$  is called a star due to the pion capture event. Stars are inelastic pion reactions. The star term originated from the photographic emulsion technique, which showed particle tracks radiating outward from the site of capture. The possibilities of  $\pi^-$  capture may include<sup>7</sup>

$$\pi^- + {}^{16}\text{O} \rightarrow {}^{16}\text{N}^* \quad (33)$$

$$\begin{aligned} {}^{16}\text{N}^* &\rightarrow {}^{15}\text{N} + \text{n} \\ &\rightarrow {}^{14}\text{N} + 2\text{n} \\ &\rightarrow {}^{14}\text{C} + \text{p} + \text{n} \\ &\rightarrow {}^{12}\text{B} + \alpha \end{aligned} \quad (34)$$

Pi-mesons are charged particles, so they in fact cause ionization events along their entire pathlength within a material, until they are eventually captured to take place in a strong-force interaction. Heavy particles and nucleons produced by the star give a large dose in a relatively small volume. As shown in Eq. 34, the  $^{16}\text{N}^*$  might decay in any of four

possible ways, and lose mass by emitting energetic particles. There is the possibility of emitted neutron radiation, protons, and alpha particles. This is just the example of  $\pi^-$  capture to yield a star; there is also the possibility of  $\pi^+$  and  $\pi^0$  interacting to form stars, which would still result in the emission of energetic particles, though the charge of the emitted particles could be opposite for  $\pi^+$  in contrast to the case of  $\pi^-$  above. The capture of  $\pi^0$  is another process that has not been examined in this work, but surely will contribute to the transmutation of nuclear species within an irradiated target, and emission of harmful energy to the surroundings.

Some of the more basic aspects of nuclear structure have now been described for the reader, such as mass and binding energetics, the composition of nucleons, and the existence of mediators or exchange particles which interact with each other. This information can now be used, as the discussion now shifts to the interaction of photon and particle radiation with matter.

## **F. The Interaction of Radiation with Matter**

Physicists who study nuclei and particle beams are generally concerned with three kinds of radiation that may be incident on a target; these are the light charged particles (LCP), the heavy charged particles (HCP), and electromagnetic radiation. The light charged particles are electrons and positrons, with rest mass energy  $mc^2 < 1$  MeV, while the heavy charged particles are any with  $Z \geq 1$ , so  $mc^2 > 900$  MeV. The EM radiation are the x- and  $\gamma$ -ray photons, which are commonly several MeV in energy and above, with the upper limit for some galactic cosmic rays said to be  $10^{20}$  eV, as described in I.A.1. The emphasis in space radiation shielding is on the heavy charged particles, which can be as small as a single proton, or as large as a  $^{238}\text{U}$  nucleus. The energy deposition and ionization effects increase rapidly with increasing  $Z$ , and as massive particles pass through target materials, they interact with electrons and nuclei within the target material many phenomena because of the interaction with the electrons or nuclei of the target material. The list of relevant cross sections includes but is not limited to Coulomb scattering, fragmentation (charge-changing) of primary or target nucleus, Compton scattering, inelastic scattering with electrons, production of nucleons or electrons, and production of electromagnetic radiation.

## 1. Electromagnetic Radiation – Gamma Rays

The range of energetic EM radiation in biological systems is determined using the knowledge that this radiation interacts with matter to produce three main types of phenomena: the photoelectric effect (photoelectric absorption), scattering on free electrons (Compton scattering), and electron-positron pair production. Electromagnetic radiation exhibits exponential absorption, and the energy is removed from the beam and degraded. This takes place according to

$$I = I_0 e^{-\mu x} \quad (35)$$

where  $I$  is the intensity of the incident radiation,  $\mu$  is the specific absorption coefficient, and  $dx$  is the thickness traveled. The quantity  $\mu$  may be called the mass attenuation coefficient for a specific  $\gamma$ -ray. The source of the attenuation in the beam is the combination of the three effects, each of which are more or less pronounced depending on the incident gamma energy.

### *i. Photoelectric Effect*

The photoelectric effect can be thought of as the absorption of a gamma ray by a bound electron, which then leaves the atomic state it was in. The process leads to the production of secondary radiation, primarily the ejection of photoelectrons from atoms, and also *bremstrahlung* radiation. The incident  $\gamma$  energy ( $h\nu$ ) is enough to remove an electron from its normal orbital position, which is then liberated from the atom at a kinetic energy (KE) that is equal to the difference between the incident  $h\nu$  and the binding energy (BE) of the electron in that shell. The most tightly bound K-shell electrons are the major contributors to this effect, as shown in Figure 14, but the lower binding-energy electrons of the outer shells may be ejected by the similar Auger process.

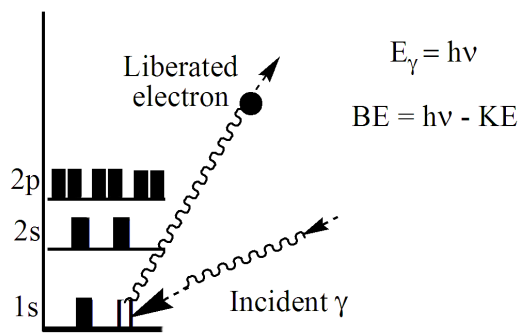


**Figure 14.** Schematic of K-shell photoelectron produced via a keV  $\gamma$  ray.

### ii. *Compton Scattering*

A  $\gamma$ -ray may interact with and impart some of its energy to an atomic electron. The process results in a different, lower-energy gamma ray which is scattered off at some angle, and the energy difference is transferred to the electron, which itself is then scattered at some other angle and left in an excited state. This process is known as Compton scattering, and is shown in Figure 15. The original photon has an energy of  $E_{\gamma}$ , the scattered photon is of energy  $E'_{\gamma}$ , and the electron acquires an energy equal to  $E_{\gamma} - E'_{\gamma}$ . The excited state of the electron ( $e'$ ) may then decay to its original state by emission of some quanta of electromagnetic radiation, or by some other relaxation process. With the presence of many electrons in ordinary matter, it is evident that there may be a number of Compton scattering events, which would then degrade the energy of the incident photon. The most energetic  $\gamma$ -rays are more likely to pass through most types of matter without interacting.

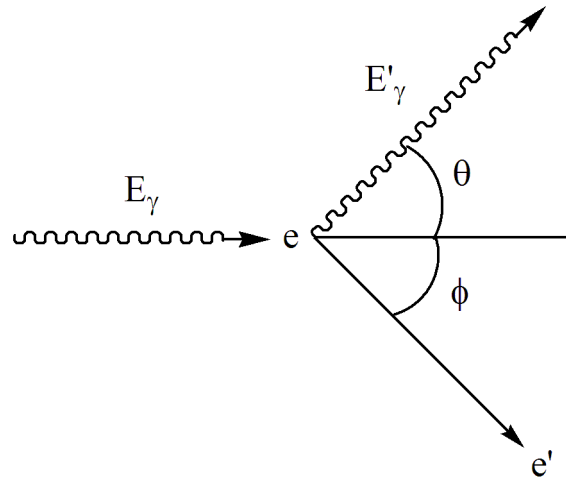


**Figure 15.** Schematic of Compton Scattering.

The scattered gamma ray energy  $E'$  is a function of the photon scattering angle  $\theta$ . From Figure 15, it is evident that the  $\gamma$ -photon is scattered off in some new direction, and with a lower energy than it had incidentally. The result is that a beam of gamma rays will broaden and lose energy with successive Compton scatterings as it passes through some amount of matter. The probability of a Compton scattering varies approximately as the atomic # of the scattering medium and decreases as the energy of the  $\gamma$ -photon increases. Compton scattering dominates at medium energies (from roughly 1 to 10 MeV)

### *iii. Pair Production*

A photon with greater than approximately 1 MeV of energy can cause the creation of an electron-hole pair. The mechanism by which this occurs is  $\gamma$ -ray annihilation, whereby an electron and a positron are instantaneously created. Every particle known to man has its own antiparticle. If the electron and positron antiparticles meet, they annihilate each other, and the result is the production of 2 gamma rays. The quantum energy of the gamma rays is equal to the sum of: 1) the mass energies of the two colliding particles, and 2) their kinetic energies. The rest mass energy for an electron is 0.511 MeV, so the threshold for electron-positron pair production is twice this number, or 1.02 MeV, with the threshold energy being given in Eq 36. For x- and  $\gamma$ -ray energies well

above 1 MeV incident, pair production becomes one of the most important interactions for radiation incident on normal matter.

$$E_{\text{threshold}} = 2m_0c^2 \quad (36)$$

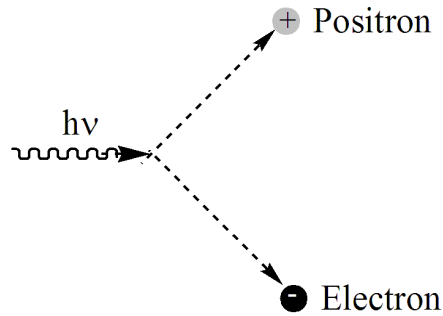


**Figure 16.** Schematic of  $\gamma$ -induced electron-positron pair production.

The three potential  $\gamma$ -ray interactions depend strongly on  $Z$  of the absorber, and the energy of the incident  $\gamma$ -ray. The trend is shown in Figure 17. For lower energy  $\gamma$ -photons ( $< 1$  MeV) photoelectric absorption dominates for nearly all  $Z$ . The lower-energy  $\gamma$ -rays are closer in magnitude to the energy of the K-shell electrons, thus are more readily absorbed, which excites the atoms and causes them to emit the excess energy as bremsstrahlung or photoelectrons. The low-energy  $\gamma$ -rays are not energetic enough to pass through a large number of atoms without interacting. The Compton effect is the primary mechanism of energy moderation for  $\gamma$ -rays at 1-10 MeV of incident energy. For  $\gamma$ -photons of moderate energy (10-100 MeV), the phenomenon of pair production is the dominant mechanism of energy attenuation.

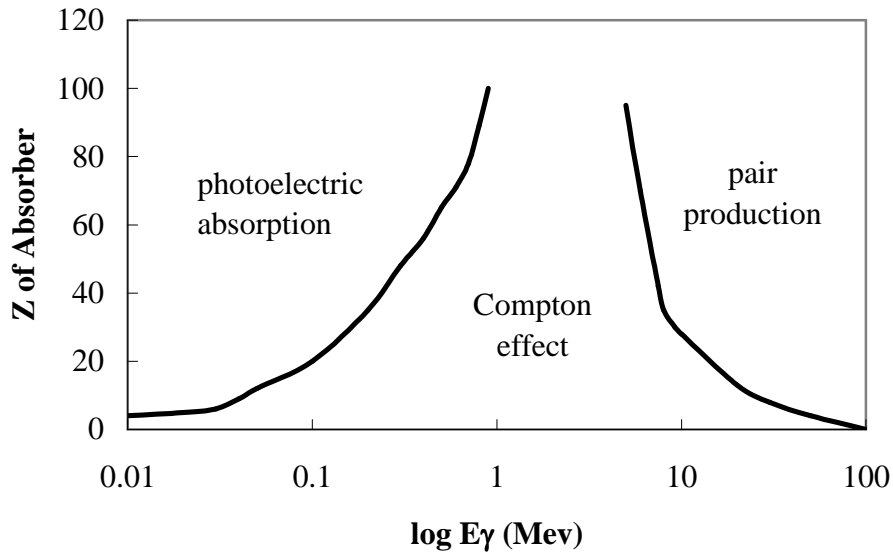


**Figure 17.** Effect of Z on  $\gamma$ -ray interactions.

## 2. Charged Particles

### *i. Coulomb Scattering*

Coulomb scattering (or Rutherford scattering) is simply the deflection of a charged particle's trajectory due to the repulsive force of the positively-charged nuclei. The incident primary comes in close proximity to a target nucleus and experiences the short-range electrostatic repulsive force, which causes it to emerge from the interaction at a different angle. The situation is shown in Figure 18. The straight line that is the distance of closest approach is known as the impact parameter ( $b$ ). Though the particle has been scattered off in some new direction, it can still be expected to contain a great deal of kinetic energy, so the intact primary is still able to participate in many interactions after a coulomb scattering event.

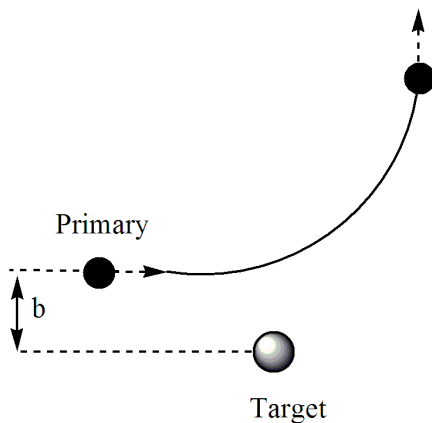


**Figure 18.** Rutherford (also Coulomb) scattering

*ii. Inelastic Collisions*

Charged particles interact as they travel into a target material, with the light charged particles losing their incident energy primarily through inelastic collisions with atomic electrons, but electrons and positrons may also radiate energy away by bremsstrahlung due to the various accelerations set up by electric fields within matter. Equations 37 through 42 presented below allow for the determination of the projectile's rate of energy loss per unit distance within the target material ( $-dE/dx$ ). The  $-dE/dx$  for a specific ion, energy, and target material is an important quantity, because  $dE/dx$  may then be converted to linear energy transfer (LET), LET may be converted into fluence, and the determined fluence (over some known time interval) then allows an estimate of the absorbed dose within the target. The energy loss per unit length is also termed the *stopping power* of the material. In many studies, the  $-dE/dx$  energy loss, LET, and (electronic) stopping power are analogous, so the three types must be specifically measured to distinguish between them. There is no distinction between the three quantities in this work, since the simulated data only allows an estimated magnitude for the energy loss for the moving particles in the materials of interest.

A monoenergetic beam of heavy charged particles will lose energy when it traverses through some amount of matter, and ultimately, all particles will be stopped after they cross some specific thickness of absorber—this is again dependent on the material and beam energy. The minimum amount of absorber material that stops a

particle is the *range* of the material for a specific particle at a specific incident energy. The magnitude of the range depends on the rate at which the charged particle loses energy in the inelastic collisions with electrons. Derived from quantum mechanical calculations of the collision process, the Bethe-Bloch energy loss is the process that determines the range of a particle in a material. Range is typically reported in terms of energy in MeV/ nucleon (MeV/u) plotted against the thickness of material traversed by the particle, but the use of *areal density* affords a more meaningful comparison among solids with varying volumetric densities. The areal density is simply the volumetric density ( $\text{g/cm}^3$ ) multiplied by the thickness, so  $(\text{g/cm}^3) \cdot (\text{cm of thickness}) = \text{g/cm}^2$  of range, as displayed in Figure 19 for four different nuclei in aluminum metal of density  $2.70 \text{ g/cm}^3$ . For materials and objects deployed in space, areal density is also used as the material property of choice instead of volumetric density. The estimated range data in this study is reported in terms of both areal densities ( $\text{g/cm}^2$ ) and linear thickness to afford a simplified visual picture of the penetration depth of the energetic ions.

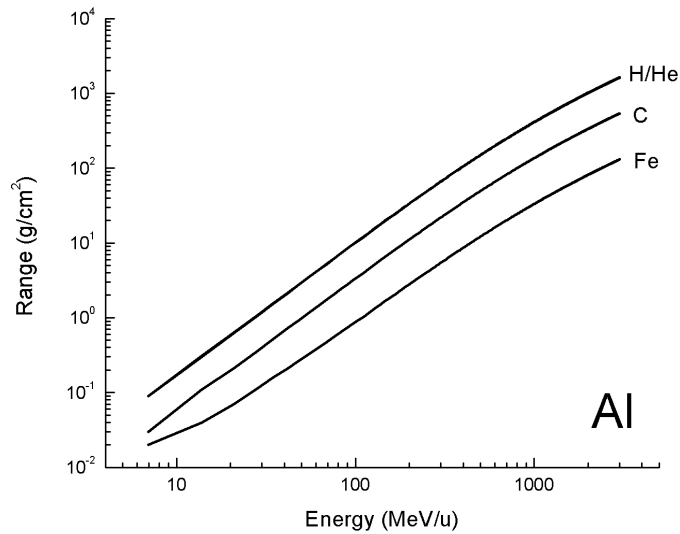


**Figure 19.** Range in  $\text{g/cm}^2$  Vs. Energy in MeV/u for  $^1\text{H}$  (protons),  $^4\text{He}$ ,  $^{12}\text{C}$ , and  $^{56}\text{Fe}$  in aluminum metal.

### *iii. HCP*

For heavy charged particles, the rate of energy loss per unit distance is computed using the Bethe-Bloch formula:

$$-\frac{dE}{dx} = \frac{4\pi r_e^2 m_e c^2 z^2}{\beta^2} NZ \left[ \ln \frac{2m_e^2 c^2 \gamma^2 \beta^2}{I} - \beta^2 \right] \quad (37)$$

where  $\beta = v/c$ ,  $v$  is the velocity of the incident particle,  $ze$  is the charge,  $N$  is the number density of target atoms,  $Z$  is the atomic number, and  $\gamma = (1-\beta^2)^{-1/2}$

$$\gamma = \frac{1}{\sqrt{1-\beta^2}} \quad (38)$$

and  $r_e$  is the classical electron radius, with  $e$  being the electronic charge

$$r_e = \frac{e^2}{m_e c^2} \quad (39)$$

$I$  is the average excitation and ionization potential of the absorber, which is an experimentally-determined quantity. The Bethe-Bloch equation breaks down at low energy, where the incident particles are at roughly the same “velocity” as the orbital electrons. The most common secondary radiation produced by heavy charged particles are energetic secondary electrons, called delta rays. The delta rays often have enough kinetic energy to create further ionization events, but the range of secondary delta rays is much smaller than for the original charged projectile.

### *iv. LCP*

The light charged particles are the electrons or positrons, and are treated in a similar fashion to the heavy charged particles, but the equation above must be modified. The light charged particles are closer in mass to the atomic electrons, so the energy loss occurs more quickly because a much larger fraction of electron energy can be lost in a single encounter. The modified Bethe-Bloch formula for light charged particles is

$$-\frac{dE}{dx} = \frac{2\pi r_e^2 m_e c^2}{\beta^2} NZ \left[ \ln \frac{m_e^2 c^2 \beta^2 T \gamma^2}{2I^2} - \ln 2 \left( \frac{2}{\gamma} - \frac{1}{\gamma^2} \right) + \left( \frac{1}{\gamma^2} \right) + \frac{1}{8} \left( 1 - \frac{1}{\gamma^2} \right)^2 \right] \quad (40)$$

in which all symbols have the same meaning as above.

The mean range may be calculated for a particle of a given energy ( $T_0$ ) by integrating the  $dE/dx$  formula:<sup>16</sup>

$$R(T_0) = R_0(T_{\min}) + \int_{T_{\min}}^{T_0} \left( \frac{dE}{dx} \right)^{-1} dE \quad (41)$$

where  $T_{\min}$  is the minimum energy at which the  $dE/dx$  formula is valid, and  $R_0(T_{\min})$  is an empirically determined constant to account for the low energy  $dE/dx$  behavior.<sup>16</sup> When integrating, the range is found to be proportional to  $T^2$ .

For both types of charged particles, the quantity  $dE/dx$  is a measure of the rate at which the incident radiation is losing energy relative to the distance it is traveling within the material. The negative sign indicates the loss of energy. The total  $dE/dx$  is generally taken as a good estimate of the magnitude of energy that the incident particle will lose to the target material, as well as an estimate of the thickness of material required in order to fully attenuate the incident energy of the radiation.

As the initially-energetic particle moves through the target material, the collisional energy loss will not remain at a constant value. The particle loses kinetic energy due to its effect on the surrounding electrons, while continuously causing ionization and excitation effects along its path. If the instantaneous  $dE/dx$  energy loss could be measured, it would be evident that the energy lost to the surroundings will increase for a projectile that is continuously slowing down. Visually, the increasing collisional energy loss would be manifested as a continuously thickening and darkening ionization track toward the end of the particle's path, as shown in Figure 20 for the protons and electron paths of section I.A. The result of the changing  $dE/dx$  behavior is a maximum in energy deposition right before the particle is completely stopped, which shows up as a peak in a plot of energy deposition (dose) against depth (distance). The peak of energy deposition for any charged particle is known as the Bragg peak, as shown in Figure 21.

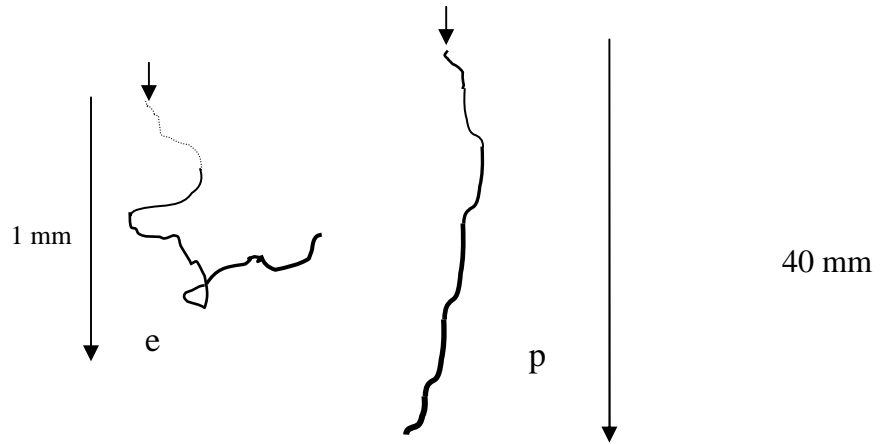


**Figure 20.** Representation of energy imparted over the path length for MeV charged particles and subsequent Bragg peak of energy deposition.

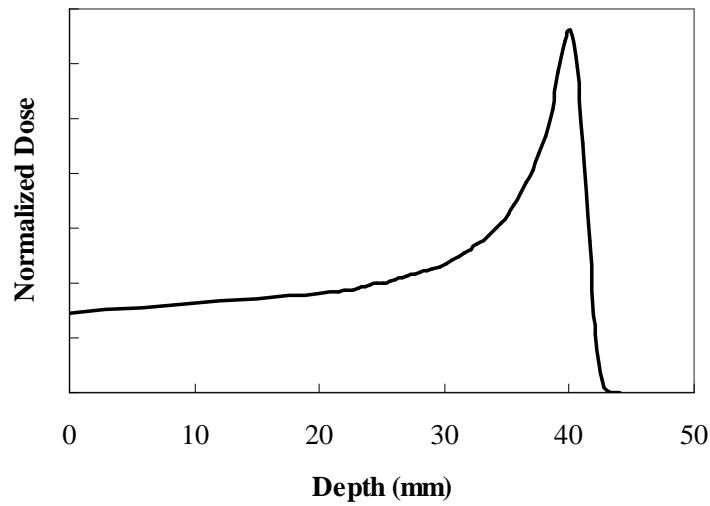


**Figure 21.** Energy deposition and Bragg Peak for 500 MeV protons in simulated biological tissue.

If the range of a particle (at a specific energy) is known for some material with known density, the range of this particle in another material may be estimated by invoking the Bragg-Kleeman rule:<sup>7,16</sup>

$$\frac{R_1}{R_0} \cong \frac{\rho_0 \sqrt{A_1}}{\rho_1 \sqrt{A_0}} \quad (41)$$

where  $R$  is the range,  $\rho$  is the mass density,  $A$  is the atomic weight, 0 stands for a known range or material, and 1 stands for the unknown range or material. Inelastic collisions are the primary loss mechanism for the majority of massive particles, but for lighter particles such as electrons which become intermittently scattered in electric fields, the emission of electromagnetic radiation causes significant energy loss for the incoming particles.

#### v. *Bremsstrahlung*

In addition to collision losses as for HCP, the light charged particles such as electrons and positrons will experience scattering within materials due to the internal electric fields of nuclei, and will thus lose energy via emitted electromagnetic radiation. The emitted radiation continuum is known as bremsstrahlung, which may be thought of classically as the acceleration of charged particles when they encounter an electric field. For small energies up to a few MeV, the bremsstrahlung process contributes very little to the total energy loss, but the probability of bremsstrahlung emission increases rapidly for incident particles at tens of MeV or greater, and in fact may be equal to the collisional energy loss at these energies. The total energy loss for the light charged particles is then the sum of collisional and radiative losses:

$$\left(\frac{dE}{dx}\right)_{\text{tot}} = \left(\frac{dE}{dx}\right)_{\text{rad}} + \left(\frac{dE}{dx}\right)_{\text{col}} \quad (42)$$

The emission probability is highly dependent on the particle mass as, so the cross section for radiative energy loss varies as the inverse of the particle mass squared:

$$\sigma \propto \left(\frac{e^2}{mc^2}\right)^2 \quad (43)$$

The occurring radiative loss is a balance of several competing factors, but can be expected to be less important than collisional losses for the heavier particles. More massive particles will experience less scattering in electric fields and less deviation from their original trajectory. As an example, a muon with mass of  $106 \text{ MeV}/c^2$  imparts roughly 40,000 times less radiative energy loss than an electron, which has a mass of

0.5011 MeV/c<sup>2</sup>.<sup>16</sup> Bremsstrahlung emission depends on the strength of the electric field felt by the incident LCP, so atomic electrons will screen the scattering (acceleration) effects. The cross section for radiative emission is also dependent on the impact parameter and Z of the target material. For LCP, Bremsstrahlung starts to dominate the energy loss at energies of 1 GeV or greater. The incident energy value where collision loss equals radiative loss is known as the critical energy (E<sub>c</sub>) and depends almost entirely on the material.

$$\left(\frac{dE}{dx}\right)_{\text{rad}} = \left(\frac{dE}{dx}\right)_{\text{col}} \quad \text{for } E = E_c \quad (42)$$

In general, a lower effective Z results in higher critical energies, with organic compounds featuring an average E<sub>c</sub> of around 100 MeV. Light metals correspondingly show a lower E<sub>c</sub>. Some critical energies are given in Leo:<sup>16</sup> Al has a value of 51.0 MeV, Fe has a value of 27.4 MeV, and Pb has a value of 9.51 MeV, while that for polystyrene is 109 MeV. It is evident that higher electron densities result in lowered values of the bremsstrahlung critical energy. The probability of bremsstrahlung emission is inversely proportional to the particle mass squared, so bremsstrahlung can generally be ignored for the heavy charged particles. For energies on the order of MeV, the contribution of bremsstrahlung is relatively small, but the probability of bremsstrahlung increases rapidly with increasing energy, and will eventually dominate the energy loss.

#### *vi. Linear Energy Transfer and Stopping Power*

To compare the effects of different types of radiation on biological tissue, the factor of interest is the linear energy transfer (LET) of the radiation, which is a measure of the energy deposited per unit distance over the path traveled. Bremsstrahlung may propagate radiation far away from the actual path of the incident projectiles, and if bremsstrahlung processes are neglected, the LET is the same as the linear stopping power dE/dx. Examples of high-LET radiation are the heavy ions and α particles. Such charged particles generally have short range in matter because they dissipate their energy quickly in collisions. The larger amount of energy deposition over short distances corresponds to

a higher value of the LET. Typical range values for MeV particles may be 0.1-1.0mm, and the LET may reach 100 keV/ $\mu\text{m}$ .<sup>7</sup> In contrast, some of the low-LET particles include electrons or photons, which have ranges on the order of cm, and LET on the order of perhaps 1 keV/ $\mu\text{m}$ . For heavy ion irradiation, the earth-based accelerators of BNL and Chiba Japan allow the choice of ion, the incident energy, and the approximate LET, as shown in Table VIII. It is evident that for a heavy projectile such as  $^{56}\text{Fe}$ , the highest incident energy (1000 MeV/ $\mu$ ) results in the lowest LET (150 keV/ $\mu\text{m}$ ), while the lowest incident energy (300 MeV/ $\mu$ ) results in the highest LET (240 keV/ $\mu\text{m}$ ).

The linear energy transfer (LET) is often analogous to the quantity  $-dE/dx$  described above. There are two types of LET that are estimated or measured by researchers, which are the track average LET and the dose average LET. Accurate estimates are difficult to obtain in both cases, as shown pictorially in Figure 22. A good estimate of the track average LET requires being able to follow an individual particle (or group of particles) throughout the target and measure the energy after it traverses some thickness of material.

**Table VIII.** List of Heavy Particles for Use at the RHIC of NSRL/BNL.

<b>Ion</b>	<b>Z</b>	<b>Energy (MeV/u)</b>	<b>LET (keV/<math>\mu\text{m}</math>) (approximate)</b>
Iron	26	1000	150
Iron	26	750	160
Carbon	6	290	13
Iron	26	600	180
Protons	1	1000	0.24
Silicon	14	1000	45
Oxygen	8	600	17
Iron	26	300	240
Protons	1	2500	0.24

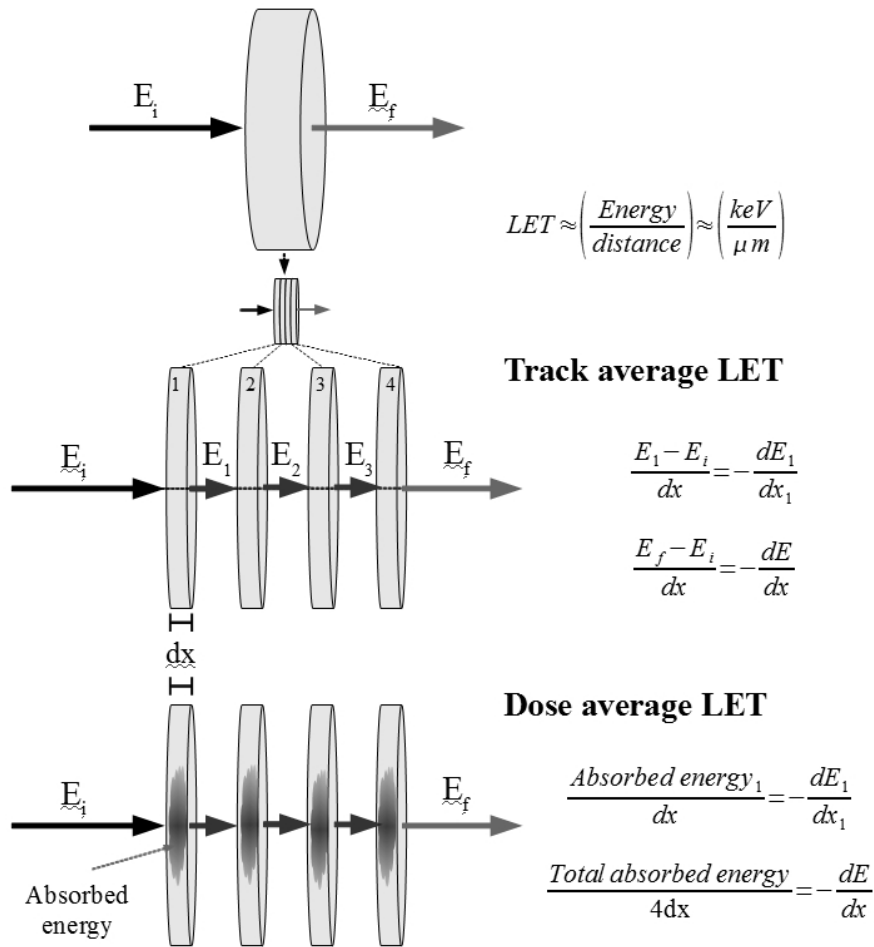


**Figure 22.** Determination of track average and dose average LET.

In practice, measurement of LET is achieved using position sensitive detectors across the area in the plane perpendicular to the beam, and measuring the energy along a small volume of acceptance around the original line of the particle's trajectory. The most common convention is the use of a  $3^\circ$  solid angle around a specifically-located detector for the acceptance of the moving particle. The dose average LET is obtained by determining the amount of energy the projectile imparts through the volume of the surrounding target material that it has passed through. This may be determined by

finding a quantity such as the absorbed dose, or magnitude of ionization that is conveyed through each “slice” of material, as shown in Fig. 22.

For the range of incident energies most relevant to GCR studies (spanning from a few MeV to 1 GeV), the terms describing energy loss by projectiles Bethe-Bloch energy loss and both types of LET are roughly equivalent to another term for projectile energy loss, the *stopping power*. Stopping powers would be reported in terms of (Energy loss/unit length), just as LET and  $-dE/dx$  for some specific particle at some specific energy and within some specific material. The total stopping power is composed of contributions from two mechanisms: the electronic stopping power, and the nuclear stopping power. The electronic stopping power is due to the inelastic collisions taking place via Bethe-Bloch energy loss, and the nuclear stopping power refers to the deceleration or scattering by the Coulomb/Rutherford mechanism.

The charged particles behave in a manner that is quite different in comparison to uncharged particle radiation. Neutrons, being relatively massive uncharged particles, behave in a manner entirely different from the LCP and HCP. Neutrons are able to transfer significant momentum to target nuclei kinematically, and when slowed down, they may be captured within a nucleus to yield new isotopes, which will affect their immediate surroundings via a number of different reaction or decay possibilities.

### **3. Neutrons**

Depending on their incident energy and the reaction cross sections, neutron interactions with nuclei can produce several types of secondary particle radiation, including protons, alphas, and heavier ions. As a proton travels through its target material, it continuously interacts with the surrounding electrons, so the Bethe-Bloch energy loss equations describe the behavior quite well. For 100 MeV protons stopping in tissue, nuclear reactions occur on the order of only a few percent.<sup>35</sup> Since neutrons contain no electric charge, they mostly encounter empty space as they travel, with small concentrated areas of nuclear matter dispersed throughout with which they might interact. There are thus only two possibilities for the neutrons: they can either react with a nucleus, or pass through without any interaction.<sup>35</sup> The behavior of neutrons as secondary radiation may be inferred from studies of how artificial neutron beams interact

with matter, for which the absorption and moderation of neutrons is dictated by nuclear reactions as they travel within materials. The attenuation of the initial neutron energy is caused by elastic and inelastic collisions with atoms. Neutrons of various energies can be produced by specific nuclear reactions, but since neutrons are uncharged and can not be accelerated, energetic neutrons must first be produced and then slowed down to obtain lower energies if required for experiments. The commonly-utilized reactions to produce neutrons generally have Q on the order of a few MeV, but there are in fact five energy designations for neutrons that might interact with a material, where E is the incident energy:

Ultra-cold	$E \approx 10^{-6} \text{ eV}$
Cold	$E \approx 10^{-3} \text{ eV}$
Thermal	$E \approx 0.025 \text{ eV}$
Epithermal	$E \approx 1 \text{ eV}$
Slow	$E \approx 1 \text{ keV}$
Fast	$E \approx 100 \text{ keV} - 10 \text{ MeV}$

When a beam of neutrons passes through bulk matter, the intensity will be degraded due to nuclear reactions which serve to remove neutrons from the beam. The neutrons will slow down and be moderated due to elastic and inelastic scattering processes with atoms, so as they are slowed, neutrons may be more likely to interact with a nucleus in the material. For fast neutrons, there are many possible reactions to cause their disappearance from the beam, such as  $(n, p)$ ,  $(n, \alpha)$ , and  $(n, 2n)$ . Slow or thermal neutrons may disappear by capture, which would proceed in the form of the  $(n, \gamma)$  reaction.

The degradation in energy of a neutron beam can reasonably be described in the form of an exponential decay, which is similar to the description of intensity attenuation in gamma rays. After traveling some distance x, the intensity of neutrons is given by

$$I(x) = I_0 e^{-N\sigma x} \quad (x)$$

Where  $I_0$  is the incident intensity, N is the number of nuclei per unit volume, and  $\sigma$  is the specific reaction cross section.

Neutrons represent a different case in comparison to the electromagnetic and particle radiation described in 6.A and 6.B, because the neutrons themselves do not ionize atoms directly as do gamma and charged particle radiation. The neutrons first have to cause the production of secondary radiation by being absorbed, so the concept of KERMA is used, where KERMA refers to **k**inetic **e**nergy **r**elaxed in **m**atter, and is defined as:<sup>35</sup>

$$K = \frac{dE_{TR}}{dm} \quad (x2)$$

where  $dE_{TR}$  is the expectation value of the sum of *all* the kinetic energies of all the charged particles liberated by the uncharged neutrons in some mass  $dm$  of target material. Kerma and dose are measured in the same units (Gy, for example), except there is an important distinction: kerma describes *released* energy of secondaries due to neutrons, while dose refers to the *absorbed* energy.

Specific pathways for neutron-induced reactions are available depending on the incident neutron energy. The interaction probabilities are determined by the reaction  $Q$  values. For exothermic reactions ( $Q > 0$ ), the reaction or decay can occur at rest within the lab frame, so requires zero incident energy. The  $Q$  value for the elastic channel of interactions is taken to be zero. In endothermic reactions ( $Q < 0$ ), there is an energy threshold below which the reaction can not occur. Examples of neutron-induced reactions with positive  $Q$  are  $^{10}\text{B}(n,\alpha)$ , and  $^{14}\text{N}(n,p)$ , for which the  $Q$  values are 2.790 MeV, 0.626 MeV respectively. The fission of  $^{235}\text{U}$  may demonstrate  $Q$  values of up to 200 MeV depending on the reaction channel.<sup>35</sup> For  $+Q$  reactions, the general  $\sigma$  behavior shows  $1/v$  dependence ( $v$  = neutron velocity) so  $\sigma$  generally decreases as  $v$  increases. With increasing energy, more reaction channels are possible, such as  $^{12}\text{C}(n,n')$ , for which the threshold is 4.44 MeV, and this value is slightly above the first excited state of  $^{12}\text{C}$ , at 4.4391 MeV.<sup>35</sup>

For fast neutrons entering matter, the loss of energy proceeds by both elastic and inelastic scattering until the neutrons reach thermal equilibrium with the surrounding atoms.<sup>16</sup> The energy loss is termed *moderation*, and if the neutron slows down enough and is thermalized, it may participate in a nuclear reaction. There is also the possibility

of resonances, which allow neutron capture before attaining thermal energy. In general, the moderation cross sections show a  $v^{-1}$  dependence so that most neutrons survive down to thermal energies, after which they are more easily captured.

For MeV neutrons, the moderation process may be treated non-relativistically by conservation laws, to find an approximate number of collisions that results in a certain degree of neutron energy attenuation.<sup>7,16</sup> The number of collisions ( $n$ ) to reach a certain level of energy reduction depends primarily on the mass number of the target nucleus, and is given by:<sup>7,16</sup>

$$n = \frac{1}{\xi} \ln \frac{E_o}{E'} \quad (42)$$

where  $E_o$  is the original neutron energy,  $E'$  is the energy after the collision, and the quantity  $\xi$  is given by:<sup>16</sup>

$$\xi = 1 + \frac{(A-1)^2}{2A} \ln \left[ \frac{A-1}{A+1} \right] \quad (43)$$

where  $A$  is the mass number. To see examples, the energy reduction term might be considered for an incident fast neutron at  $E_o = 10$  MeV which is moderated to a value of  $E' = 0.025$  eV. For normal hydrogen,  $\xi = 1$ , so  $n$  is roughly equal to 18. For  $^{12}\text{C}$ ,  $\xi = 0.425$ , so this same level of neutron moderation is achieved after around 110 collisions. Equations 42 and 43 yield a decent approximation for neutrons up to a few tens of MeV, which are likely to be a large component in medium-energy GCR-induced nuclear fragmentation reactions. Neutron moderation data for some differently-sized nuclei are given in Table IX. Because of their ultimate nature as hadrons (or baryons), ultra-fast neutrons of hundreds of MeV, several GeV, and above have much more complicated and exotic particle effects which are beyond the scope of the present discussion.

**Table IX.** Neutron Moderation Properties for Several Nuclei.<sup>7</sup>

Nucleus	$\xi$	N for thermalization
<sup>1</sup> H	1.00	18
<sup>2</sup> H	0.725	25
<sup>4</sup> He	0.425	43
<sup>12</sup> C	0.158	110
<sup>238</sup> U	0.0084	2200

The cross-sections for these capture reactions are the most important factor in selecting neutron-moderating materials, but many times the cross-sections feature resonances where  $\sigma$  is very large, such as <sup>235</sup>U, which has a very large cross-section for the capture of thermal neutrons, and subsequently becomes fissionable. Except for resonances, the cross sections decrease with increasing velocity in the form of  $v^{-1}$ , so after being slowed by scattering, the nuclear absorption of a neutron becomes more likely. A neutron that was incident at 1 MeV might be scattered so many times that its energy is reduced to the thermal regime, on the order of eV. A neutron of just a few eV has a high probability of resonant or non-resonant absorption by many nuclei. A captured neutron may lead to a stable nucleus in an excited state, such as the example of



for which <sup>7</sup>Li is left in an excited state (denoted as \*) with an excess energy of 0.48 MeV.

There are three primary contributions to the absorbed dose in biological tissues due to incident neutrons-induced nuclear reactions. The human body consists of about 95% H, C, and O, so the  $\sigma$  data for n-interaction with these specific nuclei is most important for the determination of absorbed dose in tissue. Other relevant nuclei are Ca, N, and O. Roughly 50% of the dose due to incident neutrons (at several tens of MeV) is derived from proton recoils, or elastic scattering on hydrogen. Around 35-40% comes from n-induced production of light ions such as p, <sup>2</sup>H, <sup>3</sup>H, <sup>3</sup>He, and  $\alpha$  particles. The smallest contribution is from nuclear recoils due to elastic neutron scattering, which constitutes 10-15% of the occurring reactions.<sup>35</sup>

#### 4. Radiation Quantities and Dosimetry

The study of radiation protection and dosimetry makes use of several quantities primarily derived from the charge induced in target materials by ionizing radiation, and the subsequent energy that is deposited in the material by the projectile. Radiation researchers are concerned with five quantities, which are the charge (Q), activity (A), exposure (X), dose (D) and quality factor or weighting factor (QF or  $W_R$ ). The five are summarized in Table X. Charge may be thought of as a property of an object that enables it to interact with an electric field, but the total magnitude of charge developed in a sample indicates the degree of ionization induced by incoming radiation. For the passage of X-ray and  $\gamma$ -ray photons through media, the photons interact many times through Compton scattering, the photoelectric effect, and pair production. The free electrons created may be of high enough energy to further interact and produce ionization and additional electrons. From the extent of ionization in a material, the exposure (X) is found, which is equal to the total electric charge (Q) on the ions produced in some mass of air (m).

$$X=Q/m \quad (47)$$

which is given in Coulomb/kg in the SI system. Charge may be specified in terms coulombs, or the traditional unit, known as the electrostatic unit (esu). The charge on an electron (e) is

$$e = 1.6 \times 10^{-19} \text{ C} = 4.80 \times 10^{-10} \text{ esu}$$

so  $1 \text{ C} = 3.00 \times 10^9 \text{ esu}$ . Also of interest are the conversions between units of energy (eV, joules, ergs) where  $1 \text{ joule (J)} = 6.24 \times 10^{18} \text{ eV}$ , and  $1 \text{ J} = 1 \times 10^7 \text{ ergs}$ . This gives  $1 \text{ eV} = 1.602 \times 10^{-12} \text{ erg}$ .

The activity of a sample is the number of decays per second. The original unit for activity, the Curie (Ci), refers to the rate of disintegration occurring in one gram of radium,  $^{226}\text{Ra}$ , which is an  $\alpha$  emitter. One curie is equal to  $3.7 \times 10^{10} \text{ decays/s}$ . The SI unit for activity is the Becquerel (Bq), which is equal to 1 decay/s. This gives

$$1 \text{ Bq} = 2.7 \times 10^{-11} \text{ Ci}$$

Exposure (X) is a measure of the magnitude of ionization in air. The total magnitude of charge developed is taken to be related to the number of ion pairs generated per unit of material, so the SI unit would be charge/mass or C/kg. It takes an energy of roughly 34 eV to create an ion (an electron-positron pair) in normal air at standard atmospheric pressure and 0° C. The roentgen unit is the magnitude of ionization (in esu) that would be caused in a cm<sup>3</sup> of air under standard conditions (0° C and 1 atm or 760 mm Hg atmospheric pressure). Familiarity with the roentgen unit is useful, though its use is now being discouraged in favor of the more standard C/kg of the SI system. One cm<sup>3</sup> of air weighs 0.001293 g under standard conditions, so

$$1 \text{ roentgen (R)} = \frac{1 \text{ esu}}{0.001293 \text{ g air}} = \frac{773 \text{ esu}}{\text{g of air}}$$

$$\frac{773 \text{ esu}}{\text{g of air}} \times \frac{1.6 \times 10^{-12} \text{ C}}{\text{esu}} \times \frac{1000 \text{ g}}{1 \text{ kg}} = \frac{\mathbf{2.58 \times 10^{-4} \text{ C}}}{\mathbf{kg}}$$

We may now determine what effect an *exposure* of 1 R has on a kg of air

$$1 \text{ R} = \left( \frac{2.08 \times 10^9 \text{ \#}}{\text{cm}^3} \right) \left( \frac{34 \text{ eV}}{\text{ion}} \right) = \frac{\mathbf{7.08 \times 10^{10} \text{ eV}}}{\mathbf{\text{cm}^3 \text{ of air}}}$$

which results in approximately

$$\frac{1.61 \times 10^{15} \text{ \# ions}}{\text{kg of air}} \times \frac{1.293 \times 10^{-6} \text{ kg}}{\text{cm}^3 \text{ of air}} = \frac{\mathbf{2.08 \times 10^9 \text{ \# ions}}}{\mathbf{\text{cm}^3}}$$

and 1 R represents an energy deposition of

$$1 \text{ R} = \left( \frac{2.08 \times 10^9 \text{ \#}}{\text{cm}^3} \right) \left( \frac{34 \text{ eV}}{\text{ion}} \right) = \frac{\mathbf{7.08 \times 10^{10} \text{ eV}}}{\mathbf{\text{cm}^3 \text{ of air}}}$$

So an exposure of 1 roentgen results in an energy absorption of 7.08 x 10<sup>10</sup> eV per cm<sup>3</sup> of air. In air, one R is therefore equivalent to an energy absorption of 0.113 ergs per cm<sup>3</sup>, or 88 erg per g.

In general, the extent of ionization due to high energy radiation x- and  $\gamma$ -radiation will scale approximately linearly, so that  $1 \times 10^9$  eV will yield roughly

$$\frac{1 \times 10^9 \text{ eV}}{34 \text{ eV/ion}} = 2.94 \times 10^7 \text{ ions}$$

which is almost negligible compared to the typical number of constituents per  $\text{cm}^3$  of common solid materials (generally on the order of  $10^{22}$  for most solids).

Materials other than air exposed to ionizing radiation differ in their rate of energy absorption because of differences in density and other factors. The standard for defining the energy absorption by ionization in different materials is the absorbed dose (D) of the material. The dose is the quantity used to specify energy absorption in the target, which is reported as some quantity of energy per unit mass of material. The commonly used unit is the rad (Radiation Absorbed Dose) which is equal to an energy absorption of 100 ergs/g of material. The SI unit for absorbed dose is the Gray (Gy) which is absorption of 1 J/kg of material. In terms of rads,  $1 \text{ R} = 0.88 \text{ rad in air}$ , and  $1 \text{ Gy} = 100 \text{ rad}$ .

The quality factor of the radiation indicates its relative biological effectiveness. The QF is an integer number that describes the differences in energy deposition per path length for different types of particulate or electromagnetic radiation. In general, QF increases with the increasing mass of the incident particle. The QF is analogous to what is commonly termed the *weighting factor* of the radiation, as defined by the recommendations of the International Commission on Radiation Protection (ICRP).<sup>36</sup> The Sievert (Sv) is the quantity for description of the biological effectiveness of incident radiation, and is equal to the absorbed dose multiplied by the quality factor of the radiation.

The effect of different kinds of radiation is the primary consideration in the determination of standards for radiation protection of people. Some radiation deposit their energy over a very long path, so that relatively little is deposited over any small interval, perhaps  $10 \mu\text{m}$ , or the size of a human cell.  $\beta$ - and  $\gamma$ - rays are examples of this type. Other radiation such as  $\alpha$  particles or other HZE lose their energy more rapidly and deposit most of their energy over a very short path length. In comparison, the probability of cell damage from 1 rad of  $\alpha$ -radiation is much larger than the probability from 1 rad of

$\gamma$ -radiation, so to quantify the differences, the relative biological effectiveness (RBE) is used. RBE is defined as the ratio of the dose of a certain radiation to the dose of x-rays that produces the same biological effect.

**Table X.** Radiation Quantities of Interest

Quantity	Measure of	Traditional Unit	SI Unit
Charge (q)	Number of liberated electrons	Electrostatic unit (esu)	Coulomb
Activity (A)	Decay rate	Curie (Ci): $3.7 \times 10^{10}$ decays/s	Becquerel (Bq): 1 decay/s
Exposure (X)	Ionization in air	Roentgen (r): Exposure yielding 1 esu charge in 1 cm <sup>3</sup> air at 0° C and 760 mm Hg pressure	$\frac{\text{Coulomb}}{\text{kg}}$
Absorbed Dose (D)	Energy Absorption	Rad (r): 100 erg/g of material	Gray (Gy): 1 J/kg
Quality Factor (QF)	Effect of radiation in comparison to gamma rays at same incident energy	Energy / Unit path length	unitless
BE = D·QF	Biological effectiveness	Sievert (Sv)	(J/kg)*QF

Values of RBE range from 1 for gamma rays and beta electrons, to about 20 for  $\alpha$  particles and heavy nuclei. The effect of  $\gamma$  and  $\beta$  radiation is thus nearly the same as the effects of x-ray irradiation, while the higher QF particles impart significantly higher dose than any electromagnetic irradiation sources. The QF for neutrons is quite variable as shown in Table XI, ranging from 5 to 20, but even the thermal and low-energy neutrons produced in fragmentation present a troublesome scenario in radiation protection.

RBE is a difficult quantity to measure, so it is customary to work instead with what is known as the quality factor (QF) or weighting factor ( $W_R$ ) of the radiation, which have been calculated for a given type and energy of radiation according to the energy deposition per unit path length. For radiation that shows relatively little energy deposition per unit path length ( $\beta$ ,  $\gamma$ ), QF is approximately equal to 1. Radiation that deposits more energy per unit length ( $\alpha$ , HZE) has QF approaching 20

**Table XI.** Quality Factors (Weighting Factors) for Photon and Particle Radiation.<sup>36</sup>

<b>Radiation</b>	<b>Weighting Factor (or Quality Factor) [QF / W<sub>R</sub>]</b>
<i>Photons</i>	1
<i>Electrons and muons</i>	1
<i>Protons with E &gt; 2 MeV (other than recoil protons)</i>	2
<i>α particles, fission fragments, heavy nuclei</i>	20
<i>π mesons</i>	1-5
<i>Neutrons</i>	
< 10 keV	5
10 keV < E < 100 keV	10
100 keV < E < 2 MeV	20
2 MeV < E < 20 MeV	10
E > 20 MeV	5

The energetic radiation discussed above has important consequences for biological systems and tissues, including but not limited to the disruption and fragmentation of DNA molecules, ionization of tissues, and severe neurological effects in more complicated organisms. The effects of energetic proton irradiation are generally not deemed to be lethal, but exposure to energetic heavy ions causes severe deficits in neurochemistry, learning behaviors, and memory.<sup>19</sup>

The preceding discussion has focused on acquainting the reader with sufficient background information to realize that the shielding of space travelers is an extremely-challenging task. Only a few of the possible nuclear interactions have truly been considered within the following simulated irradiation data. The focus here is on three primary concepts: 1) The generation and emission of energetic gamma and neutron radiation from targets hit with MeV incident energy, 2) emitted radiation due to the more energetic GeV incident radiation, and 3) the state that the targets are left in after irradiation: the relative amounts of radioactive nuclei per unit volume, their identities, and the mechanisms of decay. The irradiation simulation and property data of the composites is considered relative to pure LDPE, which is currently the best candidate for this type of shielding material.

## II. EXPERIMENTAL PROCEDURE

Irradiation experiments were performed via simulation of materials and radiation interactions within the physics framework of two different Monte Carlo particle-transport codes. The two programs were the MCNPX transport code used by Z. Shayer,<sup>37</sup> and FLUKA code,<sup>17,18</sup> which was used by the author. The MCNPX software has fewer available options and is less familiar to the author, so more information on FLUKA is included here. The MCNPX code offers slightly more accurate cross-sectional data at low and medium incident energies (below 1 GeV/nucleon), while FLUKA is typically more accurate in the high-energy regime ( $\geq 1$  GeV/nucleon). A third software package, LISE,<sup>38</sup> was used to estimate the mean ranges of protons and some nuclei in some elemental targets and also in low-density polyethylene. The FLUKA software is used by NASA, CERN, and other researchers, and has many applications, including: simulated high energy physics experiments, shielding design, detector and telescope design, cosmic ray studies, dosimetry, and medical physics or radiobiology. The FLUKA software is for UNIX/LINUX platforms, and is available for free download at [www.fluka.org](http://www.fluka.org).<sup>17,18</sup> Many of the elements and materials of interest may be modeled in such transport codes, including the LDPE and glass of interest here. FLUKA also differentiates between isotopes and includes the different reaction cross-sections for most nuclei, which allows the construction of isotopically-enriched target materials in the simulation. However, isotope enrichment was not considered in this work, because the bulk composite materials are meant to be prepared without difficulty and as inexpensively as possible.

### A. Solar Protons in MCNPX

The fabricated composite materials were slightly different than what was originally intended, and featured LDPE which contained two types of glass particles. In  $\text{Li}_2\text{O}-\text{Al}_2\text{O}_3-\text{B}_2\text{O}_3$  glasses it is possible to achieve a range of viscosity-temperature behavior by varying the  $\text{Li}_2\text{O}/\text{Al}_2\text{O}_3$  ratio, but it was not possible to form significant yields of lithium alumino borate HGM. The focus was then shifted to using commercial silicate HGM for lightweighting, along with solid glass microspheres (SGM) of  $20\text{Li}_2\text{O}-$

10Al<sub>2</sub>O<sub>3</sub>-70B<sub>2</sub>O<sub>3</sub> (mole %) to test the possibility of neutron capture in the simulated irradiation. This glass was chosen because it exhibits good chemical durability and a relatively-low linear coefficient of thermal expansion (CTE) of  $\leq 7 \times 10^{-6} \text{ K}^{-1}$  up to 110° C, which is the LDPE processing temperature. For secondary neutron (n) and gamma ( $\gamma$ ) radiation, there were six pieces of data recorded: 1) n generated per incident primary, 2)  $\gamma$  generated per incident primary, 3) n transmitted per incident primary, 4)  $\gamma$  transmitted per incident primary, 4) the transmitted  $\gamma$  spectrum, and 6) the transmitted n spectrum. All measurements were made relative to 100% pure LDPE without any glass particle additions, and plotted against increasing SGM content. The total  $\gamma$  and n fluence resulting from the  $10^6$  incident proton events has been averaged over the number of events to yield an estimation of the quantitative effect that each proton has on its target. The data is given as an estimated number of secondary photons or particles per incident primary.

Proton irradiation simulation was also performed on a binary 33Li<sub>2</sub>O-67B<sub>2</sub>O<sub>3</sub> (mole %) glass to afford a comparison of the difference in n and  $\gamma$  transmission between the two glass compositions. To experimentally determine some physical properties (mass density, molar volume, and number of ions per unit volume or unit mass) for the two simulated glass compositions and the composites, 20Li<sub>2</sub>O-10Al<sub>2</sub>O<sub>3</sub>-70B<sub>2</sub>O<sub>3</sub> and 33Li<sub>2</sub>O-67B<sub>2</sub>O<sub>3</sub> were made in the laboratory by traditional melting of high purity Li<sub>2</sub>CO<sub>3</sub>, Al<sub>2</sub>O<sub>3</sub>, and H<sub>3</sub>BO<sub>3</sub>. Batches were melted in a 90Pt-10Rh at 1000° C for exactly 1 hour, after which the bottom of the crucible was quenched in room temperature water at 22° C. The crucible containing the sample was then set on a refractory brick and allowed to cool to room temperature, after which the glasses were annealed at their respective glass transition temperatures for ½ hour. Density measurements were obtained by the Archimedes method using kerosene as the immersion fluid. Property data is shown in Table XII.

**Table XII.** Property Data for Fabricated SGM and Commercial HGM Glass. Only the approximate composition of the HGM glass is given, and the mass density used for the calculation is that of pure SiO<sub>2</sub> glass (2.20 g/cm<sup>3</sup>).

Glass Composition	FW (g/mol)	$\rho$ (g/cm <sup>3</sup> )	$\frac{\rho * N_A}{FW}$ (#x10 <sup>22</sup> /cm <sup>3</sup> )	(x10 <sup>22</sup> )/cm <sup>3</sup>			
				# Li	# B	# Al	# O
<b>SGM glass</b>							
20Li <sub>2</sub> O-10Al <sub>2</sub> O <sub>3</sub> -70B <sub>2</sub> O <sub>3</sub>	64.906	2.135 ± 0.001	1.98	0.79	2.77	0.40	5.15
33Li <sub>2</sub> O-67B <sub>2</sub> O <sub>3</sub>	56.506	2.263 ± 0.002	2.41	1.59	3.23	-----	5.64
				<b>#B</b>	<b>#P</b>	<b># Si</b>	<b># O</b>
<b>HGM glass (approximate)</b>							
*96B <sub>2</sub> O <sub>3</sub> -3B <sub>2</sub> O <sub>3</sub> -1P <sub>2</sub> O <sub>5</sub>	61.19	*2.20 ± 0.002	2.16	1.30	4.32 x10 <sup>-2</sup>	2.07	4.45

The organization of simulated composite samples is shown in Table XIII and Table XIV. All composites were 90% LDPE by volume, with the remaining 10% consisting of a mix of the solid and hollow glass spheres. The quantity of HGM was varied from 5-10 volume %, and the quantity of SGM was varied from 0-5%. The different composites are denoted as Xs where X is the volume percent of solid glass spheres, so examples would be as follows: 0s consists of 90% LDPE and has only 10 vol% HGM, while 5s has 90% LDPE, 5 vol% HGM, and 5 vol% SGM.

**Table XIII.** Composition of Simulated Composite Target Materials

	Vol.		Vol.		Vol.					Mass of	Mass of
Composite Designation	Fn.	P (LDPE)	Fn.		Fn.	$\rho$ (SGM)	$\rho_c$ (theo)	$\rho_c$ (actual)	MASS	HGM (g)	SGM (g)
	LDPE	$g/cm^3$	HGM	$\rho$ (HGM)	SGM	$g/cm^3$	$g/cm^3$	$g/cm^3$	LDPE (g)		
0s	0.90	0.9245	0.10	0.20	0	2.135	0.852	0.8520	41.603	1.0	0
1s	0.90	0.9245	0.09	0.20	0.01	2.135	0.871	0.8714	41.603	0.9	1.068
2s	0.90	0.9245	0.08	0.20	0.02	2.135	0.891	0.8907	41.603	0.8	2.135
3s	0.90	0.9245	0.07	0.20	0.03	2.135	0.910	0.9101	41.603	0.7	3.203
4s	0.90	0.9245	0.06	0.20	0.04	2.135	0.929	0.9294	41.603	0.6	4.270
5s	0.90	0.9245	0.05	0.20	0.05	2.135	0.949	0.9488	41.603	0.5	5.338

**Table XIV.** Carbon, Hydrogen, and Ion Content of Composite Samples

<b>Material</b>	<b>Totals from LDPE (x10<sup>22</sup>)</b>		<b>Totals From SGM Glass (x10<sup>22</sup>)</b>				<b>Totals From HGM Glass (x10<sup>22</sup>)</b>			
	<b># H</b>	<b># C</b>	<b># Li</b>	<b># Al</b>	<b># B</b>	<b># O</b>	<b># B</b>	<b># P</b>	<b># Si</b>	<b># O</b>
LDPE	400.50	200.25	0	0	0	0	0	0	0	0
0s	400.50	200.25	0	0	0	0	6.50	0.22	10.35	22.25
1s	400.50	200.25	0.40	1.10	0.20	2.58	5.85	0.19	9.32	20.03
2s	400.50	200.25	0.79	2.19	0.40	5.15	5.20	0.17	8.28	17.80
3s	400.50	200.25	1.19	3.29	0.59	7.73	4.55	0.15	7.25	15.58
4s	400.50	200.25	1.58	4.39	0.79	10.30	3.90	0.13	6.21	13.35
5s	400.50	200.25	1.98	5.49	0.99	12.88	3.25	0.11	5.18	11.13

**Table XV.** Percentage of C, H, and Inorganic Ions Based on the Total Number of Ions or Atoms in the Simulated Composites.

<b>Material</b>	<b>% H</b>	<b>% C</b>	<b>% Li</b>	<b>% Al</b>	<b>% B</b>	<b>% P</b>	<b>% Si</b>	<b>% O</b>
LDPE	67.00	33.00	0	0	0	0	0	0
0s	62.57	31.29	0	0	1.016	$3.37 \times 10^{-2}$	1.617	3.476
1s	62.54	31.27	0.062	0.031	1.085	$3.04 \times 10^{-2}$	1.455	3.529
2s	62.50	31.25	0.124	0.062	1.154	$2.70 \times 10^{-2}$	1.292	3.582
3s	62.47	31.24	0.185	0.093	1.223	$2.36 \times 10^{-2}$	1.130	3.635
4s	62.44	31.22	0.247	0.123	1.292	$2.02 \times 10^{-2}$	0.968	3.687
5s	62.41	31.20	0.309	0.154	1.361	$1.68 \times 10^{-2}$	0.806	3.740

Irradiation was simulated on composite material targets using solar protons as the incident primaries. The composite materials were simulated to be homogeneous mixtures which contain 90% LDPE and 10% glass particles by volume. The compositional differences among the samples are also shown in Table XIII. The solar proton energy spectrum was approximated as shown in Figure 23, for which the incident energies are characteristic of those used for interplanetary space mission analysis. The irradiation consisted of  $10^6$  events, with the peak of the energy distribution at 1 GeV/proton. The largest fraction of the protons, perhaps between  $10^2$  and  $10^5$  events, have incident energies below 100 MeV, there are between one and ten events at 600 MeV, and there are few events that take place at incident energies above 800 MeV. The gammas and neutrons produced per primary were detected, as were the fluence of both species transmitted through the simulated shield.

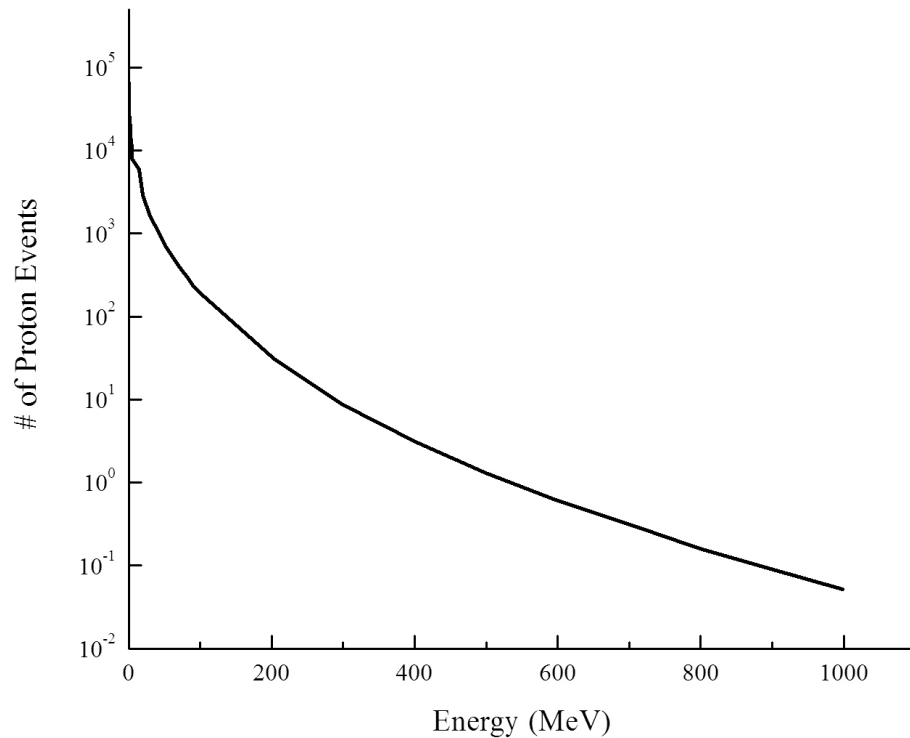


**Figure 23.** Simulated MCNPX Solar Proton Spectrum.

## **B. GeV Proton and Heavy Ion Bombardment in FLUKA**

Two types of experiments were performed in FLUKA on elemental targets and LDPE: GeV proton irradiation and bombardment with  $^{12}\text{C}$  at 1 GeV/nucleon to gauge heavy ion effects. Use of FLUKA enables the simulation of various materials, geometries, and particles. All that is required to run the simulation is the construction of a specifically-formatted input file, but the extraction of data is more involved, and requires the use of specific FORTRAN modules which must be compiled and linked by the user. An advantage of using FLUKA is the heavy-ion module (DPMJET III), which allows the simulation of heavy ions as incident primaries, such as  $^{12}\text{C}$ ,  $^{56}\text{Fe}$ , and  $^{238}\text{U}$ , and the relevant interaction physics.

The list of elements, nuclei, and isotopes available in FLUKA is quite extensive. Compounds can be specified by the user according to the fractions of various elements within the material and some of the known physical properties. The user-specified

compounds are constructed using the mass, volume, or atomic fractions of each element in the material, along with the mass density, or the user may employ several pre-defined compounds, such as polyethylene (CH<sub>2</sub>), which was used in this work.

### 1. Proton Irradiation and <sup>12</sup>C Bombardment

Proton bombardment was simulated on natural beryllium, aluminum, and tungsten targets, as well as LDPE. The Be, Al, and W targets were chosen because they represent materials of low, medium, and very high Z, respectively, and also because meson production is consistent from Be and Al, which are used as meson “factories” in accelerator experiments. For LDPE, the average  $Z_{LDPE} = 2.65$ , which is less than  $Z_{Be} = 4$ , and much less than  $Z_W = 74$ . Within and around target materials, the effect of Z on the magnitude of meson production was observed by comparison of LDPE with the different elemental targets. The experimental geometry is shown in Figure 24. The incident proton energy was 1 GeV/nucleon, and the number of events incident on the target was  $10^5$ . The charged pion fluence was estimated through a two-dimensional vertical projection of the target and the surrounding area, with the fluence being recorded as cm/cm<sup>3</sup>-primary. The targets themselves were designed to be detectors in the simulation, with the energy deposition being binned in the entire volume of the target, and the fluence being binned in the area around the target in the x-y plane, and also in the 100 cm<sup>2</sup> area directly behind the target. Two-dimensional projections of the fluence and deposited energy were converted into three-dimensional projections using the ImajeJ software algorithm for grayscale images.<sup>39</sup> Estimates of dose average LET were obtained by simply dividing the magnitude of energy deposition by the thickness of the target.

The second type of experiment was the irradiation of LDPE with <sup>12</sup>C nuclei at an energy of 1 GeV/nucleon, which was also carried out for  $10^5$  events. For the heavy ion bombardment, the number of nuclear fragments generated in the material was found from the usrsuw user routine. The geometrical coordinates for FLUKA input files are given as (+X, -X, +Y, -Y, +Z, -Z). The target is a rectangular parallelepiped centered at the origin and has dimensions of (+10, -10, +10, -10, +1.0, -1.0) cm. At its boundaries, the target is surrounded by large vacuum and black hole regions so any secondaries which escape outside the desired region of binning are discarded. The coordinates for vacuum and

black hole were  $(+10^6, -10^6, +10^6, -10^6, +10^6, -10^6)$  cm and  $(+5 \times 10^6, -5 \times 10^6, +5 \times 10^6, -5 \times 10^6, +5 \times 10^6, -5 \times 10^6)$  cm, respectively. Behind the shielding, the gamma ray and neutron spectra were also found by MCNPX, which then allows the determination of which nuclear excited states are responsible for the gamma emission by de-excitation.

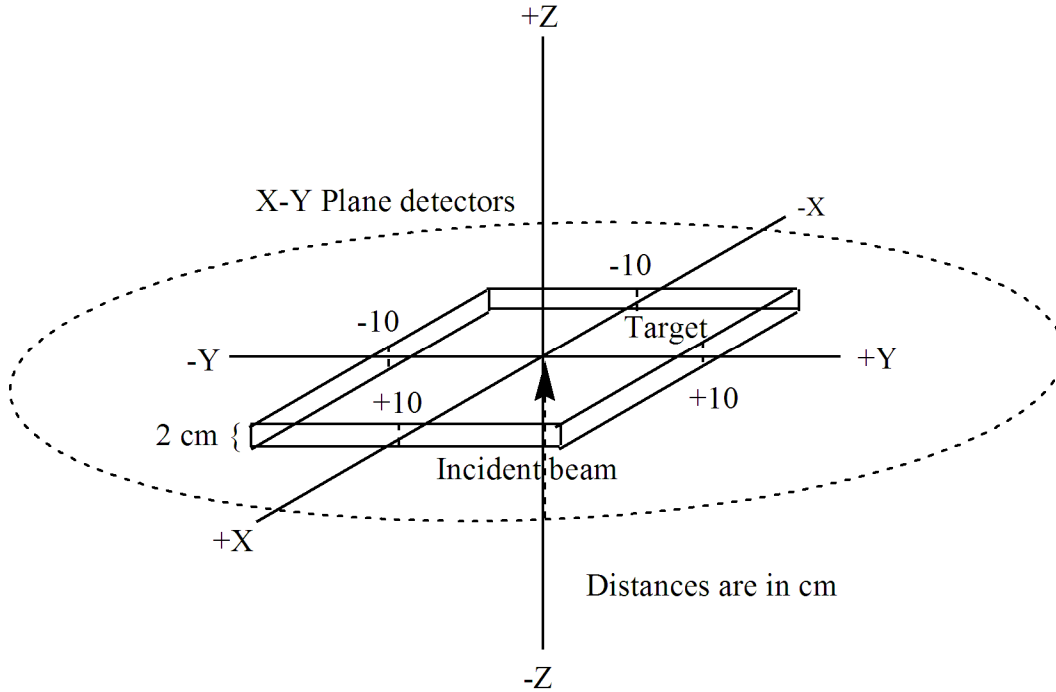


**Figure 24.** Irradiation geometry used in both MCNPX and FLUKA.

### C. Estimates of Mean Range Using LISE

Estimates of mean range were obtained for  $^1\text{H}$ ,  $^4\text{He}$ ,  $^{12}\text{C}$ , and  $^{56}\text{Fe}$  nuclei incident on elemental targets and LDPE. The ranges in  $\text{g}/\text{cm}^2$  were calculated for incident energies from 0 to 3.0 GeV/nucleon (GeV/u) and for particles incident on Be, Al, W, and LDPE target materials as was done in the FLUKA simulations. The various penetration depths were determined by dividing the range in  $\text{g}/\text{cm}^2$  by the volumetric mass density in  $\text{g}/\text{cm}^3$  to obtain a thickness estimate in cm for how far the average particle travels in the given material. The secondary range plots were included as a visual representation of the penetration of heavy particles on solid materials.

### **III. RESULTS**

#### **A. Effects of Primary Protons**

The effects of proton irradiation on composite materials in MCNPX have been compared with the effects that the same primary radiation would have on pure LDPE. The chief result of this study is that alteration of pure LDPE shows a decrease in shielding effectiveness as any particles of moderate- to high-Z are added. The addition of components that feature atoms above  $Z=1$  is in fact deleterious to overall shielding properties. The presence of glass particles produces neutrons and offers no benefit in their attenuation, while the various nuclei within the glass particles are susceptible to excitation, with the excited states most likely to decay by gamma ray transitions. Any mass-reduction benefit that was hoped for with the use of hollow spheres is negated by the presence of heavier nuclei such as Al and Si in the glass, as well as a reduction in the hydrogen density of the bulk material to levels below what is desired. The study was also performed with a rather low aerial density of material, as the composite shields were only 2 cm thick. Thin shields would be cheapest and easiest to deploy, but they would not work as well as thick polyethylene plates or tanks of water, for example.

#### **1. Secondary Gamma and Neutron Radiation**

Solar Proton irradiation of LDPE and Composites shows the generation of significant gamma and neutron generation per incident primary on the composite materials relative to pure LDPE, with the presence of aluminum being conducive to the production and emission of gamma rays within and behind the target. The effects of increasing the fraction of solid glass particles are shown in Figure 25 for simulated  $20\text{Li}_2\text{O}-10\text{Al}_2\text{O}_3-70\text{B}_2\text{O}_3$  glass composites. There is a continuous increase in the production of gamma rays and neutrons as the volume fraction of glass particles is increased. There does appear to be a slight decrease in gamma production at around 3 volume % glass particles, which is the 3s lot of materials. It may be possible that there is some attenuation of gammas by the SGM for this thickness of composite, but it seems

that any addition, even the 0s lot with no SGM, are not as effective shields as pure LDPE alone.

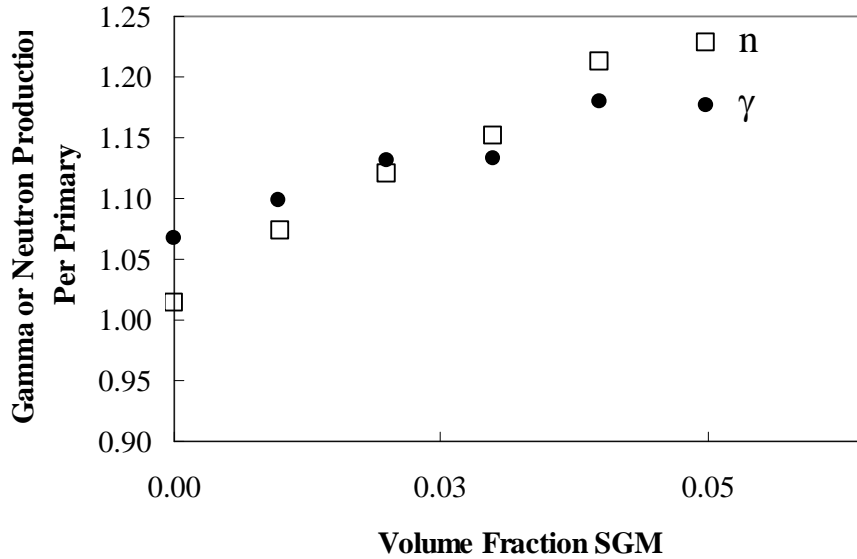


**Figure 25.** Secondary gammas and neutrons produced for  $20\text{Li}_2\text{O}-10\text{Al}_2\text{O}_3-70\text{B}_2\text{O}_3$  composite materials relative to pure LDPE.

The results for the glass-containing composites are presented with regard to what might be expected for a pure, hydrogen-dense material such as LDPE. The vertical axis of Figure 26 is of note since it shows the produced and transmitted secondaries relative to pure LDPE. The 0s composites are at 0.00 volume fraction SGM, but they produce slightly more secondary radiation when compared to pure LDPE. There are about 1.01 times more neutrons produced and 1.07 times more gammas generated for the 0s HGM-only composites in comparison to pure LDPE. The addition of any SGM, starting with the 1s material, increases the effective secondary radiation. However, it should be noted that even at 5 vol% SGM, the maximum resulting radiation is only around 1.25 times the neutrons, and about 1.15 times the gammas generated by pure LDPE in proton bombardment. The comparison of the plotted data with what is expected for pure LDPE seems to indicate that one can expect some amount of secondary radiation in the form of gamma rays or neutrons to be generated by proton bombardment of shields made of

LDPE with no other elements added. The generation of secondary radiation is generally as expected from nuclear and radiation theory, so an indicator of the simulated material's effectiveness is the radiation flux that is experienced behind the shield. Most of the secondary gamma and neutron radiation that is produced is likely to exit a thin shield, such as the 2 cm thick plates of this study.

The generated secondary gamma and neutron radiation is also transmitted through the 2 cm thick shields within this simulation data. Figure 26 shows only a slight difference between the transmitted fluence in comparison to the gammas and neutrons produced in Figure 25; the maximum for transmitted neutrons behind 5s is about 1.20 times what is expected for LDPE, and the transmission of gammas is about 1.15 times greater for 5s. The gamma rays experienced behind the shield increase as the volume fraction of  $\text{Li}_2\text{O-Al}_2\text{O}_3\text{-B}_2\text{O}_3$  glass particles increases, though any minimum at 3 vol% SGM is less pronounced than what is seen in Figure 25.

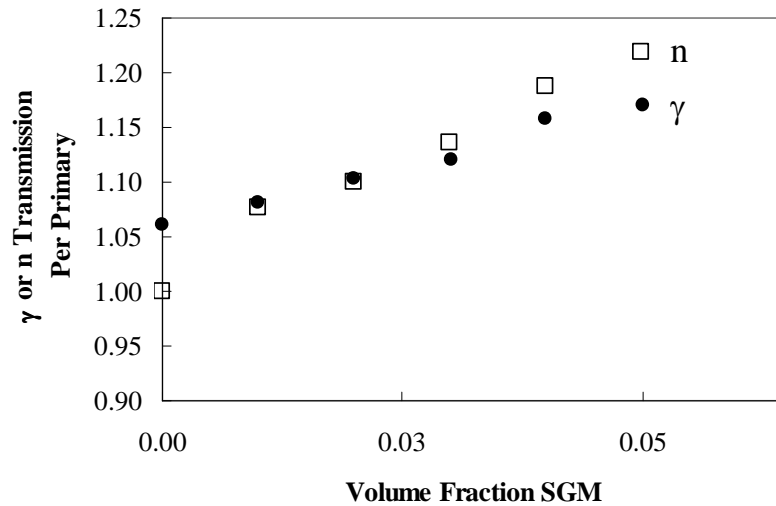


**Figure 26.** Secondary neutrons and gammas transmitted through 2 cm of  $20\text{Li}_2\text{O-10Al}_2\text{O}_3\text{-70B}_2\text{O}_3$  composite shielding.

Another comparison of shielding effectiveness was afforded by repetition of the same experiments using a simulated binary lithium borate glass without any aluminum. This was done in an attempt to reduce the magnitude of generated gammas, as well as

seeing if the original goals of neutron capture were achievable by having the natural concentrations of  ${}^6\text{Li}$  and  ${}^{10}\text{B}$  in the simulated glass. Besides the  $20\text{Li}_2\text{O}-10\text{Al}_2\text{O}_3-70\text{B}_2\text{O}_3$  glass used in the simulation and making the composites, another homogeneous LDPE composite was simulated using SGM of binary  $33\text{Li}_2\text{O}-67\text{B}_2\text{O}_3$  glass composition, as this is deemed to be one of the more durable binary lithium borate compositions.<sup>22</sup> It was hoped that the effect of aluminum on producing specifically  $\gamma$  or n might be determined by separately comparing the magnitude of secondaries produced by the binary and ternary glasses. For the binary and ternary glasses, the relative gamma ray transmission is seen in Figure 27, while the relative neutron transmission is shown in Figure 28. The gamma transmission data shows that 1 volume % binary SGM appears to cause a minimum in gamma transmission. Though the gammas transmitted increase monotonically with further binary SGM addition, the maximum for the 5s material is still about the same as what is expected for pure LDPE. The minimum and gradual increase of gamma radiation appears to indicate that perhaps the lithium or boron in the glass offer some degree of gamma ray attenuation, since increasing the amount of the Al-containing glass only serves to increase the amount of gamma radiation. The potential benefits as radiation shields have not been quantified.

It was hoped that the use of lithium and boron would reduce the transmitted neutron flux, but the data do not appear to show any advantages in the use of natural Li and B in the simulated composites. A comparison of the transmitted neutron flux for the binary and ternary glass composites relative to pure LDPE is shown in Figure 28. It is again evident that the effect of aluminum is most disadvantageous, as the amount of transmitted neutrons increases with increased  $20\text{Li}_2\text{O}-10\text{Al}_2\text{O}_3-70\text{B}_2\text{O}_3$  SGM to about 1.20 times that of LDPE for the 5s materials.

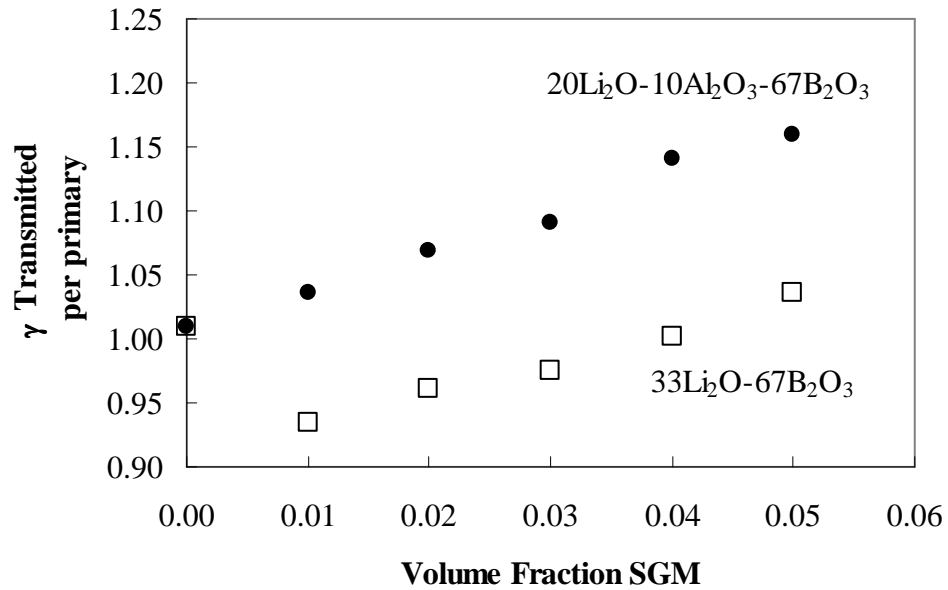


**Figure 27.** Relative gamma ray transmission per primary for simulated composite materials containing lithium borate or lithium aluminoborate glasses.

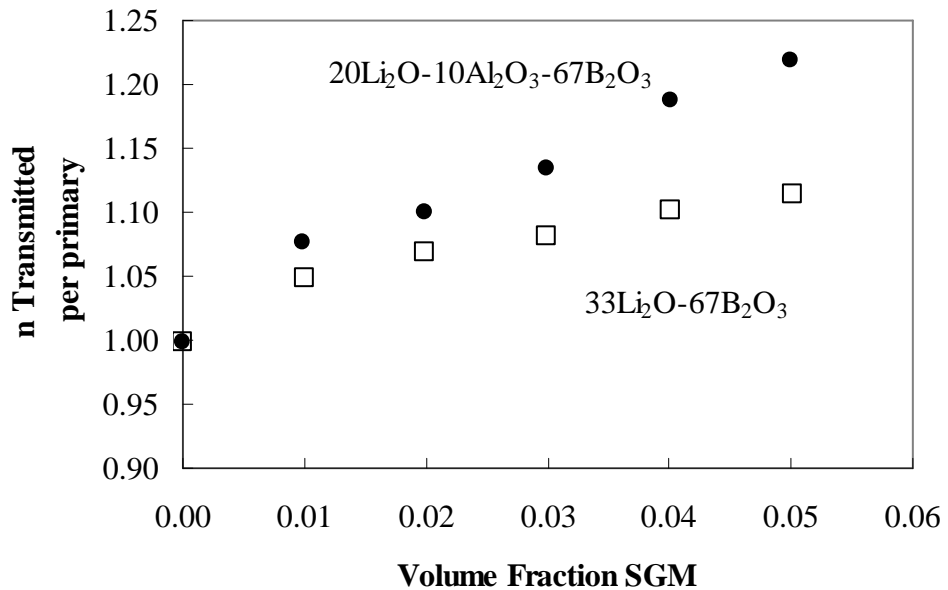


**Figure 28.** Relative neutron transmission per primary for simulated composite materials containing lithium borate or lithium aluminoborate glasses.

The presence of  $33\text{Li}_2\text{O}-67\text{B}_2\text{O}_3$  also serves to increase the neutron fluence behind the shield, though to a lesser degree than for the composites containing the ternary glass. The maximum amount of neutrons is seen for the 5 volume % binary glass composite, which is roughly 1.10 times what would be detected for LDPE in the simulation. The  $33\text{Li}_2\text{O}-67\text{B}_2\text{O}_3$  glass composite does show less neutrons transmitted per primary in comparison to  $20\text{Li}_2\text{O}-10\text{Al}_2\text{O}_3-70\text{B}_2\text{O}_3$  glass, but it can not be said that any of the lithium or boron in either glass serves to moderate or attenuate secondary neutrons; the transmitted neutron flux only increases when elements other than C and H are present in polyethylene. It would also appear that the presence of  $^{27}\text{Al}$  dominates the gamma production, and leads to more neutrons behind the simulated shields.

## 2. Secondary Radiation

The gamma and neutron fluence spectra are useful as a guide to the radiation field one might experience behind common shielding materials. The neutrons are the result of fragmentation, but the specific reactions responsible for the neutron fluence can not be determined. The gamma fluence spectrum allows the resolution of specific gamma rays emissions, as well as the excited nuclear states responsible for them. The gamma transmission data of Figure 27 for binary Vs. ternary glasses gives some indication that the source of most of the gamma rays are in fact the Al nuclei, since the binary glass with only Li and B does not show the same rapidly-increasing secondary transmission up to 5 vol% SGM addition.

Proton bombardment causes transmission of a great deal of energetic gamma and neutron secondary radiation behind the 2 cm thickness of the simulated shielding materials. The gamma ray spectrum generated for MCNPX shows prominent gamma de-excitations due to excited states of the  $^{27}\text{Al}$  nucleus. The gamma ray spectrum is given in Figure 29, along with the energy of the prominent gamma ray de-excitation peaks. This gamma spectrum has emission components ranging from 1.05 MeV to almost 8 MeV in energy, and features a strong emission of 4.73 MeV that dominates the spectrum. The MCNPX simulation results show that the addition of heavier nuclei to a target material generates significant gamma and neutron flux behind the target.

The gamma spectrum consists mostly of transitions that are due to excited states of aluminum. The composite materials contain large percentages of the other elements Li, B, O, and Si, but the gamma emissions shown in Figure 29 are not characteristic of the energy levels or the common de-excitation transitions in those elements. It is possible that other nuclei are excited, but their contribution is not noticeable in the gamma spectrum. This simulation data offers qualitative understanding of the gamma de-excitation process, but a more in-depth analysis would have to consider all of the possible gamma radiation that might result from excited states in Li, B, O, Si, and their isotopes. There are many prospective outcomes based on the irradiation, but it may be seen that there are not only a few excited Al states at low energy, but there is a fairly continuous background of gamma de-excitation, with emitted radiation reaching up to 10 MeV in energy. The processes occurring in the simulated bombardment lead to  $^{27}\text{Al}$  reaching levels up to 10 MeV above the ground state. Some of the excited states and gamma emissions are shown in Figure 29, but this figure is by no means complete.

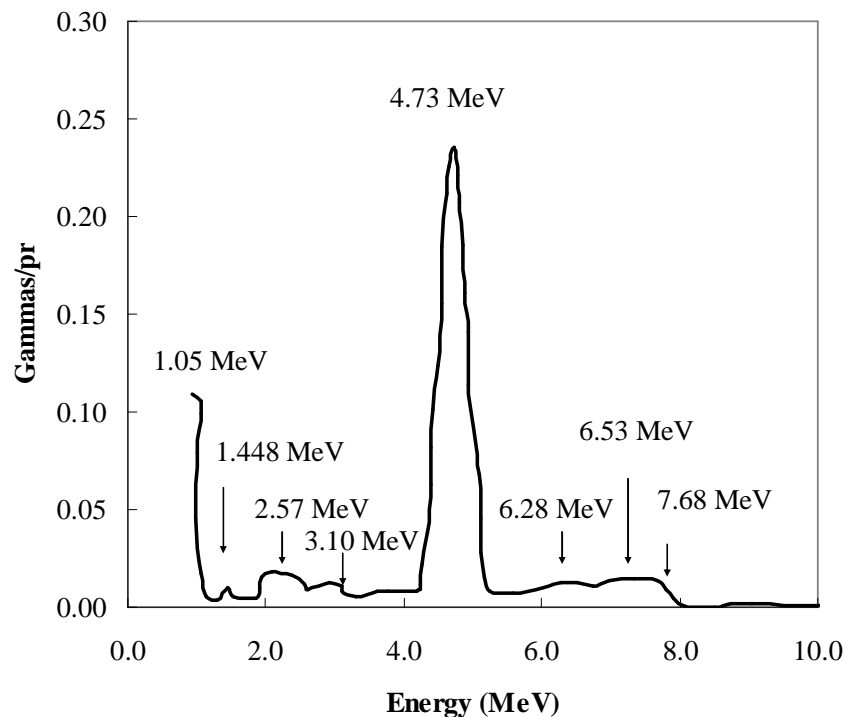


**Figure 29.** Gamma ray spectrum behind composites containing lithium aluminoborate glass.

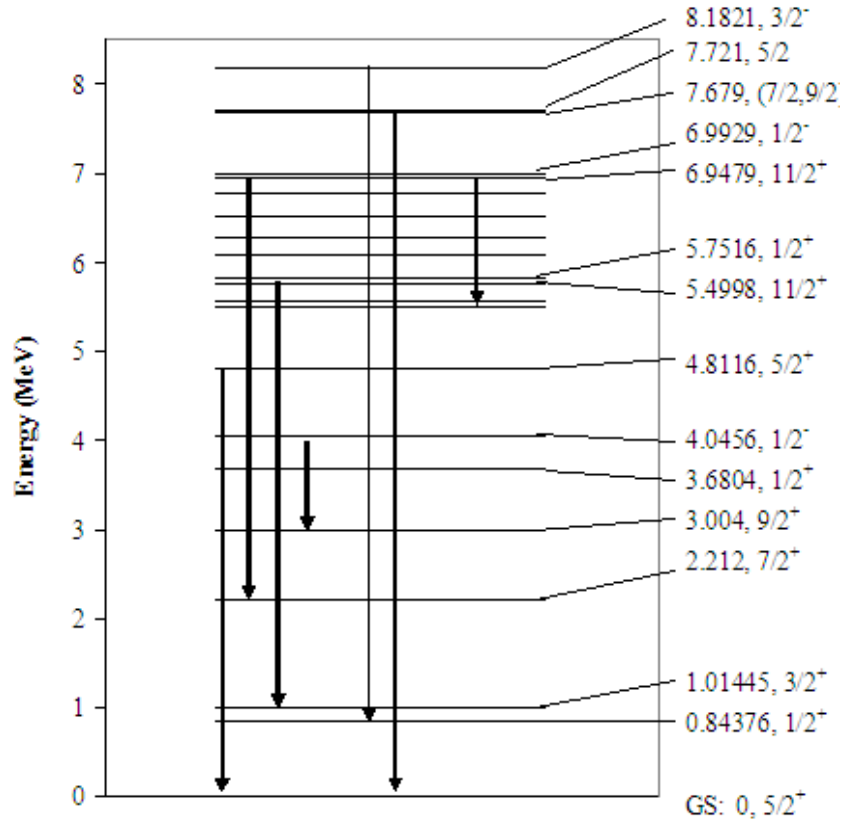


**Figure 30.** <sup>27</sup>Al Excited states and prominent gamma ray emission.

It is difficult to pinpoint the exact source of the neutron fluence behind the targets, but one can expect a fairly continuous background of secondary neutrons to be generated within and transmitted through the composites of this study. However, the majority of neutrons are of fairly low energy, perhaps  $\leq 1.0$  MeV, mostly of the thermal and epithermal regime. The integrated neutron fluence is shown in Figure 31 as the estimated neutrons generated per primary (neutrons/pr), with the fraction being relevant to the  $10^5$  incident primaries. The number of neutrons is off-scale for secondary particles of  $\leq 1.0$  MeV, which shows that there are many target nuclei that are being fragmented, and that the majority of fragmentation neutrons are of much less energy than the incident primaries. There appears to be roughly one neutron produced per hundred primaries for the range  $\geq 1.0$  MeV. It is not possible to determine the spectrum of secondary neutrons from 0 to 1.0 MeV, but it can be assumed that a great number of thermal and epithermal neutrons are produced by fragmentation. Above approximately 1.0 MeV, the fraction of

neutrons per primary is reduced to around 0.05, a value which is fairly constant over the interval between 1.0 and 10.0 MeV. The low fraction in the 1 to 10 MeV regime results in around 5,000 secondary neutrons going through the shield for every 100,000 primary proton events.

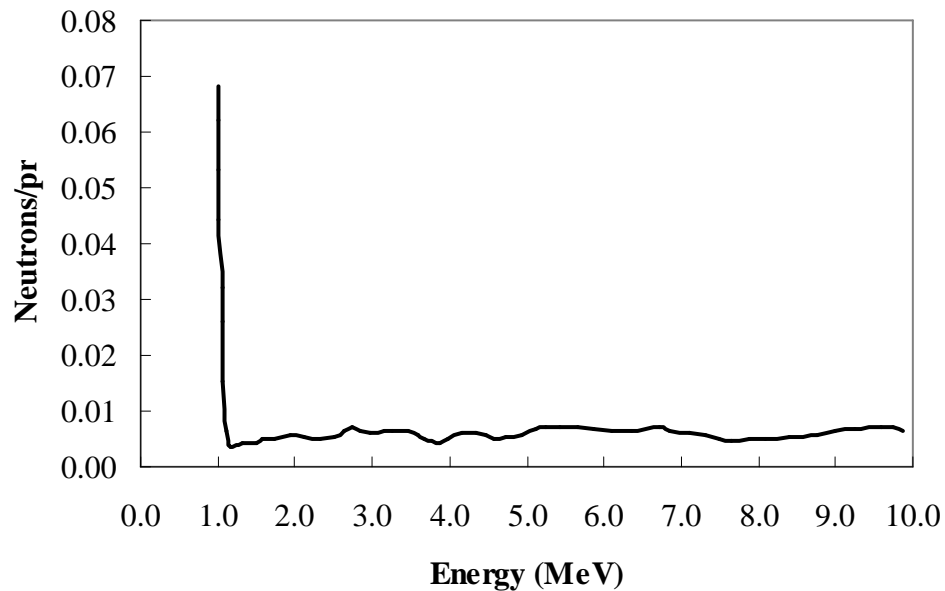


**Figure 31.** Neutron spectrum behind composites containing lithium aluminoborate glass particles.

### **3. Charged Pi-Meson fluence and Deposited Energy in Elemental and LDPE targets**

For the energy limit in the GCR of 1 GeV/nucleon, there must be some awareness of the presence of pi-mesons, since pions will impart some ionization and there is a chance of reactions with the nuclei of the irradiated material. Only charged pions were detected in the simulation.

The simulated fluence plots offer an estimation of the density of charged meson tracks throughout the volume of the target materials. The target itself has been designed to be a detector, so throughout its volume, the Cartesian binning of pi-meson fluence displays the results as cm of meson pathlength divided by  $\text{cm}^3$  of material volume, which results in measure of the number density per area through the volume of the target. The

extent of charged pion production and transport through the targets was estimated by binning the charged pion fluence within the volume of the target, and around the target. Also included were the x-y plane around the target, the two-dimensional within the targets, and the area directly behind the target.

For the generated pions, deposited energy was estimated by the software with the interaction cross sections for these mesons with the nuclei and atoms of the four different target materials. Particle fluence is defined as the number of particles traversing a unit area at a certain point in space in a unit period of time, which is often given in units of  $\text{cm}^{-2}$ . What was recorded in FLUKA is in terms of  $\#-\text{cm}/\text{cm}^3\text{-primary}$ , as shown in Figures 32-38. The charged particle fluence ( $\pi^\pm$  only) as a result of heavy nuclei bombardment is similar for all materials tested, though increases slightly with higher Z target materials, and the magnitude of energy deposition is lowest for LDPE. The fluence is significant within the target area, for both elemental targets and LDPE.

The magnitude of energy deposition due to charged pions has been tracked, with results as expected for nucleon-nucleon interactions at about 1 GeV/nucleon. The production threshold for  $\pi^+$ ,  $\pi^-$ , and  $\pi^0$  is 1 GeV, below which no pions are seen in the simulation. The generation and energy density of charged pions is largest at the center of all targets, at the point of the beam spot and behind. The value is the same, about  $10^{-3}$ , for all elements and LDPE, and drops off by a factor of 5 within a few cm. Be and W show a similar pattern. The meson tracks are clearly seen in the images on the left-hand side of the figures. The magnitude scale of the fluence extends from  $10^{-4}$  to about  $10^{-7}$   $\#/\text{cm}^2\text{-primary}$  for the elemental targets Be, Al, and W, but extends much lower, from  $10^{-4}$  to  $10^{-9}$   $\#/\text{cm}^2\text{-primary}$  for simulated polyethylene. The meson tracks also show a slightly reduced scale for the LDPE in comparison to the pure elements: the scale extends from  $10^{-5}$  to  $10^{-10}$  for simulated LDPE, whereas it spans from  $10^{-4}$  to  $10^{-10}$  for Be, Al, and W. The number of mesons generated in and propagating away from LDPE is reduced by roughly one order of magnitude compared to simulated pure elements.

There is a slightly larger magnitude of pion fluence through the entire target for pure elementals in comparison to LDPE. The tracks show how the pions may propagate through the four materials, and some of them may reach a distance of about half a meter away from the target. It is not possible to determine exactly what is occurring at the dark

areas in the center of the irradiation geometry, except that the pion fluence is at a maximum in this vicinity. It is also necessary to remember that the vacuum and black hole regions outside the target discard any escaping particles, so it can not be determined from the this data how far each particular track-generating meson travels. It is also not possible to tell if any of the propagating mesons are captured to form stars from the meson track and fluence plots. Also of note is that the neutral pi-mesons ( $\pi^0$ ) have not been tracked. It is likely that nearly equal numbers of  $\pi^+$ ,  $\pi^-$ , and  $\pi^0$  are produced in such proton bombardment, but the radically different lifetimes of  $\pi^\pm$  and  $\pi^0$  would be the governing factor in how far any individual meson travels, and its appearance within such simulations.

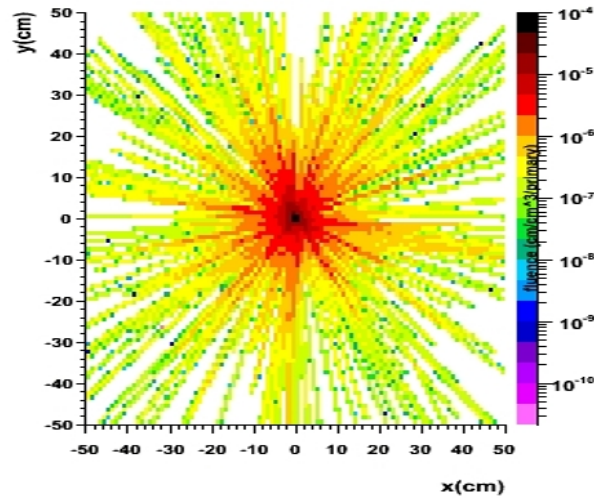


**Figure 32.** Charged pion fluence in and around Be target.

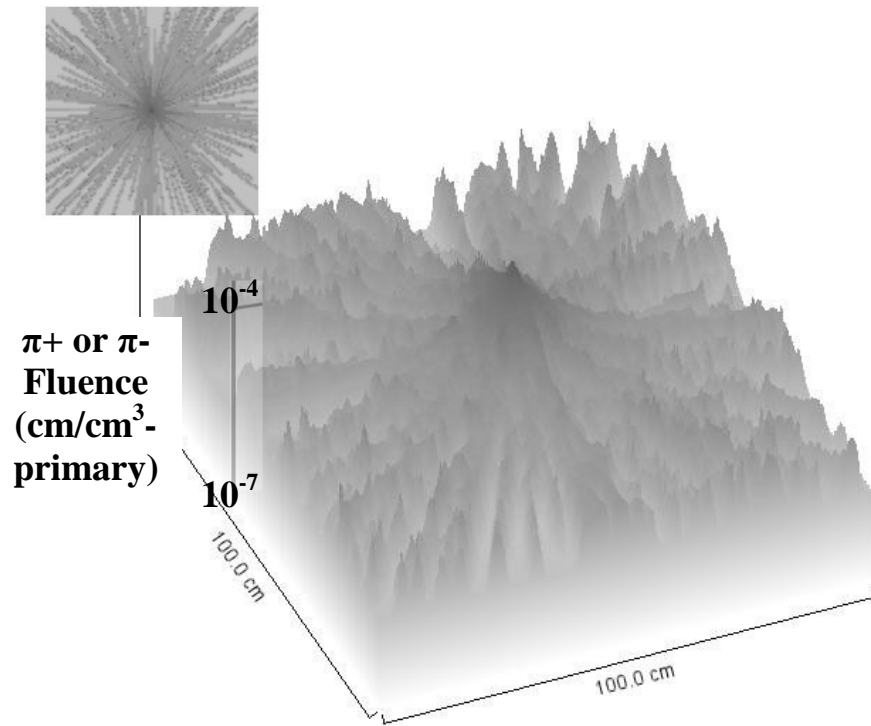


**Figure 33.** Three-dimensional representation of charged meson track density in and Around Beryllium target.

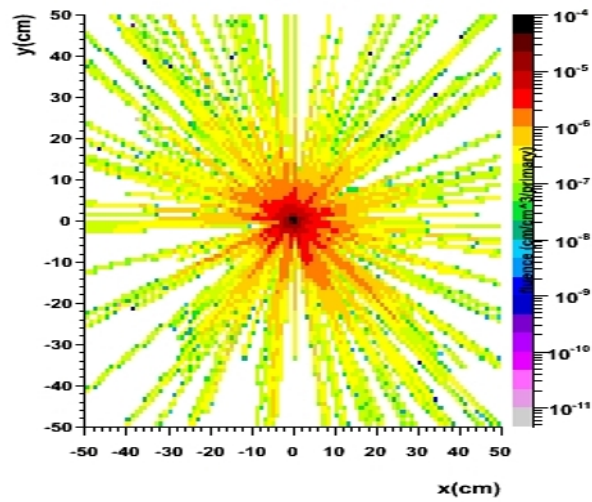


**Figure 34.** Charged pion fluence in and around Al target.

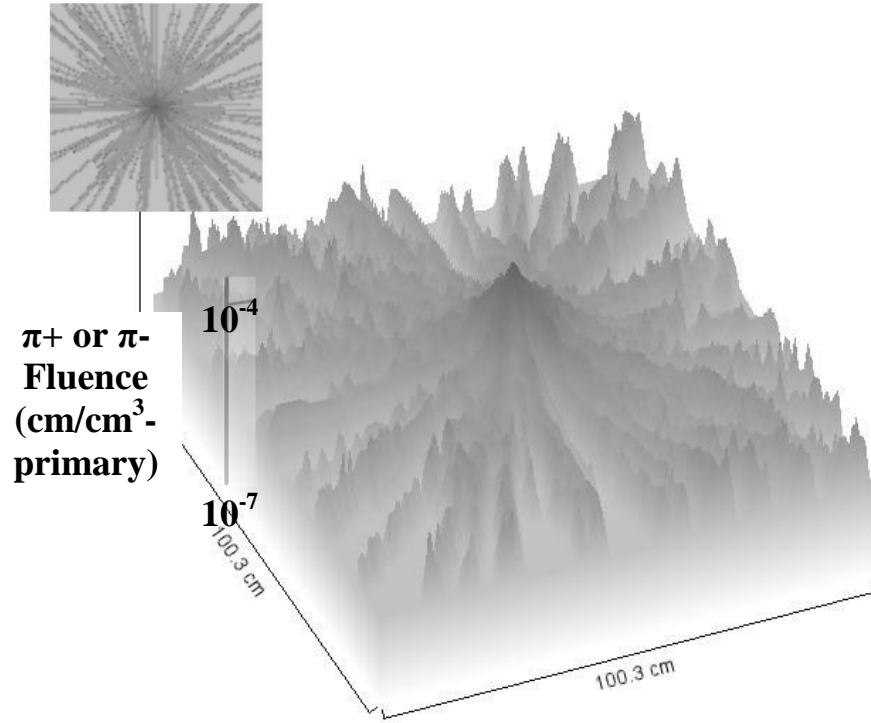


**Figure 35.** Three-dimensional representation of charged meson track density in and Around Aluminum target.

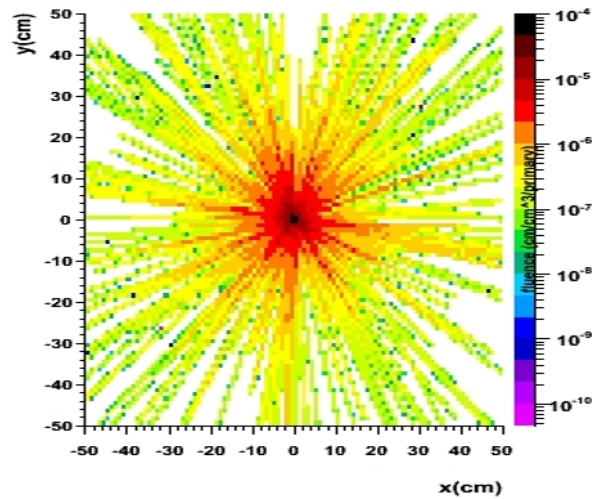


**Figure 36.** Charged pion fluence in and around W target.

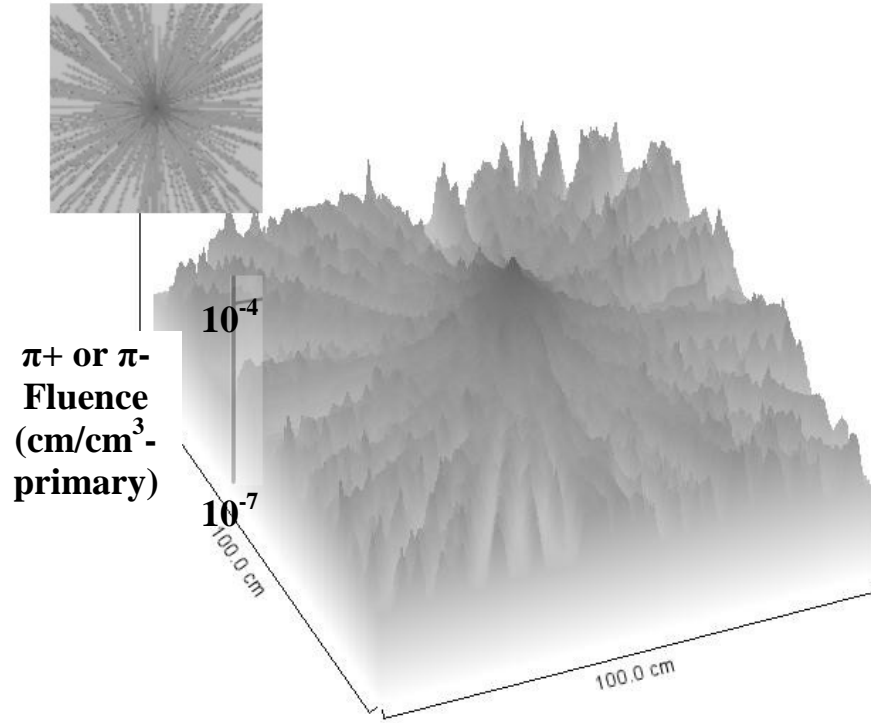


**Figure 37.** Three-dimensional representation of charged meson track density in W target.

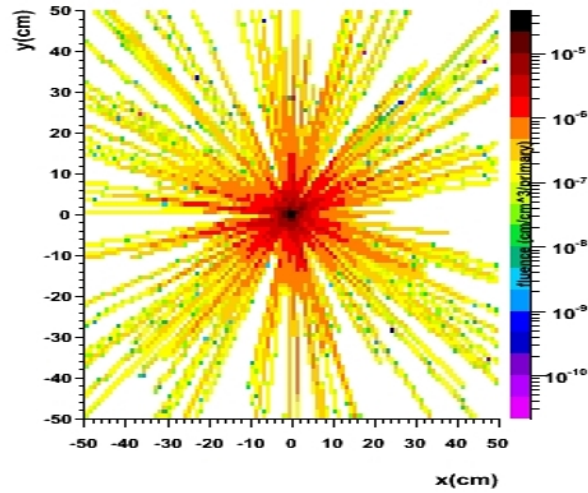


**Figure 38.** Charged pion fluence in and around LDPE target.

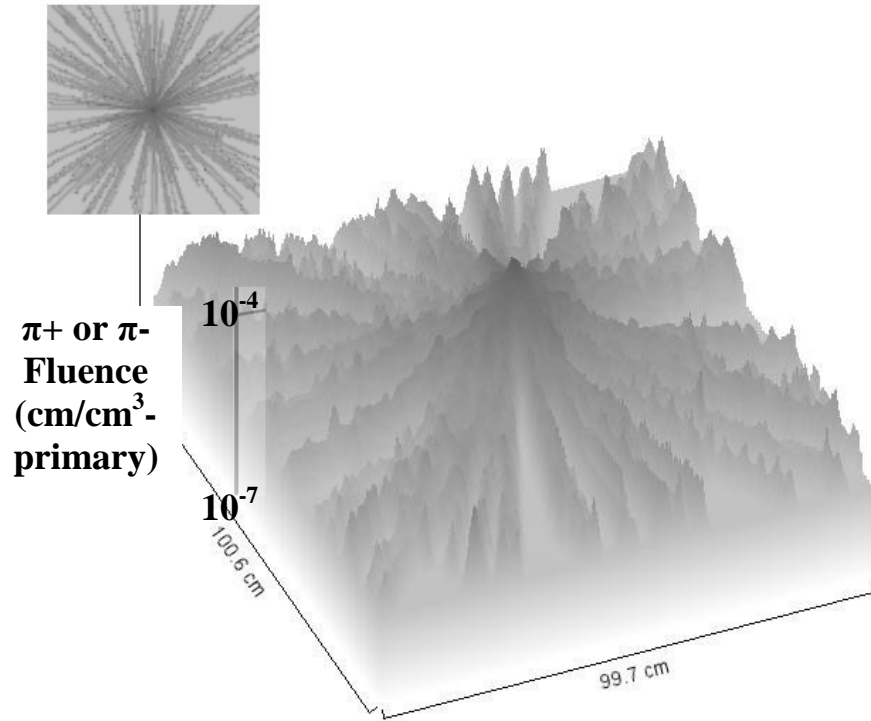


**Figure 39.** Three-dimensional representation of charged meson track density in LDPE target.

## B. Deposited Energy

The deposited energy in the targets is due primarily to the cascades generated within the material after being struck by GeV proton events. The magnitude of the energy deposition is on the order of  $10^5$  eV per incident primary. As expected, the maximum energy deposition occurs at the center of each of the targets at the location where the particles are incident., so it is evident that the primary protons themselves are able to deposit a great deal of energy within the target. The magnitude of energy deposition gradually falls off when moving away from the center of the elemental targets, but the behavior is quite different for the LDPE sample.

All targets experience a maximum energy deposition of  $10^{-4}$  GeV per  $\text{cm}^3$  per primary proton at the center of the sample, which gradually falls off to a minimum of  $10^{-7}$  GeV per  $\text{cm}^3$  per primary at the edges of the target. The estimated maximum in absorbed energy is roughly  $10^5$  eV per primary particle per  $\text{cm}^3$  of material, which results in a total of approximately  $10^{10}$  eV/ $\text{cm}^3$  deposited at the center of the target for the duration of the

simulated proton bombardment. Near the boundaries of the target, the estimated minimum deposition is around  $10^2$  eV per primary particle per  $\text{cm}^3$  of material, which results in a total of about  $10^7$  eV/ $\text{cm}^3$  deposited at the edges of the target. The two- and three-dimensional projections of the energy deposition are shown in Figures 38-45.

The two- and three-dimensional projections for the elemental targets (Be, Al, W) all display very similar behavior with regard to the magnitude and distribution of the energy deposition, but the projections for LDPE are quite different in the magnitude and location of the accumulated energy. The two- and three-dimensional projections for the Be target are respectively seen in Figure 40 and Figure 41. The magnitude of energy deposition falls from  $10^{-4}$  to about  $10^{-5}$  within a radius of 2 cm from the center of the target, but the deposited energy remains above  $10^{-5}$  GeV/ $\text{cm}^3$ -primary for the majority of the target's volume. Only at distances greater than or equal to 5 cm from the center does the deposited energy fall to below  $10^{-5}$  GeV/ $\text{cm}^3$ .

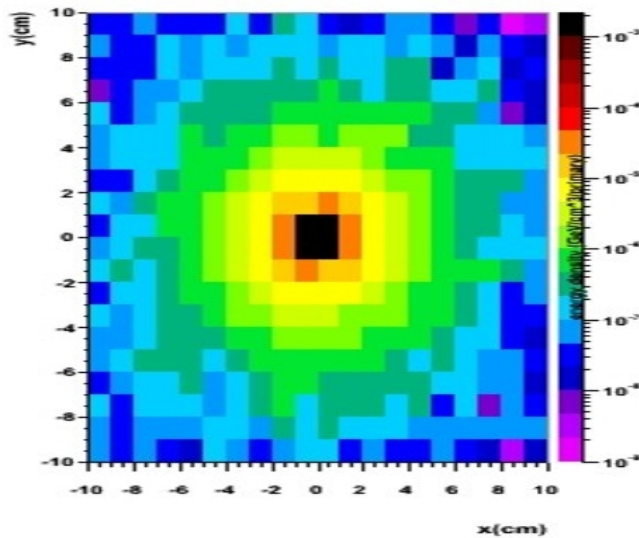


**Figure 40.** Two-dimensional projection of energy deposition in beryllium target.

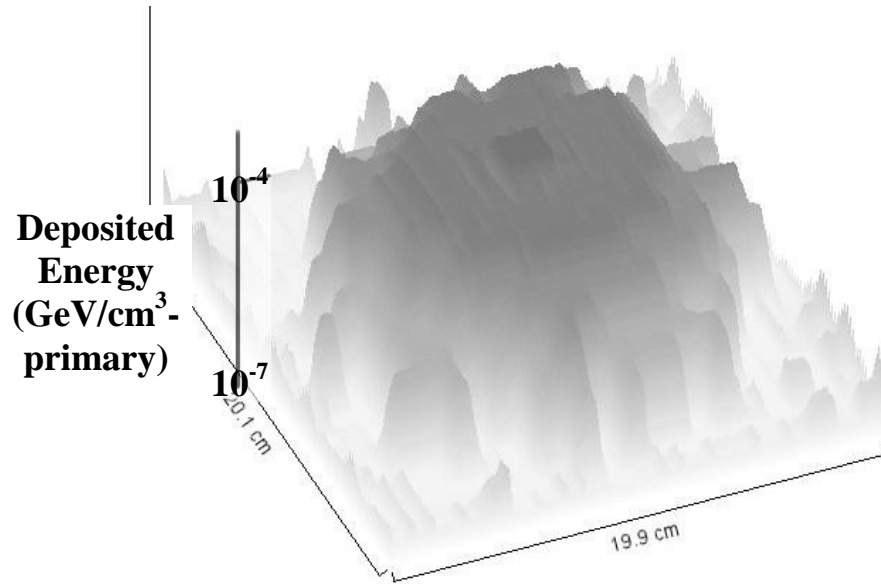


**Figure 41.** Representation of deposited energy density in Beryllium target.

For the aluminum target, the projections for deposited energy are displayed in Figure 42 and Figure 43. This data shows almost the same trend in comparison to the beryllium target: the energy deposition falls from the maximum of  $10^{-4}$  to  $10^{-5}$  within a radius of 2 cm away from the center, but the deposition remains above  $10^{-5}$  GeV/cm<sup>3</sup>-primary for the majority of the area in Figure 42, and the entire target volume, as shown in Figure 43.

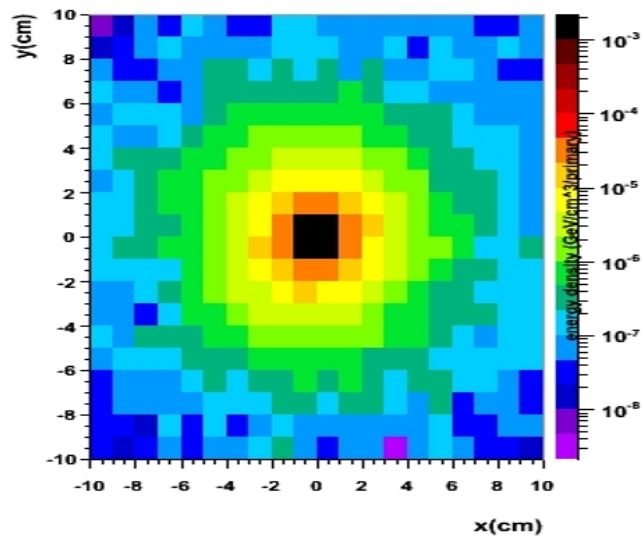


**Figure 42.** Two-dimensional projection of energy deposited in aluminum target.

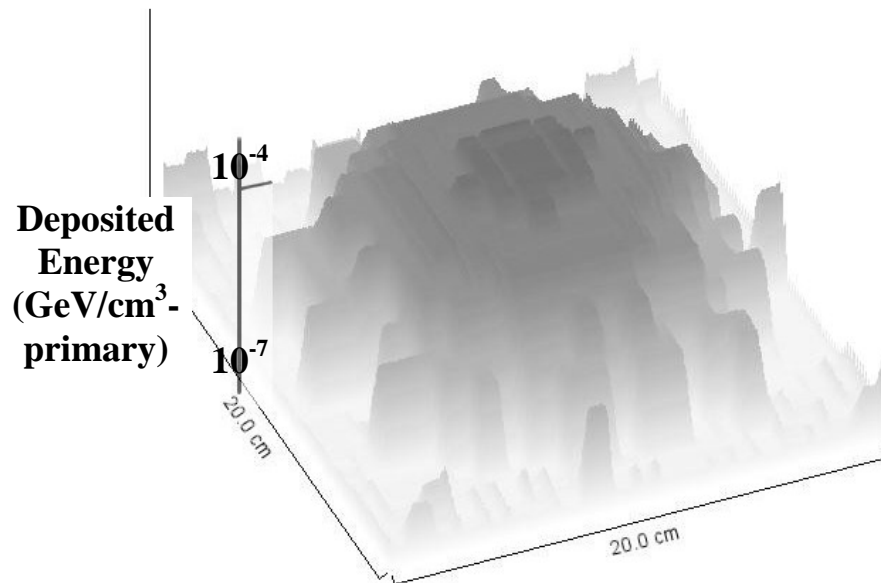


**Figure 43.** Representation of Deposited Energy in Aluminum target.

The data for the tungsten target is almost identical to what was seen for both the aluminum and tungsten targets. The maximum energy deposition of  $10^{-4}$  GeV/cm<sup>3</sup>-primary falls off to about  $10^{-5}$  within a few centimeters from the incident beam spot, but remains above  $10^{-5}$  GeV/cm<sup>3</sup>-primary for the majority of the sample volume. Only when

approaching a distance of 1 or 2 cm from the target's edges does the deposition start to fall below  $10^{-6}$  GeV/cm<sup>3</sup>-primary.

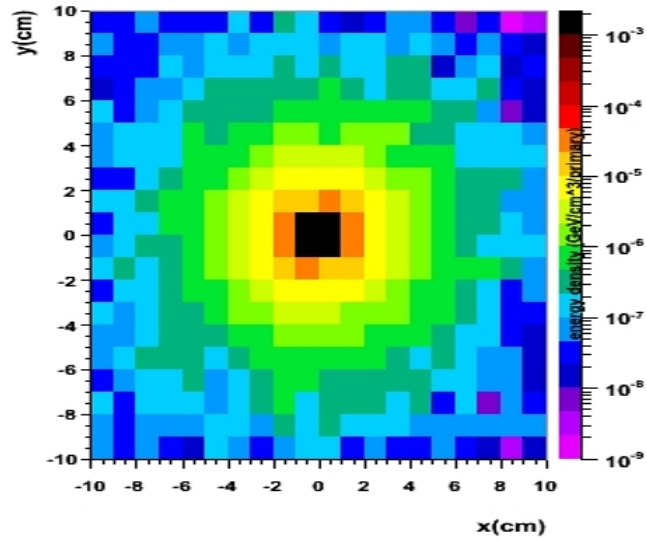


**Figure 44.** Two-dimensional projection of energy deposited in tungsten target.

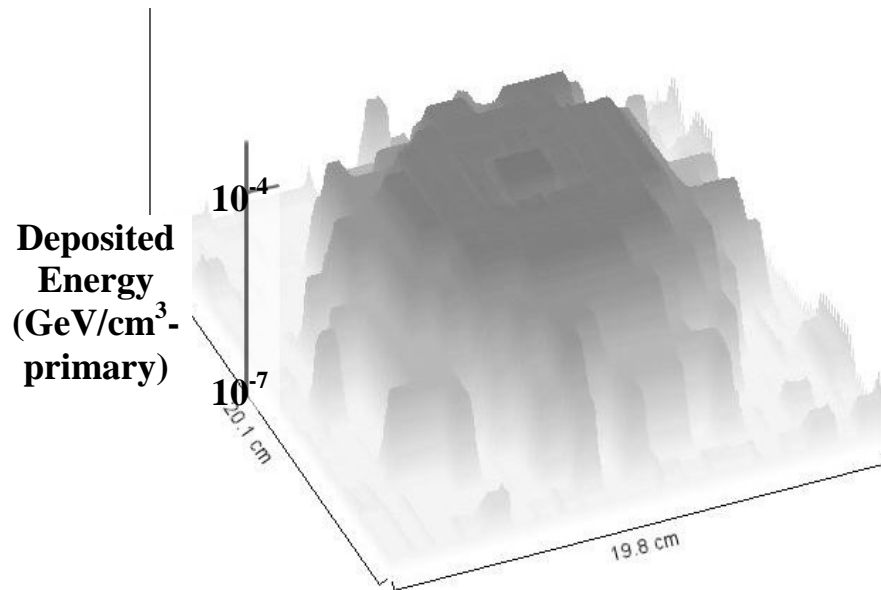


**Figure 45.** Three-dimensional view of energy deposition in W target.

The energy deposition data for the LDPE target is very different in comparison to the elemental samples. As seen in the elemental targets, the deposited energy reaches the same maximum of  $10^{-4}$  GeV/cm<sup>3</sup>-primary at the center of the LDPE plate, but the magnitude of energy deposition falls off very rapidly to  $10^{-7}$  within 2-3 cm from the center. It is very evident that, subject to the same experimental conditions, there is a much lesser magnitude of total energy deposited in the LDPE samples. Due to the accumulation of deposited energy near the center of the LDPE target and the deposition being almost negligible everywhere else, it also appears that the extent of cascade generation (and the subsequent energy deposited from the cascades) is also much less in the case of LDPE when compared to all elemental samples. This observation is of particular importance, since the use of Be, Al, and W targets allows comparisons of LDPE with nuclei for which  $Z$  is: 1) less than  $Z_{\text{eff}}$  of LDPE (beryllium), 2) larger than  $Z_{\text{eff}}$  of LDPE (aluminum), and 3) many times greater than  $Z_{\text{eff}}$  for LDPE (tungsten).

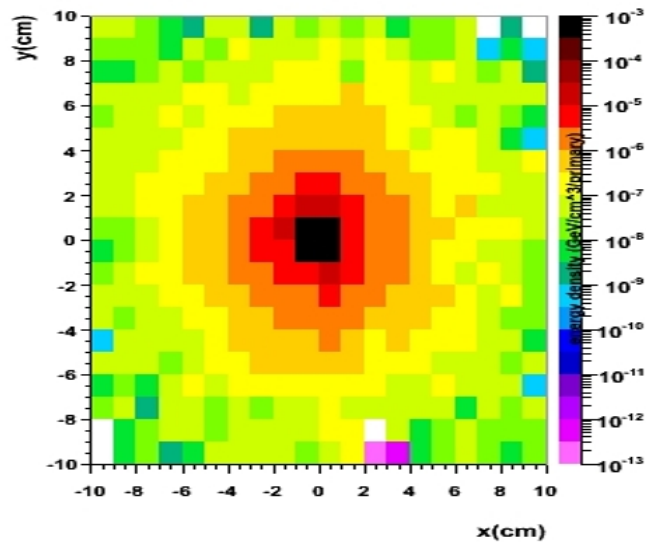


**Figure 46.** Two-dimensional projection of energy deposition in LDPE target.

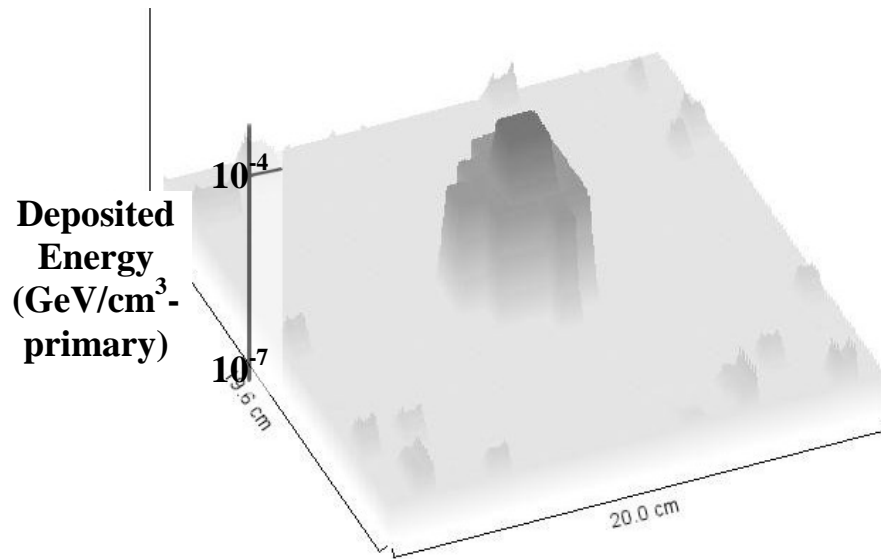


**Figure 47.** Three dimensional projection of energy deposition in LDPE target.

### 1. Range Estimates

The ranges of H, He, C, and Fe nuclei were estimated in Be, Al, W, and LDPE for incident energies from 0 to 3.0 GeV/nucleon. The general behavior is consistent: 1) the smaller the projectile nucleus, the higher the range in all simulated materials at all incident energies, and 2) the higher the electron density in the target material, the shorter the resulting range for any incident particle. The difference between the ranges of  $^1\text{H}$  and  $^4\text{He}$  is very slight, and can not be distinguished in the plots shown. The range of the four nuclei on beryllium are shown in Figure 48, the range within aluminum is shown in Figure 49. The range within tungsten, which contains the highest electron density, is shown in Figure 50, while the range within LDPE, which has the lowest electron density, is shown in Figure 51.

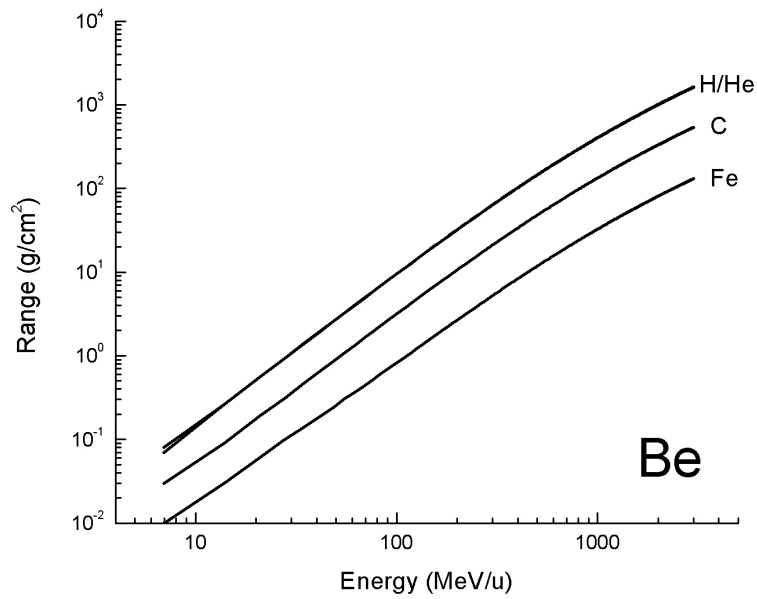


**Figure 48.** Range estimates up to 3.0 GeV/u for heavy particles on beryllium.

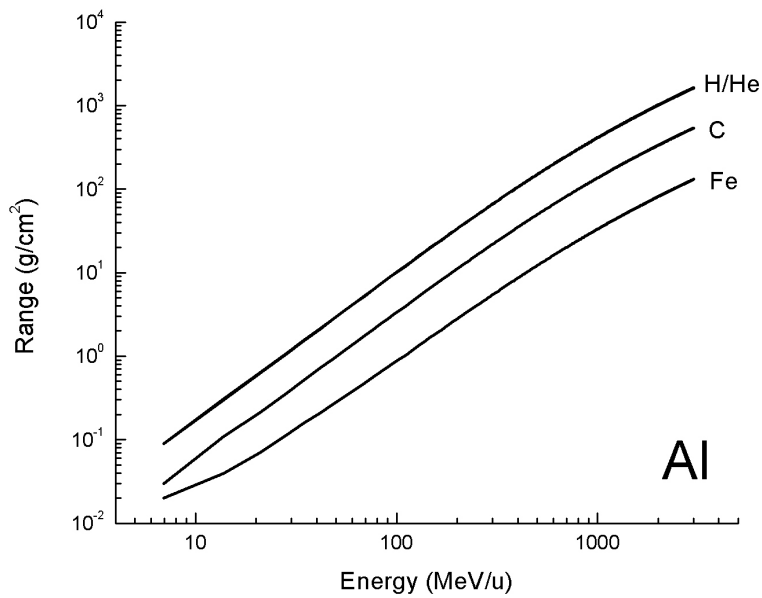


**Figure 49.** Range estimates up to 3.0 GeV/u for heavy particles on aluminum.

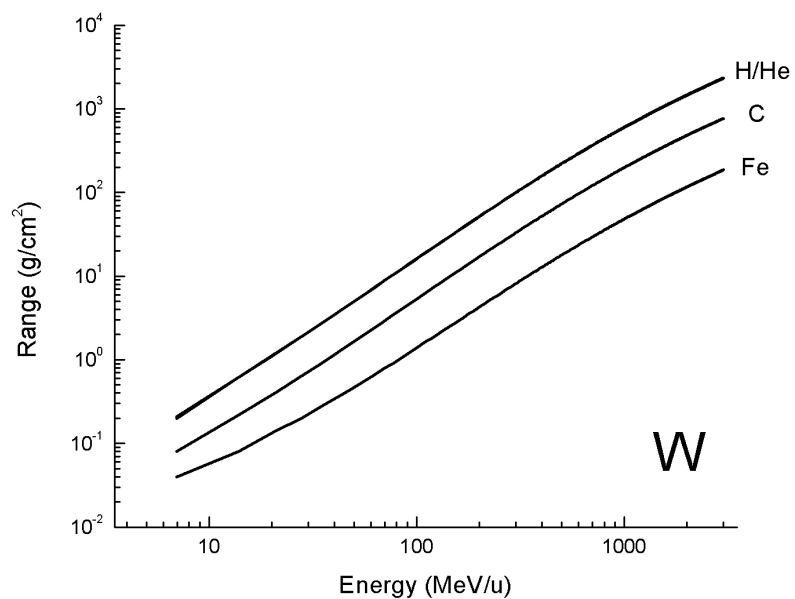


**Figure 50.** Ranges estimates up to 3.0 GeV/u for heavy charged particles on tungsten.

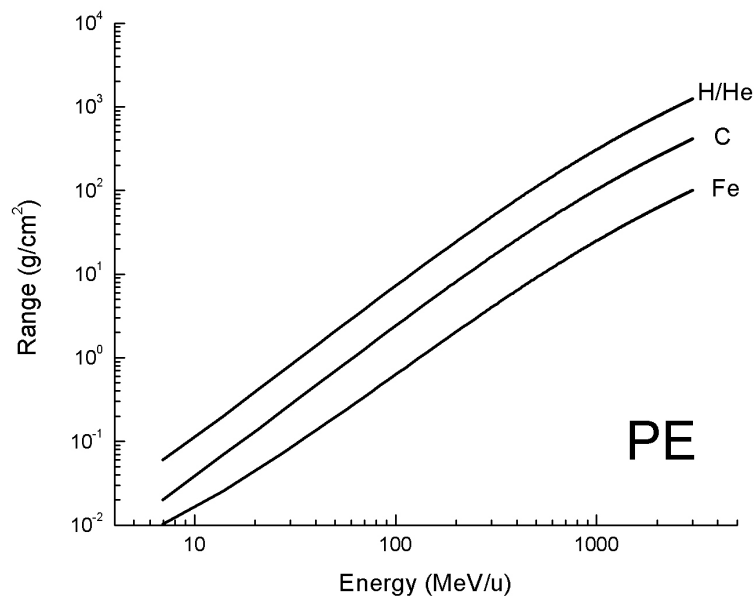


**Figure 51.** Range estimates up to 3.0 GeV/u for heavy charged particles on LDPE.

The mean ranges were displayed as mm of penetration depth to aid in the visualization of effects due to particle size and electron density of the targets. The estimated penetration depths for  $^1\text{H}$ ,  $^{12}\text{C}$ , and  $^{56}\text{Fe}$  on beryllium are shown in Figure 52. Protons have by far the largest mean penetration depth, reaching over 0.9 m at 3.0 GeV, while C penetrates roughly 0.3 m at the same energy, and Fe reaches less than 0.1 m. At the energy most relevant to GCR, 1.0 GeV/u, protons reach approximately 0.2 m, C moves to about 0.08 m, and Fe is stopped at distances of less than 25 mm.

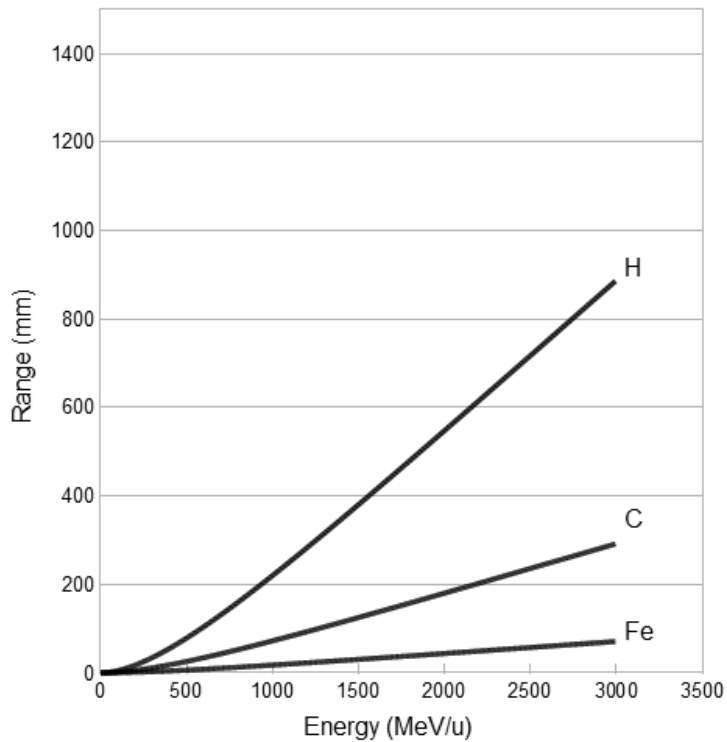


**Figure 52.** Average penetration depth for  $^1\text{H}$ ,  $^{12}\text{C}$ , and  $^{56}\text{Fe}$  in beryllium.

The estimated penetration depths for  $^1\text{H}$ ,  $^{12}\text{C}$ , and  $^{56}\text{Fe}$  on aluminum are shown in Figure 53. The overall shift to lower penetration depths in comparison to beryllium is immediately evident, with protons reaching almost exactly 0.6 m at 3.0 GeV/u, C reaching a maximum of 0.2 m, and Fe attaining a penetration depth of roughly 50 mm. At 1.0 GeV/u, H travels about 0.175 m, C goes to about 50 mm, and Fe moves to a depth of 10-20 mm.

Tungsten displays significant stopping power for the incident ions in question. The penetration depths are shown in Figure 54. H reaches an average depth of ca. 0.15 m at 3.0 GeV/u incidence, C requires a stopping distance of < 50 mm, and Fe at 3.0 GeV/u traverses about 10-15 mm of material. With an incident energy of 1.0 GeV/u, a proton on average travels around 10-20 mm, while C and Fe both behave in a similar fashion, both reaching an average penetration depth of ca. 5-10 mm.

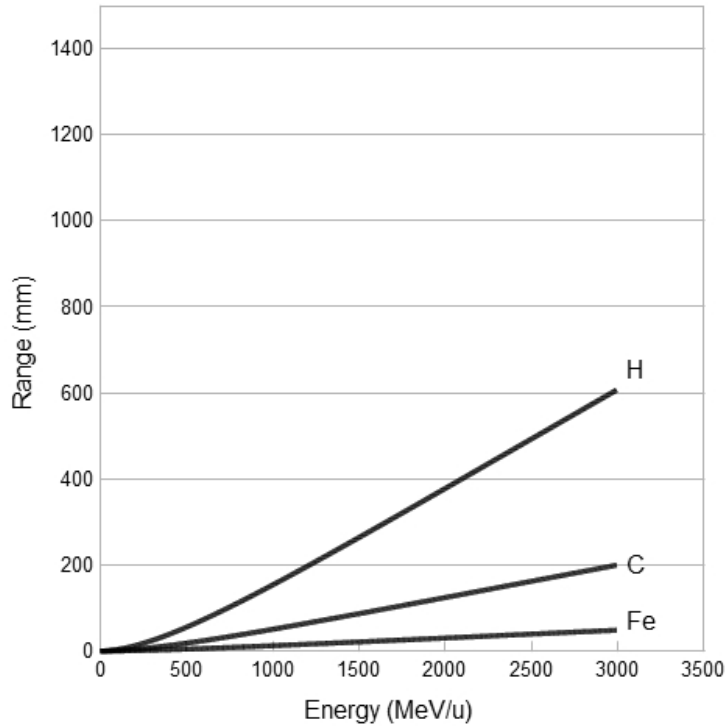


**Figure 53.** Average penetration depth for  $^1\text{H}$ ,  $^{12}\text{C}$ , and  $^{56}\text{Fe}$  in aluminum.

LDPE allows the highest ranges for all nuclei, as shown in Figure 55. The penetration depth for protons at 3.00 GeV/u is around 1.25 m, C reaches 0.425 m, and Fe has a range of slightly over 0.1 m at this energy. At 1.0 GeV/u, H travels around 0.5 m, C travels 0.1 m, and Fe travels about 20-25 mm.

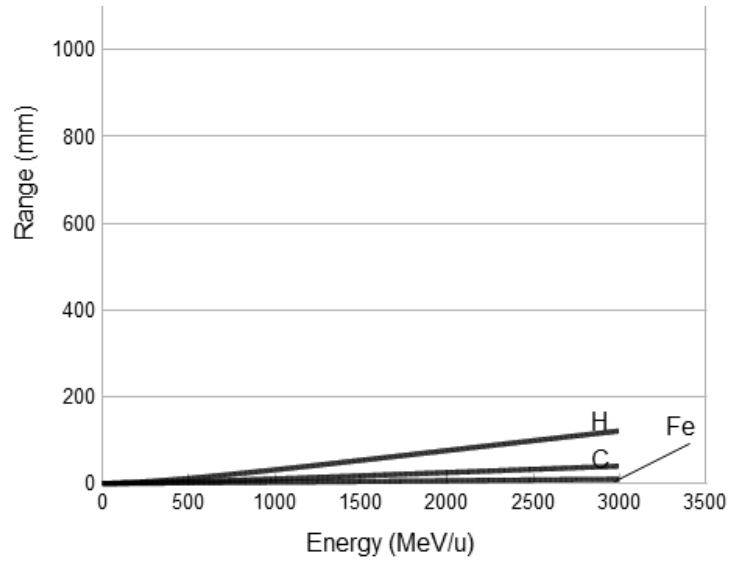


**Figure 54.** Average penetration depth for  $^1\text{H}$ ,  $^{12}\text{C}$ , and  $^{56}\text{Fe}$  in tungsten.

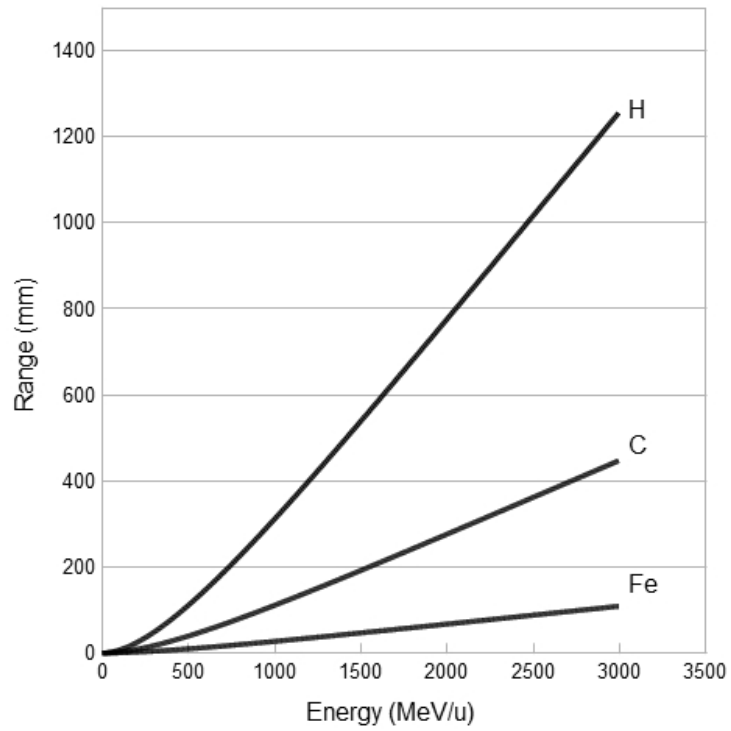


**Figure 55.** Average penetration depth for  $^1\text{H}$ ,  $^{12}\text{C}$ , and  $^{56}\text{Fe}$  in LDPE.

## 2. Heavy Nuclei

### *i. $^{12}\text{C}$ Irradiation of LDPE Target - Fragmentation*

Only some of the possible effects of proton irradiation have been measured here, but the effects of heavier nuclei as primaries are nearly the same, they just occur to a larger extent. The irradiation of target materials by heavy ions will cause a larger magnitude of all of the same effects: ionization throughout and adjacent to their path length, radiation fluence from nucleons and gamma rays, fragmentation of the primary and target nuclei, emission of bremsstrahlung radiation, and production of charged  $\pi$ -mesons. There is also energy accumulated within targets as a result of all processes. When the number of nucleons in a projectile or its incident energy are increased, one should expect much more ejecta in the form of secondary particles and electromagnetic radiation.

The focus of the heavy ion irradiation was to observe some of how the bulk of the material was changed after being bombarded with a large number of energetic primaries, so the number of residual nuclei generated was measured per primary particle and per cubic centimeter of material. One of the more common heavy nuclei in the GCR is  $^{12}\text{C}$ , so this ion was used to irradiate pure LDPE, and determine which fragments were generated within the sample. The reason for the use of  $^{12}\text{C}$  is that there should not be any residual nuclei generated by either the primaries or the polymer for which  $A$  is much larger than what would be seen for the largest isotopes of carbon, namely  $^{13}\text{C}$  and  $^{14}\text{C}$ .

The irradiation of pure LDPE targets with  $^{12}\text{C}$  nuclei generates sixteen nuclear fragments, with ten being stable, five being subject to further decay by electron capture, and one remnant ( $^3\text{H}$ ) that decays in the  $\beta^-$  mode. The data for unstable fragments is shown in Figure 56, while stable fragments are shown in Figure 57. All of the fragments are of  $A = 13$  or lower, as expected, since LDPE contains only hydrogen ( $A = 1$ ) and carbon ( $A = 12$ ), and the incident projectile also has  $A = 12$ . Such light nuclei are most likely to experience  $\beta^-$  decay or electron capture ( $\epsilon$ ), both of which produce radiation that is not as harmful as, for example, the energetic alpha particles emitted by heavy nuclei such as  $^{236}\text{U}$ . It is not possible to determine if any trapped primaries contribute to the detected fragments. Spallation and charge-changing of either the projectile or target

nuclei would also be expected to reduce  $A$  of the constituent target nuclei, mostly  $^1\text{H}$  and  $^{12}\text{C}$ . There are no fragments for nuclei above carbon, as expected, and the overall effect is relatively low when compared to the typical atomic densities of many materials; the density of hydrogen in LDPE is of the order of  $10^{22}$  #/cm<sup>3</sup>, while there are a maximum of roughly  $10^3$ - $10^4$  residual nuclei (both stable and unstable) generated per primary within pure LDPE. Of the stable fragments, it is readily seen in Figure 57 that the high-energy spallation reactions produce stable Li, Be, and B, as expected from studies of cosmic rays.<sup>5,6,26</sup>

The type and number of unstable fragments that result are less than the number of stable fragments generated per unit volume of material. The simulation data yields the number of fragments are per incident primary, so the numbers would be expected to increase monotonically with an increasing number of incident projectile events. The uncertainty in this data is 10-20%, in accordance with the compiled cross-sectional data within the FLUKA code. The least common of the unstable fragments is  $^9\text{C}$ , with a number between one and ten per cm<sup>3</sup> and per primary, so for a total of  $10^5$  or  $10^6$  incident proton events, one can expect about the same total number (and concentration) of these  $^9\text{C}$  nuclei per cm<sup>3</sup> of irradiated material. Pure polyethylene has a hydrogen density of  $8.89 \times 10^{22}$  #/cm<sup>3</sup>,<sup>23</sup> so the concentration of unstable  $^9\text{C}$  nuclei is still about 16 or 17 orders of magnitude less than the number of hydrogen nuclei per cm<sup>3</sup>. The hydrogen density of polyethylene is reduced to  $6.6 \times 10^{22}$ /cm<sup>3</sup> for LDPE with 5% boron addition, and around  $5.4 \times 10^{22}$ /cm<sup>3</sup> for lithium polyethylene.<sup>23</sup>

The most frequently-formed unstable nuclei within the simulation are  $^{11}\text{C}$  and  $^3\text{H}$ , which appear at levels of about 1000/cm<sup>3</sup> and 300/cm<sup>3</sup>, respectively for each incident primary. Multiplying by the  $10^5$  or  $10^6$  events yields a maximum concentration of unstable nuclei on the order of  $10^8$  to  $10^9$  per cm<sup>3</sup> of ion-irradiated polyethylene, which are far below the  $10^{22}$  nuclei/cm<sup>3</sup> for the non-irradiated material, by around 13 or 14 orders of magnitude. The unstable nuclei and their decay reactions are shown in Table XVI. These lighter nuclei decay via  $\beta$ - or  $\epsilon$  modes, which would not supply the same energetic decay radiation to objects behind irradiated shields.

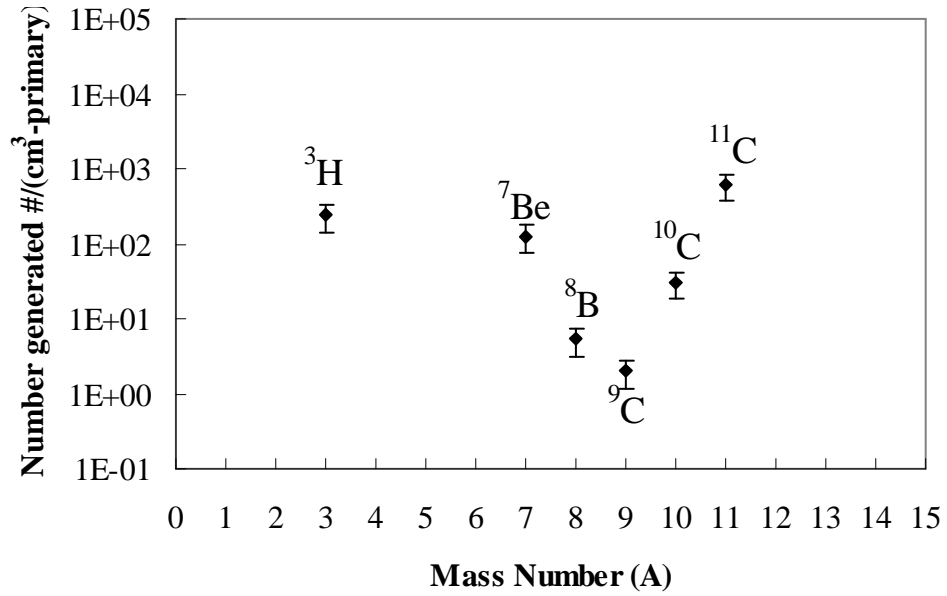


**Figure 56.** Unstable fragments generated in LDPE per primary.

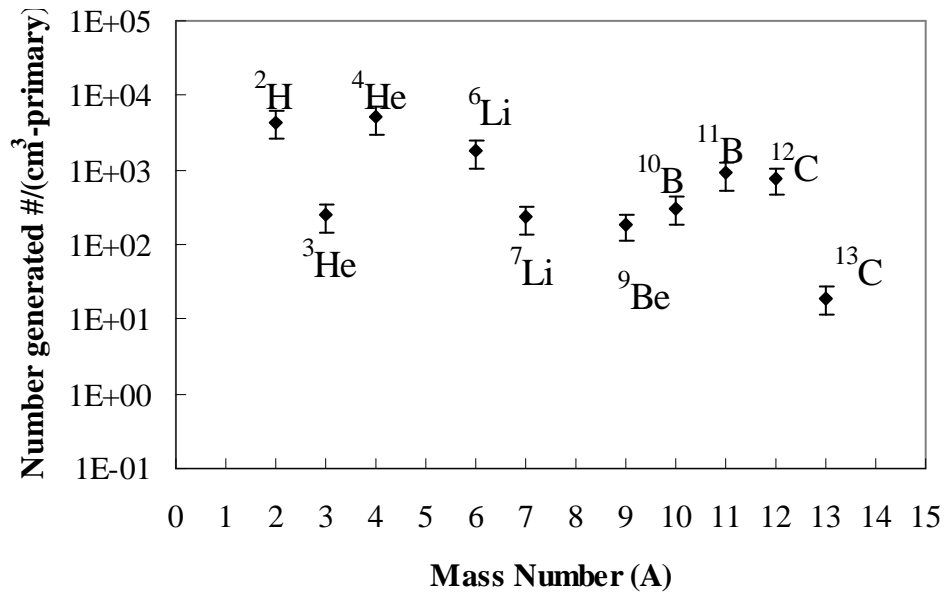


**Figure 57.** Stable fragments generated in LDPE per primary.

The unstable nuclei vary considerably in their respective half-lives, but the majority exhibit electron capture, which yields a stable nucleus and an emitted neutrino. The exception is the  $^3\text{H}$  nucleus, also called tritium, which decays in the  $\beta^-$  mode, but is also quite stable, with a half-life of 12.3 years. The tritium nucleus ejects a total of about 18.6 keV of energy in the decay, with an average electron energy of about 5.7 keV, and the remaining 13 keV being carried by an electron anti-neutrino. The other five unstable nuclei have mean half-lives ranging from as little as  $0.85 \times 10^{-15}$  s (as) for  $^9\text{C}$ , to a maximum of 53.3 days for  $^7\text{Be}$ , but only emit neutrinos, which are not considered to be ionizing radiation.

**Table XVI.** Unstable Residual Nuclei from  $^{12}\text{C}$  irradiation of LDPE Target.

Nucleus	Z	A	$T_{1/2}$	Decay Reaction
$^3\text{H}$	1	3	12.3 y ( $\beta^-$ )	$^3_1\text{H}_2 \rightarrow ^3_2\text{He} + e^- + \bar{\nu}$
$^7\text{Be}$	4	7	53.3 d ( $\epsilon$ )	$^7_4\text{Be}_3 + e^- \rightarrow ^7_3\text{Li}_4 + \nu$
$^8\text{B}$	5	8	0.772 s ( $\epsilon$ )	$^8_5\text{B}_3 + e^- \rightarrow ^8_4\text{Be}_4 + \nu$
$^9\text{C}$	6	9	0.85 as ( $\epsilon$ )	$^9_6\text{C}_3 + e^- \rightarrow ^9_5\text{Be}_4 + \nu$
$^{10}\text{C}$	6	10	19.2 s ( $\epsilon$ )	$^{10}_6\text{C}_4 + e^- \rightarrow ^{10}_5\text{B}_5 + \nu$
$^{11}\text{C}$	6	11	20.4 m ( $\epsilon$ )	$^{11}_6\text{C}_5 + e^- \rightarrow ^{11}_5\text{B}_6 + \nu$

## IV. DISCUSSION

### A. Protons

The use of MCNPX and FLUKA by institutions such as CERN and NASA in similar studies largely validates the findings here.<sup>5,6,10,11,17,21,24,31,40-43</sup> Interaction physics and cross-sections are considered to be accurate for this reason, but true quantitative effects of the simulation are difficult to calculate accurately. The discussion of secondary radiation from proton bombardment necessarily involves the generation of any secondary radiation by  $X(p,A)X'$ , where A could be any quantum of radiation that results from the exchange ( $\gamma$ , n,  $\pi$ , etc.). Another possibility is a fragmentation reaction, for which the identity of  $X'$  must be determined in accordance with the exchange part of the reaction. The results that have been demonstrated here are generally as expected, based on previous studies of energetic gamma ray, proton, and heavy-ion bombardment of materials such as aluminum and polyethylene.

#### 1. Secondary Gamma and Neutron Radiation

The comparison of binary and ternary glasses in composites shows that the addition of even moderately heavy nuclei such as  $^{27}\text{Al}$  has a negative effect on the shielding properties of materials. The two phenomena appear to have separate causes, with neutrons being due primarily to fragmentation, and the gamma emission originating from the excited nuclear states within targets. The primary effect of the incident projectiles seems to be excitation of material nuclei to excited states. Moderately-heavy elemental targets such as C, N, O, Mg, Al, and Si have been studied a great deal with regard to the  $X(p,\gamma)X'$  reaction, as these gamma rays are employed extensively in  $\gamma$ -ray line astronomy.<sup>27</sup> The study of Lesko et.al. measured the cross sections for gamma ray production via the  $X(p,\gamma)X'$  reactions to be on the order of 1 to  $10^3$  mb.<sup>27</sup> The trend was similar for all of the above nuclei: the  $\gamma$  production cross sections are maximized at between 10 and 30 MeV incident proton energy, and drop sharply when the incident primary's energy is above 50 MeV. The  $\gamma$ -ray production is almost negligible for C, N, O, Mg, Al, and Si nuclei above 100 MeV of incident energy. From these findings, it is likely that the  $^{27}\text{Al}$   $\gamma$  spectrum of appears due to the lower-energy components of the

solar proton spectrum, which has a large population of protons incident at 100 MeV and below. As shown in Figure 29, the  $\gamma$  production peaks at about 0.25 per incident primary, which, as expected from the cross-section data, indicates that other processes are more prevalent for the interaction of each primary with a target nucleus. Neutron production per primary seems to have an even lesser contribution to the secondary radiation emitted in the simulation.

For proton bombardment of nuclei such as C, N, Ne, or Al, the neutron production cross sections for  $X(p,n)X'$  display similar characteristics to those reported for  $X(p,\gamma)X'$ .<sup>27,44</sup> The study of Kalend et. al. studied neutron production cross sections for Al, Ni, Zr, and Bi targets at laboratory frame angles between  $20^\circ$  and  $135^\circ$ . What was found was that the cross sections vary from 1 to  $10^3$  mb, reach a maximum  $\leq 40$  MeV incident proton energy, and fall to negligible values above 100 MeV of incident energy. The trends are similar to the  $\gamma$ -ray cross sections listed above, which shows that other processes out-weigh the contribution of emitted secondary gammas and neutrons when the incident energy gets larger than 50-100 MeV.

One of the more important results of the simulation data is that the processes of gamma de-excitation, fragmentation, and meson production only describe a fraction of all the possible nuclear and electronic interactions that might occur. This work has completely neglected processes such as Bremsstrahlung, by which decelerating particles can produce a broad spectrum of energetic and potentially-harmful electromagnetic radiation. Bremsstrahlung radiative emission is expected to dominate the energy loss for any HCP ( $Z > 1$ ) interacting with any materials, as long as the particles have greater than around 700 MeV of incident energy, which in fact describes a large population of the simulated interaction events.

## 2. Mesons

Be and Al targets, though simulated here, are in fact used as “pion factories” in certain beam lines. If charged pions are required in particle physics experiments, then elemental targets are bombarded with GeV protons, and the pions created downstream are then studied. The simulation data offers a look at the extent of charged  $\pi$ -meson fluence, but there is no way to resolve individual meson tracks in the images, nor

differentiate between  $\pi^+$  and  $\pi^-$  from the data. In addition, one can likely expect the production of  $\pi^0$ , but detectors were not defined for these particles.

Charged and neutral mesons will propagate energetically away from the initial interaction site, with the possibility of further interaction with other nuclei of the material, or decay of the mesons themselves into muons, electrons, or even gammas. A captured pion event may result in a star (inelastic interactions with  $\pi$ ), which will further decay into another nucleus and particles such as neutrons. The study of Agosteo et. al. found significant star production in a series of heavy elements (Hg and Ta) after energetic proton irradiation, resulting in roughly 1.22 stars/p for Hg, and 1.31 stars/p for Ta.<sup>45</sup> There is a clear trend toward increased pi-meson production with increasing Z of the target, and the number of inelastic meson reactions actually exceeds the number of input protons. The extent of meson propagation in the various targets of this study has not been determined, since the measurement of the irradiation effects have been localized to the area of the target and the surrounding 50 cm. True quantification of secondary radiation and meson effects would take into account the production of  $\pi^0$ . The neutral  $\pi^0$  does not interact in the same manner as the charged pi-mesons. The charged mesons have a mean lifetime of about  $2.6 \times 10^{-8}$ , but the  $\pi^0$  has an exceedingly small lifetime on the order of  $10^{-17}$ , so can be expected to decay almost instantaneously. The mass energy of the neutral pi-meson is 135.0 MeV, which is smaller than that of either of the charged pi-mesons (139.75 MeV),<sup>7</sup> so the neutral pi-meson decays into two gamma rays, each having exactly 67.5 MeV of energy. The energy of this type of gamma ray is roughly seven orders of magnitude higher than what was seen for the gamma de-excitation of <sup>27</sup>Al from proton bombardment simulations, so the generation of  $\pi^0$  and their subsequent decay should cause a great deal of concern for space radiation analysts. It is nearly impossible to predict the locations of the  $\pi^+$ ,  $\pi^-$ , and  $\pi^0$  that would be created, and thus it is equally difficult to predict the paths that the gammas from  $\pi^0$  would take. The situation behind such irradiated materials is dangerously random.

Meson production has been simulated to show some effects of high energy irradiation that might occur via GCR-material interactions. Most of the interest is centered in the fact that for some long time interval, there would be a number of 1 GeV/nucleon events on any material in space, so researchers must be aware of the

potential nuclear changes that may result in materials. One should also take note of the fact that there are *no* mesons whatsoever shown in the FLUKA data for incident energy < 1 GeV/nucleon. The cross section for the  $X(p,\pi^\pm)X'$  interaction within FLUKA is basically non-existent up to 1000 MeV. This is one of the limitations of the FLUKA software: it is meant for the very-high energy physics community, who are interested in experiments outside the GeV range of energies, primarily TeV and beyond. In fact, a few hundred MeV of incident energy are enough to begin producing mesons, though the number may be small and they may be nearly impossible to detect from purely geometrical considerations. There has been at least one study of cosmic ray triggers on spacecraft and the resulting secondary  $\mu^-$  and  $\pi^-$  radiation.<sup>41</sup> This comprehensive study contained the work of more than 100 authors, and was from data collected by the alpha magnetic spectrometer (AMS-01) aboard the space shuttle Discovery.<sup>41</sup>

The analysis of the AMS-01 data focused on period of four days where the space shuttle was docked with the Mir space station, and the secondary  $\pi^-$  and  $\mu^-$  radiation field behind the Mir was imaged. The AMS-01 experiment was aboard Discovery from June 2 to June 12, 1998, and collected 97 million cosmic ray triggers, which provided valuable measurements of the radiation field in near-earth orbit.<sup>41</sup> Projection plots showed excess radiation flux in a shape matching the exact physical layout of the mir, which corresponded to around 22,000 secondary  $\pi^-$  and  $\mu^-$  events. The focus was on four types of particle events: the study distinguished between upward- and downward-moving particles, and for when the space shuttle was docked or detached from the mir. The events were (a) upward-docked, (b) upward-detached, (c) downward-docked, and (d) downward detached, for which the event rates were also given. The rates were  $1.42\text{ s}^{-1}$  and  $1.87\text{ s}^{-1}$  for events (a) and (b), respectively, while the rate was  $1.1\text{ s}^{-1}$  for events c and d. The excess flux showed up at an additional rate of  $0.064\text{ s}^{-1}$  when docked (a events), and  $0.010\text{ s}^{-1}$  when detached (b events), which are about one event per 15 s, and one event per 100 s, respectively. Clearly the attachment of the Mir greatly increased the secondary cosmic ray flux behind the spacecraft that was then detected. Of note is that there is more than one pion or muon event per second naturally occurring from the cosmic radiation background and the presence of the space shuttle, but the additional flux

generated by matter adds a significant number of potentially-harmful events to the radiation field for almost any time interval in space.

The generated  $\mu$  are not able to participate in further nuclear reactions, so are not deemed to be as harmful as the more energetic  $\pi$ , and the AMS-01 study did not distinguish between  $\pi^-$  and  $\mu^-$ , but the uncertain identity of the secondaries and the event rate are of concern for any interval of exposure. Also, only two directions of traversing particle were recorded, either upward- or downward-moving particles were mapped onto a vertical projection, so there were many directions that were not binned or accounted for. Within the excess flux, one secondary event for every 15 s, corresponds to a rate of 230 # per hour, 5520 #/day,  $1.66 \times 10^5$  #/month, or  $1.16 \times 10^6$  events during the seven month travel time to Mars. One event every 100 s is equal to 36 # per hour, 864 #/day,  $2.59 \times 10^4$  #/month, or  $1.81 \times 10^5$  in seven months. These rates are most valid for typical spacecraft materials at distances rather close to earth, since the Mir was not designed to have exterior low-Z materials as radiation shielding, and the experiments were in near-earth orbit. The rates would be expected to increase as the distance from earth increases, since the protection of the magnetic field decreases when moving away from earth, and because only a small fraction of all the emitted secondaries were recorded and imaged.<sup>41</sup>

## **B. Heavy Ion Bombardment**

### **1. Fragments**

The fragmentation traced by FLUKA shows that the number of generated fragments per unit volume is a small fraction compared to the typical number of nuclei per unit volume in materials like LDPE. The fragmentation simulation does not allow one to distinguish if it is the  $^{12}\text{C}$  projectiles, or the  $^{12}\text{C}$  internal to LDPE that are being fragmented., but it is likely that the presence of the  $^{12}\text{C}$  peak is due to the deposition of  $^{12}\text{C}$  nuclei after they have lost their energy by LET to the atomic electrons. For 12 GeV total energy per nucleus with LET of 145 keV/ $\mu\text{m}$ , this is roughly 8 cm required to stop an incident  $^{12}\text{C}$  particle at 1 GeV/nucleon. The heavier and slower ions generally impart higher LET, as they rapidly lose energy in collisions.

For the ions used at the NASA research center and RHIC of Brookhaven National Laboratory, the identity, incident energy, and the approximate corresponding LET were shown in Table VIII. The heaviest accelerated ions are  $^{56}\text{Fe}$ ,  $^{48}\text{Ti}$ ,  $^{32}\text{S}$ , and  $^{35}\text{Cl}$ . In the RHIC,  $^{56}\text{Fe}$  at 300 MeV/ $\mu$  has an LET of 240 keV/ $\mu\text{m}$ , while  $^{56}\text{Fe}$  at 1 GeV/ $\mu$  has an LET of 150 keV/ $\mu\text{m}$ . This translates into 1250  $\mu\text{m}$  (1.25 mm) to stop the 300 MeV particle, and roughly 6700  $\mu\text{m}$  (6.7 mm) to stop the 1 GeV iron nucleus. For Ti, with  $Z=22$ , the stopping distance is 1000 MeV/108 keV/ $\mu\text{m}$ , which is  $9.26 \times 10^3 \mu\text{m}$ , or roughly 9.3 mm. The ability of materials to stop the sulfur and chlorine nucleus is similar to the situation of Ti nuclei, and reduced in comparison to iron, because of their lower LET. For  $^{32}\text{S}$  and  $^{35}\text{Cl}$  at 600 MeV, the LET of 65 keV/ $\mu\text{m}$  corresponds to a distance  $9.23 \times 10^3 \mu\text{m}$  (9.2 mm). As the mass of the nuclear projectiles is reduced, the related LET is increased, and the distance required to stop the particles increases greatly.

For moderately heavy ions such as  $^{12}\text{C}$ ,  $^{16}\text{O}$ ,  $^{28}\text{Si}$ , the LET is in the tens of MeV, and not hundreds, which causes a greatly-increased penetration distance. For the 290 MeV carbon of this list, the LET of 13 keV/ $\mu\text{m}$  requires a material thickness of 22.3 mm. Two types of energetic oxygen nuclei have been accelerated at BNL, having 600 and 1000 MeV/ $\mu$  of incident energy, and 17 keV/ $\mu\text{m}$  and 14 keV/ $\mu\text{m}$ , respectively. The required thickness becomes excessive, being 35.3 mm for the 600 MeV particle and 71.4 mm for those at 1 GeV. For the larger silicon nucleus, the 600 MeV and 1000 MeV particles will pass through roughly 10.0 mm and 22.2 mm of material respectively before they are halted. The 300 MeV silicon has 70 keV/ $\mu\text{m}$  of LET, and may thus travel through roughly 4.3 mm of material. The light particles, mostly protons at RHIC, are of considerably lower LET, so they do not induce the same magnitude of ionization events along their path, but they also are not easily stopped, especially within the conventional framework of spacecraft construction.

The lowest LET species listed are the GeV protons, having energies of 1 GeV/ $\mu$  and 2.5 GeV/ $\mu$ , and the corresponding LET is 0.24 keV/ $\mu\text{m}$  for both particles. The 1 GeV protons would require  $4.17 \times 10^6 \mu\text{m}$  (4.17 m) to be captured, while the 2.5 GeV protons would require approximately two and a half times this amount of material,  $1.04 \times 10^7 \mu\text{m}$  (10.4 m) to be stopped. It is problematic to deploy construction or shielding materials of these dimensions in space.

## V. CONCLUSIONS

This study reveals a number of issues involved in the use of lithium borate glass microspheres in potential composite shielding materials. A primary finding of this study is that the use of  $\text{Li}_2\text{O}$  and  $\text{B}_2\text{O}_3$  as the primary glass components in the simulated material does not have the intended effects on the radiation field behind the shielding, and specifically the neutron flux that might be experienced. For the simulated proton bombardment, the majority of the radiation field behind the materials consists of secondary gamma and neutron radiation. It was hoped that  $^6\text{Li}$  and  $^{10}\text{B}$  would eliminate some portion of the secondary neutrons, but the number of transmitted neutrons per primary only increased with increasing borate glass content. Gamma emissions by de-excitation are only a small percentage of the secondary radiation which is transmitted through the simulated polymeric matrix materials, but are in the MeV range of energies, which makes them quite harmful to any biological materials or organisms in the path of the radiation.

Gamma de-excitation from  $^{27}\text{Al}$  consists of a number of prominent emissions spanning the range of energies from 1.0 MeV up to a maximum of ca. 8.0 MeV, though the fluence of secondary gammas behind the radiation shield is only a fraction of what is experienced in comparison to secondary neutrons. The peak gamma emission is at an energy of 4.73, which occurs at a rate (flux) of roughly 0.25 per primary proton. There is no simulation data below ca. 1.0 MeV of energy, but one can expect a continuous spectrum of bremsstrahlung keV x-rays and sub MeV gamma rays to be emitted behind these materials as they are continuously bombarded by protons. The all-particle spectrum of Fig. 2 indicates that there are roughly  $10^2$ - $10^3$  GeV particle events occurring per  $\text{m}^2$  of area per second at a distance of 1 A.U., a flux which would result in a high output intensity of energetic bremsstrahlung behind any solids placed into this type of deep space environment.

Proton bombardment creates secondary radiation in all shielding materials of this work, beyond what would be expected for LDPE. Secondary neutrons are typically due to fragmentation of target nuclei, and their energy peaks at ca. the same order of energy as the incident proton had when it struck. The secondary neutrons are obtained

regardless of the type of nuclear reactions or fragmentation occurring, though the specific reactions have not been tracked in this study. There is about one fragmentation neutron generated per incident proton. Boron and lithium were incorporated into simulated composites to test the possibility of neutron capture by  ${}^6\text{Li}$  and  ${}^{10}\text{B}$ , but there was no evidence of neutron attenuation due to the natural presence of these isotopes. It is necessary for energetic neutrons to be thermalized before they are captured by either species. There was a decrease in secondary gamma radiation for materials containing low amounts of the binary  ${}^{33}\text{Li}_2\text{O}$ - ${}^{67}\text{B}_2\text{O}_3$  glass particles (between 0.01 and 0.03 volume fraction).

Relative to pure LDPE, the MCNPX simulations show an increasing combined secondary radiation flux behind the tested materials with increasing borate glass content. The generated secondary fluence ranges between 1.0 and 1.25 per incident primary, but the numbers transmitted through a 2 cm thickness of material are reduced slightly, by around 10%. However, even the 0s and 0f samples transmit an increased radiation flux relative to pure LDPE because of the presence of 10 volume percent silicate glass particles.

Useful information was obtained in the comparison between glass types for the secondary radiation flux realized behind the simulated shields, primarily that the secondary gammas are reduced by the presence of  ${}^{33}\text{Li}_2\text{O}$ - ${}^{67}\text{B}_2\text{O}_3$  glass particles relative to what would be observed behind pure LDPE shielding. Gamma transmission spans values of ca. 1.0 to 1.15 per primary for  ${}^{20}\text{Li}_2\text{O}$ - ${}^{10}\text{Al}_2\text{O}_3$ - ${}^{70}\text{B}_2\text{O}_3$  glass, while the minimum gamma flux is at a value of around 0.93 per primary for the binary lithium borate glass at an addition level of 1.0 volume percent. The simulated composites containing 1, 2, and 3 volume percent lithium borate particles each demonstrate a slight level of improvement over pure LDPE with regard to attenuating the secondary gamma flux. Any potential benefit is most likely explained by this glass having a moderate electron density within a small molar volume, so Compton scattering may be an effective method of gamma attenuation by these boron-based materials. The exact mechanism of gamma attenuation by these materials is unclear at this time, but is worthy of further study.

The same beneficial aspects of the glass particles are not seen with regard to the fragmentation neutron flux for simulated composite shields. The neutron flux ranges from ca. 1.0 to 1.25 per primary proton for the materials containing the ternary glass, while the number is slightly reduced for the binary-containing shields, spanning from a minimum of 1.0 per primary at 0% addition to a maximum of 1.1 per primary at 5 volume % added. From the combined secondary gamma and neutron flux data, the fragmentation neutrons occur in significantly higher numbers, and are much more problematic. Another important consideration for this type of harmful secondary radiation interaction is that the QF for MeV neutrons is around 20 times higher than what would be imparted by gamma rays at around the same incident energy.

The  $^{27}\text{Al}$  nucleus appears to be one of the worst offenders at generating secondary gamma radiation, which is unfortunate, since aluminum metal is one of the most commonly-used structural materials in aerospace applications. The findings in this work and in other space radiation protection studies may in fact force completely new thoughts and new designs in all aircraft and spacecraft, even those used in commercial air travel. A material such as titanium may be highly valued in aerospace engineering due to its high specific strength and high specific modulus, but with  $Z = 22$ , titanium metal is likely to cause even more difficulties than aluminum when it is irradiated by energetic particles.

FLUKA with protons shows that the fluence of charged mesons peaks at a maximum of about  $10^{-4}$  per  $\text{cm}^2$  per primary proton, indicating that the protons enable a high population of meson fluence and particle reactions on the lower end of the energy scale, as well as stars due to the capture of mesons. Though their intrinsic rest mass is relatively low, charged mesons were also seen to propagate large distances through the target, likely causing large numbers of ionization events in their path. A large number of star capture locations are also seen as spikes in the meson fluence data, though the majority of mesons have likely traveled further away than the simulated detectors could measure. The exact types of star capture reactions have also not been identified, which is another area that requires much further study to limit the harmful radiation dose. This type of meson production cross section and reaction data is still actively being pursued by NASA and other space agencies.

The Monte Carlo particle tracking in the FLUKA simulations show a magnitude of energy deposition from all processes peaking at a level of  $10^{-4}$  GeV per  $\text{cm}^3$  per primary proton, which means that each 1 GeV proton may impart a maximum of 100,000 keV of energy to a stricken target upon interaction. This is around ten times the energy of typical atomic x-rays, which like gamma rays, have a low QF due to their lack of mass. The deposited energy is due to a number of tracked processes including inelastic Coulomb scattering and ionization events, as well as the effects that the secondary radiation have when they are produced and subsequently enter into the bulk of the solid material.

The FLUKA simulation proves that the deposited energy throughout the volume of LDPE is many orders of magnitude lower than for the elemental targets. The data for energy deposition indicates that many of the incident protons become backscattered before undergoing even the slightest interaction with the targets, because any interaction would cause some degree of energy deposition throughout the target volume and an associated secondary radiation flux taking place behind the shielding. The backscattering of incident protons and heavy nuclei is the ideal situation for space radiation protection, though it is unknown how effective LDPE would be at backscattering the same number ( $10^6$ ) of incident heavy nuclei events.

The simulation of heavy ion bombardment by  $^{12}\text{C}$  results in a small fraction of nuclear fragments in comparison to the total number of nuclei per  $\text{cm}^3$  in common solids. Unstable lighter fragments that undergo  $\beta$ - and electron capture decays do not provide the same level of harmful dose or quality factor as secondary n or gammas that might be transmitted through shields. It has also been shown that increases in any of the following cause exponential increases in the harmful secondary generation that might be generated within and transmitted through all solid materials: 1) Z of the target, 2) Z of the projectile, 3) electron density of the target, or 4) incident energy of the projectile.

The simulations performed in this study show effects within irradiated solid materials that are difficult to totally eliminate, other than by the use of low Z materials in all aspects of shielding design. There is concern due to the secondary radiation generated within and transmitted through any materials, even those that are the best candidates for shielding, such as pure LDPE. In addition to the generated gamma and neutron

secondaries, there may also be a significant number of unstable nuclear fragments present within the entire volume of an irradiated material, with a maximum on the order of hundreds per  $\text{cm}^3$  per incident particle event. Incident radiation at hundreds of MeV will also cause ionization events and potentially complex nuclear reactions due to the generation of charged and uncharged  $\pi$  mesons that can propagate almost 10 m before decaying. The effects of incident protons and heavy ions are analogous, though the magnitude and extent of the reactions are greatly multiplied in the case of a bound group of protons in comparison to a single projectile event.

The LDPE-based composites in this work have the potential to cause a significant dose behind them, and the expected dosage would be the result of the four types of detected radiation. The dose that might be encountered behind composite shields includes the detection of the four types of radiation in the simulations here: proton and neutron fluence, gamma rays by de-excitation, charged  $\pi$ -mesons, and radioactive fragments, but an overwhelming contribution would come from the many ionization events that would occur in and along the path of the incoming particles. Further significant contributions would come from the radiated bremsstrahlung due to the acceleration of the charged particles. This study has neglected the measurement of path-ionization and bremsstrahlung due to acceleration of the charged particles, but both of these would contribute heavily to the spacecraft's internal radiation field. Depending on the characteristics of the primary, the bremsstrahlung would produce a continuous spectrum with a maximum energy in the x-ray portion of the spectrum. On earth, all attempts are made to minimize x-ray exposure to living things, but this would be impossible on a deep-space voyage. Crews would be continually subjected to some level of x-ray background, and charged  $\pi$  and  $\mu$  particles from their vessel,<sup>41</sup> while the internal radiation field would occasionally be enhanced by the interaction of a rare heavy ion with spacecraft materials and the subsequent effects as described above.

A tangible solution to the "radiation problem" has thus far proven intractable, being limited by physics as well as the current economic and monetary systems of the earth. The use of  $^6\text{Li}$  and  $^{10}\text{B}$  may still prove effective in attenuating and absorbing thermalized neutrons, with neutron moderation being readily achievable via thick layers of hydrogen-rich material placed before the neutron capture materials, as employed in

nuclear reactors. A structure of alternating LDPE alongside lithium- and/or boron-containing layers may provide a suitably effective and inexpensive material for large-scale application. An added benefit may be realized through the secondary gamma attenuation that was observed in this study, though further characterization of the mechanism and optimization of such a fabricated material would be required.

Though there may now be agreed-upon solutions for deep space shielding materials, the cost may prevent this type of long duration space mission from ever taking place. Some schemes call for as much as 500 tons of either H<sub>2</sub>O or LDPE to totally surround a potential space-faring craft. At a cost of roughly \$20,000/kg to send a payload into space, this is roughly \$8 billion, for the aircraft's shielding alone. The cost of the shielding alone could far exceed the cost of designing and constructing the space vehicles themselves.

## REFERENCES

1. M.W. Friedlander, *A Thin Cosmic Rain*; pp. 1-112. Harvard University Press, Cambridge, MA, 1998.
2. J.A. Simpson, "Elemental and Isotopic Composition of the Galactic Cosmic Rays," *Ann. Rev. Nucl. Part. Sci.*, **33**, 323-81 (1983).
3. T.K. Gaisser and T. Stanev, "High-energy Cosmic Rays," *Nuc. Phys. A*, **777**, 98-110 (2006).
4. F.A. Cucinotta, L.W. Townsend, J.W. Wilson, J.L. Shinn, G.D. Badhwar, and R.R. Dubey, "Light Ion Components of the Galactic Cosmic Rays: Nuclear Interactions and Transport Theory," *Adv. Space Res.*, **17** [2] 77-86 (1996).
5. P. Fontes, " $^{10}\text{B}$  and  $^{11}\text{B}$  Production Cross Sections in  $^{12}\text{C}$  Spallation by Protons and Alpha Particles: Application to Cosmic Ray Propagation," *Phys. Rev. C*, **15** [6] 2159-67 (1977).
6. F. Yiou, M. Baril, J.D.D. Citres, P. Fontes, E. Gradsztajn, and R. Bernas, "Mass-spectrometric Measurement of Lithium, Beryllium, and Boron Isotopes Produced in  $^{16}\text{O}$  by High-Energy Protons, and Some Astrophysical Implications," *Phys. Rev.*, **166** [4] 968-74 (1968).
7. K. Krane, *Introductory Nuclear Physics*; pp. 44-76, 80-112, 116-373, 378-82. John Wiley and Sons, Toronto, 1988.
8. D. Griffiths, *Introduction to Elementary Particles*; pp. 1-79. John Wiley & Sons, New York, 1987.
9. E. Segre, *Nuclei and Particles: An Introduction to Nuclear and Subnuclear Physics*; pp. 1-74, 197-206. W.A. Benjamin, New York, 1964.
10. R.C. Singeletery and S.A. Thibeault, "Materials for Low-Energy Neutron Radiation Shielding," (2000) NASA STI Program Office. Accessed on: March 2011. Available at <<http://ntrs.nasa.gov/search.jsp>>
11. C. Zeitlin, J. Miller, S.E. Rademacher, T. Borak, T.R. Carter, K.A. Frankel, W. Schimmerling, and C.E. Stronach, "Heavy Fragment Production Cross Sections from 1.05 GeV/nucleon  $^{56}\text{Fe}$  in C, Al, Cu, Pb, and  $\text{CH}_2$  Targets," *Phys. Rev. C*, **56** [1] 388-97 (1997).

12. J. Miller, C. Zeitlin, F.A. Cucinotta, L. Heilbronn, D. Stephens, and J.W. Wilson, "Benchmark Studies of the Effectiveness of Structural and Internal Materials as Radiation Shielding for the International Space Station," *Rad. Res.*, **159**, 381-90 (2003).
13. E.N. Parker, "Shielding Astronauts from Cosmic Rays," (2005) Dept. of Astronomy and Astrophysics, University of Chicago, Chicago, IL. Accessed on: January 2006. Available at <[http://engineering.dartmouth.edu/~Simon\\_G\\_Shepherd/research/Shielding/docs/Parker\\_05.pdf](http://engineering.dartmouth.edu/~Simon_G_Shepherd/research/Shielding/docs/Parker_05.pdf)>
14. E.N. Parker, "Shielding Space Travelers," *Sci. Am.*, **294** [3] 40-43 (2006).
15. C.J. Zeitlin, L.H. Heilbronn, J. Miller, J.W. Wilson, and R.C. Singleterry, Jr., "Measurement of Charged Particle Interactions in Spacecraft and Planetary Habitat Shielding Materials," (2003) NASA STI Program Office. Accessed on: October 2006. Available at <<http://ntrs.nasa.gov/search.jsp>>
16. W.R. Leo, *Techniques for Nuclear and Particle Physics Experiments: A How-to Approach*; pp. 17-63. Springer Verlag, Berlin, 1987.
17. A. Fasso, A. Ferrari, J. Ranft, and P.R. Sala, "FLUKA: A Multi-particle Transport Code", Version 2004.3.b [Computer Program] CERN, Geneva, Switzerland, 2005.
18. A. Fasso, A. Ferrari, S. Roesler, P.R. Sala, G. Battistoni, F. Cerutti, E. Gadioli, M.V. Garzelli, F. Ballarini, A. Ottolenghi, A. Empl, and J. Ranft, "The Physics Models of FLUKA: Status and Recent Developments," (2003) Computing in High Energy and Nuclear Physics (CHEP2003). Accessed on: March 2011. Available at: <<http://www.slac.stanford.edu/econf/C0303241>>
19. B. Shukitt-Hale, A. Szprengiel, J. Pluhar, B.M. Rabin, and J.A. Joseph, "The Effects of Proton Exposure on Neurochemistry and Behavior," *Adv. Space Res.*, **33**, 1334-9 (2004).
20. B.B. Gersey, T.B. Borak, S.B. Guetersloh, C. Zeitlin, J. Miller, L. Heilbronn, T. Murakami, and Y. Iwata, "The Response of a Spherical Tissue-Equivalent Proportional Counter to  $^{56}\text{Fe}$  Particles from 200-1000 MeV/nucleon," (2004) NASA STI Program Office. Accessed on: March 2011. Available at <<http://ntrs.nasa.gov/search.jsp>>
21. R.H. Maurer, J.D. Kinnison, and D.R. Roth, "Neutron Production Measurements from Shield Materials," (2003) NASA STI Program Office. Accessed on: March 2011. Available at <<http://ntrs.nasa.gov/search.jsp>>

22. J.E. Shelby, *Intoduction to Glass Science and Technology*, 2<sup>nd</sup> ed.; pp. 111-35. Royal Society of Chemistry, Cambridge, UK, 2005.
23. R.K. Kaul, NASA-Marshall Space Flight Center, Huntsville, AL, October 2006, Private Communication .
24. A.F. Barghouty and S.A. Thibeault, "The Exploration Atmospheres Working Group's Report on Space Radiation Shielding Materials," (2006) NASA STI Program Office. Accessed on: April 2010. Available at: <<http://ntrs.nasa.gov/search.jsp>>
25. M. Herr and J.A. Lercher, "Hydrogen Storage in Microspheres." (2003) European Space Research and Technology Centre. Accessed on: March 2011. Available at <<http://www.esa.int/gsp/completed/030910ESTEC16292.pdf>>
26. J.R. Cummings, W.R. Binns, T.L. Garrard, M.H. Israel, J. Klarmann, E.C. Stone, and C.J. Waddington, "Determination of the Cross Sections for the Production of Fragments from Relativistic Nucleus-nucleus Interactions. II. Parametric Fits," *Phys. Rev. C*, **42** [6] 2530-45 (1990).
27. K.T. Lesko, E.B. Norman, R.M. Larimer, S. Kuhn, D.M. Meekhof, S.G. Crane, and H.G. Bussell, "Measurements of Cross Sections Relevant to  $\gamma$ -ray Line Astronomy," *Phys. Rev. C: Nucl. Phys.*, **37** [5] 1808-17 (1988).
28. M. Giard and G. Lagache, "Galactic Emissions: Seeing Through the Galaxy," *C. R. Phys.*, **4** [8] 901-9 (2003).
29. H.W. Kroto, "The Chemistry of the Interstellar Medium," *Phi. Trans. R. Soc. Lond.*, **A 325** [1587] 405-21 (1988).
30. J.H. Heinbockel, S.R. Blattnig, F.F. Badavi, F.A. Cucinotta, G.D. Qualls, J.W. Wilson, M.S. Cloudsley, and J. Tweed, "Sensitivity of Shielding Effectiveness to Nuclear Fragmentation Cross-section Errors," (2005) NASA STI Program Office, Accessed on: October 2006. Available at <<http://www.ntrs.nasa.gov/search.jsp>>
31. C. Zeitlin, A. Fukumura, L. Heilbronn, Y. Iwata, J. Miller, and T. Murakami, "Fragmentation Cross Sections of 600 MeV/nucleon  $^{20}\text{Ne}$  on Elemental Targets," *Phys. Rev. C*, **64** [2] 1-16 (2001).
32. J.W. Wilson, M.S. Cloudsley, F.A. Cucinotta, R.K. Tripathi, J.E. Nealy, and G. DeAngelis, "Deep Space Environments for Human Exploration," *Adv. Space Res.*, **34**, 1281-87 (2004).

33. R. Bigelow, M.J. Moloney, J. Philpott, and J. Rothberg, *Nuclear and Particle Physics Simulations: The Consortium for Upper-level Physics Software*; pp. 98-116. Wiley-VCH, Berlin, 1995.
34. M.G. Mayer, "Nuclear Configurations in the Spin-Orbit Coupling Model. I. Empirical Evidence," *Phys. Rev.*, **78** [1] 16-21 (1950).
35. S. Pomp, "Tutorial on Neutron Physics in Dosimetry," (2009) 11th Neutron and Ion Dosimetry Symposium. Accessed on: July 2010. Available at <www.arXiv.org>
36. A.D. Wrixon, "The 2007 Recommendations of the International Commission on Radiation Protection," *J. Radiol. Prot.*, **28** [2] pp. 161 (2007).
37. Z. Shayer, Dept. of Physics, Colorado School of Mines, Golden, CO, December 2006-March 2007, Private Communication.
38. O. Tarasov and D. Bazin, "LISE++: Radioactive Beam Production with In-flight Separators," *Nucl. Instrum. Methods Phys. Res., Sect. B*, **266**, 4657-64 (2008).
39. W.S. Rasband, ImageJ, [Computer Program]. U.S. National Institutes of Health, Bethesda, MD, 2006
40. A. Ferrari, H. Aiginger, V. Andersen, F. Ballarini, G. Battistoni, M. Campanella, M. Carboni, F. Cerutti, A. Empl, W. Enghardt, A. Fasso, E. Gadioli, M.V. Garzelli, K. Lee, A. Ottolenghi, K. Parodi, M. Pelliccioni, L. Pinsky, J. Ranft, S. Roesler, P.R. Sala, D. Scannicchio, G. Smirnov, F. Sommerer, T. Wilson, and N. Zapp, "The FLUKA Code: New Developments and Application to 1 GeV/n Iron Beams," *Adv. Space Res.*, **35**, 214-22 (2005).
41. R. Henning, M. Aguilar, J. Alcaraz, J. Allaby, B. Alpat, G. Ambrosi, H. Anderhub, L. Ao, A. Arefiev, P. Azzarello, and others, "A Study of Cosmic Ray Secondaries Induced by the Mir Space Station Using AMS-01," *Nucl. Instrum. Methods Phys. Res., Sect. B*, **234**, 321-32 (2005).
42. C. LaTessa, S. Guetersloh, L. Heilbronn, J. Miller, L. Sihver, and C. Zeitlin, "Fragmentation of 1 GeV/nucleon Iron Ions in Thick Targets Relevant for Space Exploration," *Adv. Space Res.*, **35**, 223-9 (2005).
43. J.W. Wilson and F.F. Badavi, "A Study of the Generation of Linear Energy Transfer Spectra for Space Radiations," (1992) NASA STI Program Office. Accessed on: October 2006. Available at <http://ntrs.nasa.gov/search.jsp>

44. A.M. Kalend, B.D. Anderson, A.R. Baldwin, R. Madey, J.W. Watson, C.C. Chang, H.D. Holmgren, R.W. Koontz, and J.R. Wu, "Energy and Angular Distribution of Neutrons from 90 MeV Proton and 140 MeV Alpha-particle Bombardment of Nuclei," *Phys. Rev. C: Nucl. Phys.*, **28** [1] 105-19 (1983).
45. S. Agosteo, M. Magistris, and M. Silari, "Radiological Considerations on Multi-MW Targets. Part I: Induced Radioactivity," *Nucl. Instrum. Methods Phys. Res., Sect. A*, **545**, 813-22 (2005).